On some numerical issues in the Virtual Fields Method: optimization of testing configuration and piecewise construction of virtual fields

Kashif Syed-Muhammad

N^o d'ordre : D.U. 1726
EDSPIC : 368

Université BLAISE PASCAL - Clermont II

École Doctorale Sciences pour l'Ingénieur de Clermont-Ferrand

Thèse

Présentée

pour obtenir le grade de

Docteur d'Université

Spécialité : Mécanique du solide

par

SYED MUHAMMAD Kashif

Sur quelques aspects numériques de la Méthode des Champs Virtuels: optimisation de conditions d'essai et champs virtuels définis par sous-domaines

Soutenue publiquement le 9 Janvier 2007 devant le jury :

M. CHO	Seoul National University, South Korea	Examinateur
M. FRANCOIS	Université de Technologie de Troyes	Président
M. GREDIAC	Université Blaise Pascal, Clermont-Ferrand	Examinateur
F. HILD	ENS de Cachan	Rapporteur
J. MOLIMARD	Ecole des Mines de Saint-Etienne	Rapporteur
F. PIERRON	ENSAM, Châlons-en-Champagne	Examinateur
E. TOUSSAINT	Université Blaise Pascal, Clermont-Ferrand	Examinatrice

Laboratoire de Mécanique et Ingénieries,
Université Blaise Pascal et Institut Français de Mécanique Avancée

Contents

List of Figures

List of Tables

Acknowledgment

I would like to thank the Ministère de l'Education Nationale de la Recherche et de la Technologie (MNERT) of France for financing this doctoral studies. I would also like to thank Space and UPper Atmosphere Research COmmission (SUPARCO) Pakistan for the permission to undertake the PhD studies abroad.

I am grateful to my research supervisors, Dr. Michél GREDIAC and Dr. Evelyne TOUSSAINT for their confidence in my potential by awarding the research topic in the framework of research project, field measurements and identification in solid mechanics (GDR 2519 CNRS). Also, I am very much thankful for their interest, consideration and precious time which they shared during this period. I wish to thank for their teachings and comments which helped me a lot in materializing the thesis in a very satisfying and timely manner.

I would like to thank Dr. M.R. WISNOM and Dr. Fabrice PIERRON for the collaborative research undertaken in the Department of Aerospace Engineering, University of Bristol, UK. I am also thankful to Mr. J.H. KIM for his valuable time and contribution regarding the experimental part.

I am grateful to Dr. Maenghyo CHO, Dr. Manuel FRANCOIS, Dr. François HILD, Dr. Jérôme MOLIMARD and Dr. Fabrice PIERRON for kindly accepting to become the jury members for my thesis defense.

I wish to thank all the members of LaMI and IFMA with whom I interacted during these three years of PhD and enjoyed a very good working relationship.

In the end, I am very much grateful to my parents for their courage and patience in the face of solitude during my stay abroad. Also, I am very much thankful to my wife Nadia for all the good memories during this period especially by being very supportive, patient and encouraging in the days of stress and difficult times. Finally, I wish to thank my lovely kids, Faiza and Faraz who remain a constant source of pleasure, happiness and joy though I could not give them sufficient time and attention during this period.

Résume étendu

La conception optimale d'éléments de structures mécaniques nécessite une bonne connaissance des propriétés mécaniques des matériaux constitutifs. Les matériaux anisotropes et hétérogènes présentent la particularité d'être décrits par des lois qui dépendent généralement de beaucoup plus de paramètres que les matériaux isotropes homogènes. De nombreux essais standards différents conduisant à des champs de contraintes homogènes sont généralement conduits pour les mesurer, ce qui rend la procédure de caractérisation relativement lourde. Une alternative envisageable consiste à tenter d'exploiter des essais dits hétérogènes, c'est-à-dire tels que les champs de contraintes en leur sein soient hétérogènes et non plus homogènes. L'intérêt est que le nombre de paramètres activés est dans ce cas a priori plus grand que dans le cas homogène, ce qui permet de les identifier si une procédure adaptée est disponible. Il faut toutefois insister sur le fait qu'il n'existe généralement pas de lien simple entre mesures locales de l'état cinématique et paramètres inconnus. De même, il est nécessaire de mesurer des champs entiers de grandeurs cinématiques (déplacements, déformations) pour mesurer ces hétérogénéitiés.

Ce travail s'inscrit dans un tel contexte. Il consiste en fait à approfondir l'une des méthodes disponibles pour la résolution d'un tel problème: la Méthode des Champs Virtuels (MCV), qui présente l'avantage d'extraire les paramètres inconnus sans calculs itératifs dans le cas de l'élasticité anisotrope, contrairement au recalage par éléments finis par exemple. Cette méthode est basée sur l'écriture du principe des travaux virtuels avec des champs virtuels particuliers. Elle a été mise en place depuis plusieurs d'années et elle a connu depuis plusieurs développements qui ont permis de l'amériorer. Citons par exemple l'utilisation de champs virtuels spéciaux ou la prise en compte de la minimisation du bruit dans la définition des champs virtuels.

Dans le présent travail, la méthode des champs virtuels est appliquée à la flexion de plaques minces anisotropes. L'utilisation de champs virtuels décrits par sous-domaines et l'optimisation de conditions d'essais vis-à-vis d'un bruit de mesure sont présentés comme des points originaux du travail. Parmi les possibilités d'optimisation, le choix de l'essai, de l'orientation des fibres, de la taille de l'éprouvette, de la lo-

calisation des points d'appui et des efforts, de la forme de l'éprouvette, sont autant de paramètres à prendre en considération. L'idée est de trouver une combinaison optimale de ces paramètres tels qu'une identification plus robuste et plus précise soit possible, particulièrement en utilisant des données bruitées.

Les éléments discutés sont validés numériquement en utilisant des exemples simulés de plaque mince en composites. Un cas d'identification d'une plaque composite endommagée est également étudié numériquement. A la fin du travail, des premiers résultats expérimentaux sont présentés à des fins de validation de la démarche.

De façon plus détaillée, le manuscrit se compose de huit chapitres dont le contenu est le suivant.

Le premier chapitre présente les diverses stratégies exploitant des mesures de champs pour l'identification des paramètres constitutifs de matériaux. Les principes fondamentaux et les principales applications sont discutés pour chacune des méthodes.

Le deuxième chapitre présente la méthode des champs virtuels utilisée dans ce travail. Le cas du problème de la flexion de plaques minces en composites sert de support. On y présente le formalisme général de la méthode.

Le troisième chapitre présente l'effet du bruit de mesure sur la qualité de l'identification. Un travail publié récemment dans la littérature est adapté ici au cas de la flexion. On montre que la minimisation de l'effet du bruit aboutit à un champ virtuel spécial unique pour chaque inconnue, ceci pour une base fonctionnelle donnée.

Le quatrième chapitre présente une validation numérique de la procédure qui a été programmée sous Matlab. On y discute le nombre optimum de sous-domaines retenus pour définir les champs virtuels. Des données simulées obtenues sur une plaque en composite verre-époxyde servent de données d'entrée. L'influence des données bruitées est également étudiée sur la robustesse de la méthode d'identification.

Le cinquième chapitre présente une application importante de la MCV. On montre que la méthode peut être employée comme un outil d'évaluation de différentes configurations d'essais, ce qui permet de comparer ces derniers. La normalisation du critère d'évaluation par rapport à des paramètres liés au calcul (nombre de points de mesure, surface, intensité de l'effort appliqué) est discutée. Une configuration d'essai est également optimisée vis-à-vis du point d'application du chargement. Avec des données simulées auxquelles on a ajouté un bruit simulée numérique, on montre que l'amélioration obtenue en termes d'identifiabilité et de sensibilité réduite au bruit est significative. Enfin, on s'assure que le fait de changer de matériau constitutif ne change que très peu la position optimale de l'effort, ce qui tend à montrer que le résultat est bien intrinsèque à la configuration d'essai.

Le sixième chapitre discute de l'optimisation des configurations d'essai en détails.

L'effet de divers paramètres comme l'angle des plis, la taille de l'échantillon, le point d'application de la charge, les points d'appuis et finalement la forme de l'échantillon sont étudiés séparément, puis ensemble. Pour les cas où plusieurs paramètres sont pris en compte simultanément, on observe la présence de minima locaux. Cette étude permet de discriminer les paramètres influents (principalement : angle des fibres, position des appuis et de l'effort appliqué) de ceux qui le sont moins. Enfin, on vérifie là aussi que le matériau lui-même influence peu la nature de l'optimum.

Le septième chapitre présente une application importante : la caractérisation d'une plaque présentant un dommage local. Ce travail est actuellement en cours au Department of Aerospace Engineering de l'Université de Bristol et au LMPF, laboratoire situé à l'ENSAM de Châlons-en-Champagne. Une adaptation de la MCV avec des propriétés définies par sous-domaines est discutée. Elle est appliquée à l'identification simultanée des rigidités de flexion dans les deux zones séparées de la plaque composite endommagée. Le procédé est validé numériquement en utilisant un exemple de plaque endommagée. La taille et la position de la zone endommagée sont connues a priori et sont utilisées comme données d'entrée pour l'identification simultanée des rigidités inconnues des zones endommagées et non-endomagées. L'influence d'un bruit de mesure est également discutée. De surcroît, on propose un point d'application de charge placé de façon optimale pour garantir la meilleure identifiabilité des caractéristiques de la zone endommagée. Enfin, un procédé de localisation de défaut est également discuté. Il faut cependant souligner que le travail présenté dans ce chapitre est préliminaire à d'autres études possibles, comme une optimisation plus poussée de la configuration d'essai en prenant en compte notamment la position des points d'appui. Par ailleurs, la recherche de la localisation du défaut mériterait plus d'attention, car il faudrait pouvoir décrire de façon plus complète ses contours qu'avec la démarche présentée.

Le huitième chapitre présente finalement les premiers résultats expérimentaux obtenus lors d'essais conduits au LMPF de l'ENSAM de Châlons-en-Champagne. Deux séries de résultats sont comparés: les premiers obtenus dans une situation a priori défavorable, l'autre optimisée en utilisant la procédure présentée dans les chapitres précédents. Les résultats obtenus confirment clairement l'apport prédit par la théorie dans le deuxième cas.

Abstract

The present work deals with the direct identification of bending rigidities of a thin anisotropic composite plate. The inverse identification procedure used here is the virtual fields method which is based on the principle of virtual work. The idea is to determine the unknown parameters from a single test giving a unique heterogeneous strain field. Two new aspects, namely piecewise construction of the virtual fields and noise minimization effect are developed in the present work for a thin composite plate bending problem. Numerical simulations illustrate the relevance of the method and its stability with respect to noisy data. Using the developed procedure, an optimization study of testing configurations is presented and an optimized testing configuration is searched for with respect to different variable parameters such that a more robust and efficient identification is possible with least sensitivity to noise. Also, the developed approach is extended to an identification problem of damaged composite plate. Finally the simulated work is validated with some experimental results.

KEYWORDS: anisotropic composite materials, bending rigidities, piecewise virtual fields method, minimization of noise effect, optimized testing configuration.

Introduction

The present work deals with the direct identification of the bending rigidities of thin composite plates. Composite materials are finding their ever increasing utilization in various industrial applications, thanks to their light weight and at the same time good mechanical resistance. This makes it necessary to be able to determine their mechanical characteristics more accurately and reliably. Unfortunately it not as simple and straightforward as in the case of usual isotropic materials. For usual isotropic materials, the mechanical characterization is based on standard tests that generate presumably homogeneous states of stresses in tested samples of simple shapes. However for anisotropic materials or materials exhibiting multiphase or gradient of properties, heterogeneous stress/strain fields may be obtained. The usual method for characterizing such materials is to perform several tests to deduce reliable average values of constitutive parameters. However, greater is the number of involved parameters, more tests are required to be performed. To overcome these difficulties, exploitation of heterogeneous strain fields is very promising among possible solutions for direct characterization of such materials. It is obtained when response of most or all of the material parameters are involved in a single test. It also permits to design mechanical tests resulting in heterogeneous fields such that all of the material parameters are involved in the response. Thus, identification of greater number of constitutive parameters is possible from reduced number of tests. A drawback of such a procedure is the fact that generally no closed-form solutions are available for the strain/stress fields. This requires a full field (non-contact) measurement method to capture the displacement fields and a specific methodology (referred to as inverse method) to relate the required parameters to the measurements made. Thanks to the recent developments in image processing techniques using CCD cameras and powerful computers, such non-contact full-field measurement techniques are becoming more and more popular and appealing.

The present work is based on the use of so called Virtual Fields Method (VFM). In the present case of elastic anisotropy, VFM is a non-iterative identification procedure for the solution of inverse problems. The present work takes into account two recent developments, notably the piecewise construction of the special virtual fields

and the minimization of noise effect. With these two new aspects, a procedure is developed for the direct identification of the unknown bending rigidities of a thin composite plate. Another novelty of the present work is the optimization of a testing configuration such that more robust and accurate identification is possible. The discussed topics are numerically validated using simulated examples of thin composite plates. An identification case of a damaged composite plate is also studied numerically. In the end, first experimental results are presented that are very encouraging for the future detailed experimental validation.

This doctoral dissertation is presented in the following eight chapters accordingly:

First chapter discusses various available computational strategies for the solution of inverse problems. For the identification of materials constitutive parameters, this chapter presents the methods which are based on the use of overdetermined data or full-field measurement data. In this regard, an overview of different available methods, their fundamental principles and applications are discussed.

Second chapter presents the identification method used in this work which is the virtual fields method. This chapter is devoted to the theoretical development of VFM for a case of thin composite plate bending problems. The main interest and novelty is the piecewise construction of the special virtual fields over the specimen. For an example of complete anisotropy in linear elasticity, the principle of virtual work (PVW) is written with different virtual fields and a system of linear equations is developed. Such a system of linear equations leads to the direct identification of the unknown bending rigidities by exploiting full-field measurement data available on the top surface of a tested specimen.

Third chapter introduces the noise effect on the developed identification system. As the measured full-field data are always noisy, it is important to consider the noise effect on the identification procedure. Hence any identification should be able to appropriately process noisy data such that its adverse effects are minimized. Using simulated noisy data, this chapter discusses the effect of noise minimization such that a more robust identification of the bending rigidities is possible with minimum sensitivity to the noise effect.

Fourth chapter presents a numerical validation of the identification system based on the piecewise VFM with minimized noise effect as developed in the preceding chapter. With the help of a numerical illustration based on bending problem of a thin glass-epoxy composite plate, identification of the bending rigidities is achieved using simulated noisy data. A comparison is also presented in this chapter with an earlier study where a single polynomial expression was used to define the virtual fields over the whole specimen.

Fifth chapter is a further extension to the use of the developed identification procedure. It is used as a tool to classify different given testing configurations on account of better and most robust identifiability especially in the case of noisy data. A comparative study of three different configurations is undertaken using simulated noisy data. A performance based rating of these configurations is established on account of more robust and better identification. Additionally, an optimization case of a testing configuration is also studied. The idea is to explore an optimized position of the force application point such that a more robust and better identification is possible with least sensitivity to noise. A case of carbon-epoxy composite plate is also presented in order to study the effect of using a different material on the location of the optimized force application as noted in the case of a glass-epoxy material.

Sixth chapter presents the major part of this doctoral thesis. It discusses the optimization of testing configurations in detail. To the best of the author's knowledge, such an optimization study is among the few available works in its attempt and treatment. The effect of various parameters like fiber angle, specimen size, location of force application point, location of support points and finally the specimen shape are studied independently and collectively. The idea is to find such an optimal combination of these variable parameters such that a most robust identification is possible with least sensitivity to noise.

Seventh chapter discusses an important application of the piecewise VFM with minimized noise effect for an identification problem of a damaged composite plate. This work contributes to a separate research work dealing with the local loss in stiffness in damaged composite plates, currently under progress in the Department of Aerospace Engineering, University of Bristol and Laboratoire de Mécanique et Procédés de Fabrication (LMPF), ENSAM Châlons. The piecewise VFM is applied here to an illustrative numerical example of a damaged composite plate. The basic interest of this work is to establish a numerically validated procedure for simultaneous rigidity identification in the damaged and undamaged zones of a given composite plate. The effect of an optimized force application point is also studied for better and more robust identification especially of the damaged zone. Using the piecewise VFM, this chapter also discusses a procedure for the defect localization.

Eighth chapter finally presents the first experimental results. Experiments based on the deflectometry method for the full-field slope measurements are conducted by the collaborative research group at LMPF, ENSAM Châlons. The experimental data obtained are processed here to identify the bending rigidities. Experimental results of thin carbon-epoxy composite plates are discussed here for two different types of testing configurations. One is an optimized version of the other regarding the force application point. This chapter briefly recalls the deflectometry method which is a non-contact full-field slope measurement technique. These first experimental results

on the one hand validate the identification ability of the developed piecewise virtual fields method with minimized noise effect. On the other hand they serve to justify the simulated expectations of more robust identification in the case of an optimized configuration.

Chapter 1

Identification of constitutive mechanical properties using heterogeneous deformation fields

1.1 Introduction

The non-contact full-field measurements techniques are becoming more and more popular in the experimental mechanics community thanks to recent developments in image processing techniques using CCD cameras and powerful computers. Various techniques are available in practice such as digital image correlation [4, 5], electronic speckle pattern interferometry [6, 7], moiré and grid methods [8, 9, 10] and defelectometry [11, 2, 12]. In order to benefit the most from the available large amount of experimental data, these experimental procedures are also gradually modified. Now it is possible to directly obtain displacement or strain contours on the specimens surfaces under testing. In the experimental mechanics community, characterization of mechanical response of materials and structures from these measurements is an important issue. The basic interest lies in the fact that using these methods, complex experiments giving rise to heterogeneous deformation fields may be performed. Such heterogeneous fields involve mechanical response of all or most of the materials constitutive parameters. Thus identification of greater number of constitutive parameters is possible from reduced number of such tests. However identification of parameters using such full-field measurements require some suitable procedures since there is generally no direct link between measurements and unknown parameters. Several strategies for the identification of constitutive parameters using the full-field measurements data are currently under progress in different research groups at various French institutes. In the framework of a cooperative research project (GDR 2519 of CNRS), these different techniques are currently being evaluated using some

real experimental data [13]. An overview of the different techniques used in this regard is presented in this chapter.

1.2 Solution of inverse problems using full field data

The constitutive parameter identification problem is usually referred to as *inverse* problem. This problem can be defined as follows. Let us consider a solid of any shape Ω (see Fig 1.1)

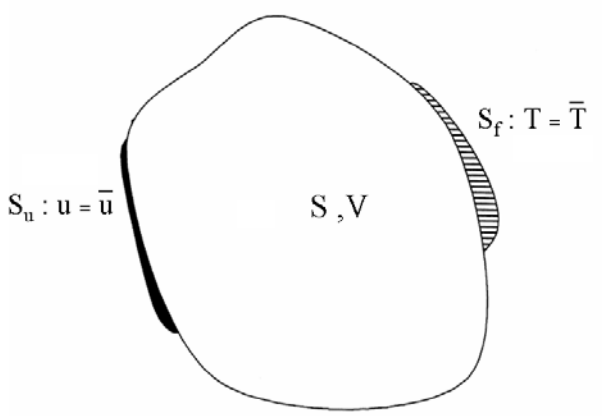

Figure 1.1: Specimen of any shape.

where S, V and t are respectively the external surface, the volume and the thickness of the specimen. For any point M on the specimen external surface S_f, the stress vector $\mathbf{T}(M,n) = \bar{\mathbf{T}}$ is assumed to be known. n is a vector perpendicular to S_f at point M. S_u is the specimen external surface where the displacement field $\mathbf{u}$ is prescribed: $\mathbf{u} = \bar{\mathbf{u}}$. Solution of such an elastic body problem is governed by the following three sets of equations.

- equilibrium equations

$$\begin{cases} div\boldsymbol{\sigma} = & 0 & \text{in } \Omega \\ \boldsymbol{\sigma}\cdot\mathbf{n} = & \bar{\mathbf{T}} & \text{on } S_f \end{cases} \tag{1.1}$$

- kinematic compatibility

$$\begin{cases} \epsilon = & \frac{1}{2}\left(grad\mathbf{u} + grad^t\mathbf{u}\right) & \text{in } \Omega \\ \mathbf{u} = & \bar{\mathbf{u}} & \text{on } S_u \end{cases} \tag{1.2}$$

- constitutive equation

$$\boldsymbol{\sigma} = \quad \boldsymbol{C} : \epsilon \quad \text{in } \Omega \tag{1.3}$$

Here $\mathbf{u}$ defines the displacement vector, ϵ the strain tensor and $\boldsymbol{\sigma}$ the stress tensor. In order to support a well-posed set boundary conditions the surfaces S_u and S_f are such that $S_u \cup S_f = \partial\Omega$ and $S_u \cap S_f = \emptyset$. Hooke tensor $\boldsymbol{C}$ may comprise of constant components in case of homogeneous materials or point-dependent for heterogeneous materials.

Direct problems	
known	unknown
geometry $\bar{\mathbf{u}}$ on S_u $\bar{\mathbf{T}}$ on S_f $\boldsymbol{C}$	$\mathbf{u}$, ϵ $\boldsymbol{\sigma}$

Table 1.1: Known and unknown parameters in case of direct problems.

Inverse problems	
known	unknown
geometry $\bar{\mathbf{T}}$ on S_f $\mathbf{u}$ on Ω *or* $\mathbf{u}$ on $\partial\Omega$	$\boldsymbol{C}$

Table 1.2: Known and unknown parameters in case of inverse problems.

A classical continuum mechanics problem often referred to as *direct problem* is shown in Table 1.1. In this case the geometry of the solid, material parameters and boundary conditions are known whereas the displacement, strain and stress fields are unknown. For such types of direct problems, closed-form solutions are generally not available. Hence, a numerical solution technique (usually the finite element method) is used for solving such problems. However identification of constitutive parameters is addressed in the present work. Such a problem is often referred to as *inverse problem*. It is presented in Table 1.2. In these inverse problems, only the displacement fields on $\partial\Omega$ are known and the material properties are unknown. The strain fields are generally obtained by differentiation of the measured displacement fields. No closed-form solutions for this inverse problem are available in most of

the cases, so the constitutive parameters are not directly related to the measured displacement fields and to the applied forces. So some numerical procedures suitable for the use of full field measurements as input data must be used for solving this problem. For this purpose several methods have been proposed in the recent past to solve this type of inverse problems which include, the finite element model updating (FEMU), the constitutive equation gap method (CEGM), the equilibrium gap method (EGM), the reciprocity gap method (RGM) and the virtual fields method (VFM). All of these identification methods are based on well-known principles of continuum mechanics.

The following section now briefly discusses these different methods one by one.

1.3 Overview of identification methods using full-field data

1.3.1 The finite element model updating

The *finite finite element model updating* (FEMU) is one of the most widely used and straightforward methods. It consists in iteratively performing a finite element analysis such that a set of required constitutive parameters are found which result in the best match of the computed quantities and their experimental counterparts. It is important to note here that full-field data is not necessary for this type of analysis as it can be effectively performed by using any kind of overdetermined data. FEMU technique is based on performing a finite element analysis of a given problem for which the specimen geometry, boundary conditions and loading information, are known in advance and are used as an input. Using an initial estimated set of unknown material parameters to be extracted, a simulated response is obtained. This simulated result is then compared to that of experimental counterpart and the resulting difference is noted. The idea here is to find such a set of parameters which results in best match of the simulated and measured results in terms of minimum difference between the two responses. A general form of such a cost function referred to as weighted least squares estimator can be found in refs. [14, 15].

FEMU has been successfully used in the literature where full-field data measured experimentally is processed. For instance, Mauvoisin [16] identified bending rigidities of thin anisotropic plates by using a measured deflection field at the surface of bent composite and cardboard plates. However, identification could not be performed successfully as the test configuration was not sensitive to all the bending rigidities. In order to ensure the influence of all the bending rigidities on the plate response, Arafeh [17, 18] later used a specially developed test design approach based

on finite element sensitivities. Based on bending test configurations proposed by Arafeh, experiments are performed lately on structural wood based panels [19, 20]. For the identification of viscoelastic parameters, deflection measurements were performed at different times (creep test). The obtained results were found satisfactory for the elastic parameters, whereas for the viscoelastic parameters this study provided only the preliminary results with no comparison to reference values. However, this work remains one of the few incorporating both experimental and numerical aspects. The FEMU has also been applied to identify the elastic-plastic behaviors of metals [15, 21] with very promising results. In a recent work, the influence of local effects on the identification of plate stiffness components is studied using the full-field measurements and the FEMU [22]. In another recent example, plastic material identification is achieved using full-field measurements and the FEMU [23]. Applications of the FEMU is also found in the field of biomechanics, for instance, it is used for the *in vivo* characterization of anisotropic and non linear behavior of human skin [24]. In a similar work, after studying the behavior of woven reinforced composites, *in vitro* characterization of the orthotropic behavior of a patch of dog skin was performed [25, 26].

Finally it may be concluded that the FEMU technique is widely used for different types of situations where full-field measurements are used. However solution of inverse problems through FEMU has some drawbacks:

- it is an iterative procedure and proves to be very time consuming, especially in cases of non-linear constitutive models where iterative calculations are performed for each set of material parameters.

- it requires a load distribution as an input which generally remains unknown and only the resulting global force is measured. Hence the iterative calculations are performed under some assumptions concerning this distribution which may not be very close to actual experimental conditions.

- an estimated set of material parameters are used to initiate the iterative procedure which play an important role in terms of convergence time.

1.3.2 The constitutive equation gap method

The constitutive equation gap method (CEGM) is based on the constitutive equation gap which measures the distance between a given stress field $\boldsymbol{\rho}$ and another stress field computed with a constitutive model and a given displacement field $\boldsymbol{\vartheta}$. A well posed boundary value problem defined by Eq. (1.1,1.2,1.3), is considered here. Let C and S be the sets of kinematically admissible displacement fields and

statically admissible stress fields respectively. The unknown constitutive parameters appearing in the constitutive equation Eq. (1.3) provide a link between strains and stresses therefore it is relevant to consider a cost function based on a notion of *error in constitutive equation* [27]. Such a cost function, based on the error in constitutive equation is defined by using the variational principles of elasticity. This concept was however first introduced by Ladevèze and Leguillon [28] with reference to error estimation in finite element computations. For a linearly elastic constitutive model, a functional measuring the gap in the constitutive law i.e. the constitutive equation gap [27, 29] between the two fields $\boldsymbol{\rho}$ and $\boldsymbol{\vartheta}$ is expressed as

$$F(\boldsymbol{\vartheta}, \boldsymbol{\rho}, \boldsymbol{C}) = \frac{1}{2} \int_{\Omega} (\boldsymbol{\rho} - \boldsymbol{C} : \boldsymbol{\epsilon}[\boldsymbol{\vartheta}]) : \boldsymbol{C}^{-1} : (\boldsymbol{\rho} - \boldsymbol{C} : \boldsymbol{\epsilon}[\boldsymbol{\vartheta}]) dV \tag{1.4}$$

The solution $(\mathbf{u}, \boldsymbol{\sigma})$ to the boundary value problem is given as [27, 29]

$$(\mathbf{u}, \boldsymbol{\sigma}) = \arg \min_{(\vartheta, \rho) \in C \times S} F(\boldsymbol{\vartheta}, \boldsymbol{\rho}, \boldsymbol{C}) \quad \text{and} \quad F(\boldsymbol{\vartheta}, \boldsymbol{\rho}, \boldsymbol{C}) = 0 \tag{1.5}$$

Making use of the available experimental information about displacement and stress fields, the constitutive parameters, for instance the elasticity tensor $\boldsymbol{C}$, can now be identified by minimization of the constitutive equation gap [30, 31] as noted in Eq. (1.6).

$$\boldsymbol{C} = \arg \min_{\boldsymbol{C}^{\star}} J(\boldsymbol{C}^{\star}) \quad \text{with} \quad J(\boldsymbol{C}^{\star}) = \min_{(\vartheta, \rho) \in C \times S} F(\boldsymbol{\vartheta}, \boldsymbol{\rho}, \boldsymbol{C}^{\star}) \tag{1.6}$$

The minimization procedure used here involves an alternate-direction search where a partial minimization with respect to $(\boldsymbol{\vartheta}, \boldsymbol{\rho})$ is followed by a partial minimization with respect to $\boldsymbol{C}^{\star}$. It is important to note that CEGM is applicable to problems where an overdetermined data is available which may not be a full-field measurement. Several studies of this kind are performed especially in the context of modal updating from vibrational data such that the FE models agree best with their measurements on the real structure [28, 32, 33, 34]. However full-field measurement data may well be incorporated and used in this procedure [35, 36].

1.3.3 The equilibrium gap method

The *equilibrium gap method* (EGM) [37, 38] has been proposed and developed to identify elastic fields or a damage field by making use of a measured displacement field in Ω. The approach is valid for the cases where the constitutive heterogeneity is in the form of a scalar and isotropic damage field $D(x)$ [39]. In this case of damage description, the Poisson's ratio remains constant contrary to the Lamé coefficients which can be written as $\lambda(x) = \lambda_0[1 - D(x)]$ and $\mu(x) = \mu_0[1 - D(x)]$ where λ_0 and μ_0 are the coefficients of the undamaged material.

As most of the measurements techniques yield data on a regular mesh of points, it is assumed here that the displacement data is available on a regular measurement grid. This allows to build a FEM mesh using eight-noded quadratic square elements within plane-stain or plane-stress framework. The resulting mesh is such that the nodes are coincident with the measuring points. Such an assumption leads to a specific formulation where only middle nodes are considered. Now, assuming a constant damage parameter D_e for a given element e, the elementary stiffness matrix gives

$$[K_{me}](D_e) = (1 - D_e) \times [K_{me0}] \tag{1.7}$$

where $[K_{me0}]$ represents the elementary stiffness matrix of an undamaged element. Similarly, the strain energy E_{me} of element e is given below with $\{u_e\}$ representing the nodal displacement column vector

$$[E_{me}](D_e) = \frac{(1 - D_e)}{2} {u_e}^t [K_{me0}]\{u_e\} \tag{1.8}$$

The FEM equilibrium equations are now used for the identification of this damage distribution. For this purpose only the midside nodes, shared by two adjacent elements denoted as 1 and 2, are considered. In the absence of external loads at the adjacent nodes referred to as 12, the FEM equilibrium equations write as follows

$$\frac{\partial E_{m12}}{\partial u_{12}}(D_1, D_2) = 0 \tag{1.9}$$

Here, $E_{m12}(D_1, D_2) = E_{m1}(D_1) + E_{m2}(D_2)$, where D_1, D_2 are the damage variables in elements 1 and 2. Similarly, if the same condition is written for all the available midside nodes, a set of linear equations is obtained where unknown damage parameters are linked to the known nodal displacements. However, Eq. (1.9) is not strictly satisfied in practice and a residual force $\mathbf{F}_r$ is obtained which is expressed as

$$\mathbf{F}_r(\hat{D_1}, \hat{D_2}) = \frac{\partial E_{m1}}{\partial u_{12}}(\hat{D_1}) + \frac{\partial E_{m2}}{\partial u_{12}}(\hat{D_2}) \tag{1.10}$$

where $\hat{D_1}$, $\hat{D_2}$ represent trial values of the unknown damage variables. Due to this residual the proposed method is referred to as the equilibrium gap method. Minimization of the residuals $\mathbf{F}_r$ lead to the eventual identification of a damage field by using a know displacement field. The procedure can be used in other cases. For instance, in the case of micro-electro-mechanical systems (MEMS), this method has been recently successfully employed for simultaneous identification of elastic properties and loading fields using the measured displacement fields [40, 41, 42, 43].

1.3.4 The reciprocity gap method

The *reciprocity gap method* (RGM) is proposed for the identification of unknown distribution of elastic moduli using full-field measurements. It assumes that the displacement distribution on the boundary, induced by a known applied static load, is measurable in the form of full-field data. Let (ξ, ϕ) denote the known displacements and tractions on the boundary $\partial\Omega$ of an elastic body in domain Ω. From such displacement-force boundary data, the interior distribution of the elastic tensor $\boldsymbol{C}^\star(x)$ may be reconstructed and a reciprocity gap functional is defined from the principle of virtual work [27, 29, 30]. A *reciprocity gap functional* is now defined here with the help of an *adjoint state*. An adjoint state represents an elastic body occupying the same region Ω but a distinct elastic tensor distribution $\boldsymbol{C}(x)$. Let $\tilde{u}$ denote the displacement field induced by a traction distribution $\tilde{\phi}$ on $\partial\Omega$ of this adjoint state. Using the principle of virtual work, the identities for the experimental and adjoint state are obtained and represented as

$$\int_\Omega \boldsymbol{\epsilon}(u^\star) : [\boldsymbol{C}^\star - \boldsymbol{C}] : \boldsymbol{\epsilon}(\tilde{u}) dV = \int_{\partial\Omega} (\phi \cdot \tilde{u} - \tilde{\phi} \cdot \xi) dS = R(\boldsymbol{C}^\star - \boldsymbol{C}; \tilde{u}, u) \qquad (1.11)$$

The above Eq. (1.11) defines the *reciprocity gap* $R(\boldsymbol{C}^\star - \boldsymbol{C}; \tilde{u}, u)$. The term reciprocity gap comes from the fact the same functional may be derived by using Maxwell-Betti reciprocity theorem for the two states $(u, \tilde{u})$. The theorem is based on the assumption that both the states refer to the same elasticity tensor and thus a reciprocity gap occurs when the assumption is no longer valid [27]. Thus for any adjoint state $(\tilde{u}, \tilde{\phi})$, the *reciprocity gap* $R(\boldsymbol{C}^\star - \boldsymbol{C}; \tilde{u}, u)$ is a known function of the experimental data (ξ, ϕ), such that

$$R(\boldsymbol{C}^\star - \boldsymbol{C}; \tilde{u}, u) = 0 \quad (\forall \phi) \qquad (1.12)$$

For any given adjoint load $\tilde{\phi}$, the above Eq. (1.12) results in an independent scalar relationship with respect to the unknown distribution $\boldsymbol{C}^\star$ or to the parameters involved in its definition. Using the RGM, theoretical studies [44, 45] based on the identification of $\boldsymbol{C}^\star$ have been achieved by using a linearized version of Eq. (1.11). In such linearized inversion problems the adjoint states were chosen according to a procedure initially proposed by Calderon [46]. The main idea of this technique is the fact that the right hand side of Eq. (1.11) yields the spatial Fourier transform of $\boldsymbol{C}^\star - \boldsymbol{C}$.

The reciprocity gap method has been extended to the identification of the flexure rigidities for Love-Kirchhoff plates [47]. However, RGM is mainly employed for the crack identification problems. In such applications an elastic body with known elastic moduli $\boldsymbol{C}$ and a traction-free embedded crack defined by the open surface Γ

is considered. The corresponding inverse problem thus consists in reconstructing Γ from boundary measurements (ξ, ϕ). Now disregarding the possibility of the crack faces coming into mutual contact, the reciprocity gap functional of the problem can be formulated [27, 29]. Such a reciprocity gap functional has been successfully used for the identification of planar cracks [48, 49, 50]. These studies demonstrate that it is possible to choose such families of adjoint states $(\tilde{\xi}, \tilde{\phi})$ which permit to identify a normal direction to the crack plane, position of this plane and the crack itself. A variant of the approach based on instantaneous version of the reciprocity gap has also been proposed for the case of elastodynamic measurements [51].

1.3.5 The virtual fields method

This method can be applied in cases where a full-field strain measurement is available. Such a strain field is in fact derived from the experimental full-field displacement measurements. The basic idea of the VFM lies in writing the global static equilibrium of the tested specimen with the principle of virtual work. Considering a plane-stress state with no body forces, the principle of virtual work writes as follows

$$-\int_V \boldsymbol{\sigma} : \boldsymbol{\varepsilon}^\star dV + \int_{S_f} \mathbf{T} \cdot \mathbf{u}^\star dA = 0 \quad \forall \ \mathbf{u}^\star, \boldsymbol{\varepsilon}^\star; K.A \tag{1.13}$$

where $\mathbf{u}^\star$ represents virtual displacement field from which the corresponding virtual strain field $\boldsymbol{\varepsilon}^\star$ is derived. These virtual fields are supposed to be kinematically admissible. Now it is required to write the principle of virtual work with as many different and independent virtual fields as the unknowns introduced into the constitutive equations. If at least as many virtual fields as the unknown parameters are chosen then a linear system of equations is obtained. This system provides the unknown parameters after inversion. Since the birth of VFM [52], this approach has then been simulated and applied to various cases of composite materials characterization. For instance, it has been successfully applied to bending problems either in statics [53, 54, 55], or in dynamics [56, 57, 58]. It has been used for in-plane characterization [59, 60] and also for through-thickness composite characterization both in the case of linear elastic response [61, 62, 63] and a non-liner response [64].

An important issue here is the choice and construction of virtual fields, since these fields directly influence the degree of independence of the equations in the linear system of equations. Also there exist an infinity of virtual fields verifying the principle of virtual work. In previous studies, for the sake of simplicity, such fields were manually constructed in the form of polynomials over the whole of specimen with the only condition of its kinematic admissibility. Such an intuitive selection was based on trial and error approach such that the different equations of the linear

system remain sufficiently independent. The independence of the equations is in fact directly related to the sensitivity of the identified parameters when actual noisy data of the measured displacement field is processed. It is therefore essential to obtain such virtual fields which lead to a set of independent equations.

This approach has been greatly improved in recent past, thanks to automatic construction of *special* virtual fields [65, 66]. The novelty here is to find such virtual fields that the coefficient of only a corresponding unknown in the linear system of equation is one and the remaining are zero. The unknown is then directly identifiable with the virtual work of the loading. Such virtual fields are referred to as special. However in this case also there exists an infinite choice for selection of such special virtual fields. This freedom has been exploited to find some more relevant special virtual fields especially in terms of sensitivity to the noisy data. In this regard a first strategy was proposed which reduces the effect of random noise onto the identified parameters [67, 3]. Recently a more efficient procedure has been proposed which results in an automatic construction of unique special virtual fields which leads to lowest sensitivity of the identified parameters to noise [68].

Another important development is the introduction of piecewise construction of virtual fields [69]. Instead of defining the fields by the same expression over the whole specimen (as in earlier studies), they are defined in subregions or piecewise over the specimen. On one hand it gives greater flexibility when a multiphase material is considered. On the other hand it allows to construct the fields using lower-degree polynomials as shape functions in each subregions. Recalling that when a same polynomial expression is defined over the whole of specimen greater degree polynomial is required which results in magnification of the adverse effects of noisy data onto the identification of parameters. In recent examples VFM has also been used to directly identity the damage behaviour of composite materials [70] in addition to further extending the application in case of elasto-plastic constitutive parameter identification [71].

With all these improvements, VFM becomes much easier to implement and reliable especially for composite material characterization involving the use of full-field measurements [72]. The main advantages of the VFM lies in the fact that it is a non-iterative procedure capable of direct identification of the unknown parameters by using a full-field data [73]. Also, the influence of boundary conditions (i.e. the knowledge of loading distribution over the boundary) can be avoided by choosing such virtual fields in which the virtual work involves only the resulting forces [67].

1.4 Conclusion

Recent advances in the sensing technology and image processing have led to the development of various techniques to measure displacement or strain fields over a mechanically tested specimen. This has also resulted in parallel development of different computational strategies which enable to process the measured fields in order to identify the materials constitutive parameters. This chapter presents these various available computational techniques. Among the different methods studied it is observed that most of these share a common inconvenience of iterative calculations in addition to the use of an initial guess of the unknown parameters.

The present work is based on the virtual fields method. It permits to avoid some of the above noted inconveniences and thus be considered as an alternative to the classical identification methods. Taking into account the recent improvements in the VFM notably the use of piecewise special virtual fields with minimized noise effect, direct identification of bending rigidities of a thin composite plate is studied here. The following chapter now discusses in detail the piecewise VFM method applied to plate bending problems.

Chapter 2

The piecewise virtual fields method in plate bending problems

2.1 Introduction

The virtual fields method is based on the principle of virtual work [52]. It consists first in writing the global static equilibrium of the specimen considering plane stress state and no body forces as

$$\underbrace{-\int_V \boldsymbol{\sigma} : \boldsymbol{\varepsilon}^\star dV}_{Internal\ Virtual\ Work:\ W_i^*} + \underbrace{\int_{S_f} \mathbf{T}\cdot\mathbf{u}^\star dA}_{External\ Virtual\ Work:\ W_e^*} = 0 \quad \forall\ \mathbf{u}^\star, \boldsymbol{\varepsilon}^\star; K.A \tag{2.1}$$

where:

- V is the volume of the specimen under study,
- S is the surface over which the global equilibrium is written, and over which full-field measurements are assumed to be available,
- S_f is the boundary surface of the specimen,
- $\boldsymbol{\sigma}$ is the actual stress field over surface S ,
- $\mathbf{T}$ is the traction on the surface S_f,
- $\mathbf{u}^*$ is a virtual displacement field, i.e. an imagined displacement field which respects the boundary conditions, referred to as kinematically admissible (K.A.),
- ϵ^* is the virtual strain field derived from $\mathbf{u}^*$,
- $':'$ denotes dot product between two $2nd$ rank tensors,
- $'.'$ denotes dot product between two $1st$ rank tensors.

It is important to note that the Eq. (2.1) is valid for any K.A. virtual field. The VFM takes advantage of this property by writing the above equation with as many different and independent K.A. virtual fields as unknowns [52]. It will be shown below that this leads to the direct extraction of the unknown parameters.
In the present case of plate bending with point loadings, using the theory of thin anisotropic plates [74], Eq. (2.1) becomes

$$-\int_S M^t \cdot K^* dA \quad + \quad W_e^* = 0 \tag{2.2}$$

with

$$M = \begin{bmatrix} M_x \\ M_y \\ M_s \end{bmatrix} \quad , \quad K^* = \begin{bmatrix} k_x^* \\ k_y^* \\ k_s^* \end{bmatrix} \quad , \quad W_e^* = \sum_{i=1}^{n} F_i.w^*$$

where

- M is the bending moment field on the surface S,
- w^* is the virtual deflection field, which is kinematically admissible (KA),
- K^* is the virtual curvature field derived from w^*,
- $F_i, i = 1, ..., n$ are applied loading forces,
- the rule of contracted indices is used: $xx \rightarrow x$, $yy \rightarrow y$, $xy \rightarrow s$

For thin plate bending, the moment-curvature relationship is written as

$$\begin{bmatrix} M_x \\ M_y \\ M_s \end{bmatrix} = \begin{bmatrix} D_{xx} & D_{xy} & D_{xs} \\ D_{xy} & D_{yy} & D_{ys} \\ D_{xs} & D_{ys} & D_{ss} \end{bmatrix} \begin{bmatrix} k_x \\ k_y \\ k_s \end{bmatrix} \tag{2.3}$$

Here, the D_{ij}'s are the unknown bending rigidities and the k_i's are the curvatures which are second derivatives of the deflection w, as

$$k_x = -\frac{\partial^2 w}{\partial x^2} \; ; \; k_y = -\frac{\partial^2 w}{\partial y^2} \; ; \; k_s = -2\frac{\partial^2 w}{\partial x \partial y} \tag{2.4}$$

The objective of the study is to identify the bending rigidities D_{xx}, D_{yy}, D_{ss}, D_{xy}, D_{xs} and D_{ys} from the heterogeneous strain fields produced on the top surface of a bent plate recalling that no closed form solution of the actual deflection and curvature field is available in the general case. It is assumed here in the present case of thin plate bending problem that the D_{ij} are constant over the whole plate. In Chapter 7 an identification problem is studied where the plate comprises of two zones with different D_{ij}. Now, substitution of M and K^* in Eq. (2.2) gives

$$\int_S \left(M_x k_x^* + M_y k_y^* + M_s k_s^* \right) dA = \sum_{i=1}^{n} F_i \cdot w_i^* \tag{2.5}$$

also, using Eq. (2.3) the above expression expands to

$$\int_S \Big[\left(D_{xx}k_x + D_{xy}k_y + D_{xs}k_s\right) k_x^* + \left(D_{xy}k_x + D_{yy}k_y + D_{ys}k_s\right) k_y^* + \left(D_{xs}k_x + D_{ys}k_y + D_{ss}k_s\right) k_s^* \Big] dA = \sum_{i=1}^{n} F_i \cdot w_i^* \quad (2.6)$$

Considering the constant bending rigidities over the whole surface, and rearranging the terms we get

$$D_{xx}\int_S k_x k_x^* dA + D_{yy}\int_S k_y k_y^* dA + D_{ss}\int_S k_s k_s^* dA + D_{xy}\int_S \left(k_x k_y^* + k_y k_x^*\right) dA + D_{xs}\int_S \left(k_x k_s^* + k_s k_x^*\right) dA + D_{ys}\int_S \left(k_y k_s^* + k_s k_y^*\right) dA = \sum_{i=1}^{n} F_i \cdot w_i^* \quad (2.7)$$

Finally the above equation is written as follows

$$D_{xx}I_{xx} + D_{yy}I_{yy} + D_{ss}I_{ss} + D_{xy}I_{xy} + D_{xs}I_{xs} + D_{ys}I_{ys} = \sum_{i=1}^{n} F_i \cdot w_i^* \quad (2.8)$$

where

$$\begin{cases} I_{xx} = \int_S k_x k_x^* dA \quad ; \quad I_{xy} = \int_S \left(k_x k_y^* + k_y k_x^*\right) dA \\ I_{yy} = \int_S k_y k_y^* dA \quad ; \quad I_{xs} = \int_S \left(k_x k_s^* + k_s k_x^*\right) dA \\ I_{ss} = \int_S k_s k_s^* dA \quad ; \quad I_{ys} = \int_S \left(k_y k_s^* + k_s k_y^*\right) dA \end{cases} \quad (2.9)$$

At this point, it is required to write the above global equilibrium equation with some particular virtual fields. If as many virtual fields as unknown rigidities are found, a linear system of equation is obtained. For identification purposes, six different virtual fields are required which are represented as $\{w^{*\alpha},\ k^{*\alpha}\}$, where $\alpha = a, b, c, d, e, f$ represent D_{xx}, D_{yy}, D_{ss}, D_{xy}, D_{xs} and D_{ys} respectively. Finally the system of linear equations is represented in a matrix form as follows

$$\begin{bmatrix} I_{xx}^a & I_{yy}^a & I_{ss}^a & I_{xy}^a & I_{xs}^a & I_{ys}^a \\ I_{xx}^b & I_{yy}^b & I_{ss}^b & I_{xy}^b & I_{xs}^b & I_{ys}^b \\ I_{xx}^c & I_{yy}^c & I_{ss}^c & I_{xy}^c & I_{xs}^c & I_{ys}^c \\ I_{xx}^d & I_{yy}^d & I_{ss}^d & I_{xy}^d & I_{xs}^d & I_{ys}^d \\ I_{xx}^e & I_{yy}^e & I_{ss}^e & I_{xy}^e & I_{xs}^e & I_{ys}^e \\ I_{xx}^f & I_{yy}^f & I_{ss}^f & I_{xy}^f & I_{xs}^f & I_{ys}^f \end{bmatrix} \begin{bmatrix} D_{xx} \\ D_{yy} \\ D_{ss} \\ D_{xy} \\ D_{xs} \\ D_{ys} \end{bmatrix} = \sum_{i=1}^{n} \begin{bmatrix} F_i.w_i^{*a} \\ F_i.w_i^{*b} \\ F_i.w_i^{*c} \\ F_i.w_i^{*d} \\ F_i.w_i^{*e} \\ F_i.w_i^{*f} \end{bmatrix} \quad (2.10)$$

Now an important issue of the VFM is the selection of these virtual fields among infinite possibilities. Previously it has been shown that there exist certain virtual

fields called *special* virtual fields [66] that render the matrix of linear system Eq. (2.10) equal to unity

$$\begin{bmatrix} I^a_{xx} & I^a_{yy} & I^a_{ss} & I^a_{xy} & I^a_{xs} & I^a_{ys} \\ I^b_{xx} & I^b_{yy} & I^b_{ss} & I^b_{xy} & I^b_{xs} & I^b_{ys} \\ I^c_{xx} & I^c_{yy} & I^c_{ss} & I^c_{xy} & I^c_{xs} & I^c_{ys} \\ I^d_{xx} & I^d_{yy} & I^d_{ss} & I^d_{xy} & I^d_{xs} & I^d_{ys} \\ I^e_{xx} & I^e_{yy} & I^e_{ss} & I^e_{xy} & I^e_{xs} & I^e_{ys} \\ I^f_{xx} & I^f_{yy} & I^f_{ss} & I^f_{xy} & I^f_{xs} & I^f_{ys} \end{bmatrix} = \begin{bmatrix} 1 & 0 & 0 & 0 & 0 & 0 \\ 0 & 1 & 0 & 0 & 0 & 0 \\ 0 & 0 & 1 & 0 & 0 & 0 \\ 0 & 0 & 0 & 1 & 0 & 0 \\ 0 & 0 & 0 & 0 & 1 & 0 \\ 0 & 0 & 0 & 0 & 0 & 1 \end{bmatrix} \tag{2.11}$$

In this case Eq. (2.10) leads to direct identification of unknown rigidities making use of Eq. (2.11). The idea is then to use the principle of virtual work with these special virtual fields such that five out of the total six terms in each row are zero whereas the sixth one is equal to unity in Eq. (2.10). Thus direct determination of the parameter is made whose coefficient is 1 in Eq. (2.11). Similarly, using six different special virtual fields, all the six unknown parameters are identified one by one. Finally, the linear system of Eq. (2.10) becomes

$$\begin{bmatrix} D_{xx} \\ D_{yy} \\ D_{ss} \\ D_{xy} \\ D_{xs} \\ D_{ys} \end{bmatrix} = \sum_{i=1}^{n} \begin{bmatrix} F_i.w_i^{*a} \\ F_i.w_i^{*b} \\ F_i.w_i^{*c} \\ F_i.w_i^{*d} \\ F_i.w_i^{*e} \\ F_i.w_i^{*f} \end{bmatrix} \tag{2.12}$$

In the present section the VFM using special virtual fields is recalled [66] and presented. Now the following section discusses one of the novelties of the present work i.e. the piecewise construction of special virtual fields applicable to thin plate bending problems.

2.2 Construction of the virtual fields

2.2.1 Introduction

So far it has been established that the unknown parameters can be directly identified by making use of special virtual fields or specifically special virtual deflection fields w^α (with $\alpha = a, b, c, d, e, f$), while writing external virtual work as per principle of virtual work (refer to Eq. (2.12)). Now in order to construct such special fields there are certain issues which are discussed below.

2.2.2 Virtual deflection fields defined by virtual elements

Any set of independent continuous functions can be used as a basis for expressing and development of virtual displacement fields. Previously polynomials defined over the whole of specimen's geometry were effectively used [3]. The present work introduces a piecewise construction of special virtual fields over a bent plate. This technique was first introduced in case of membrane loadings for multimaterials [69]. Such piecewise virtual fields are referred to here as *virtual elements*. The idea is to use similar shape functions as those used in the finite element method to describe the virtual field within each element. They are finally expressed as a function of parameters which are some generalized virtual displacements (deflection, slopes or curvatures) at each node of a virtual mesh of the plate.

One of the advantages is the freedom to construct either one or many piecewise virtual fields over the whole geometry of specimen. This gives an important leverage when a multiphase material is to be characterized [69]. In these cases such separate piecewise virtual fields are constructed for different zones having different properties within a given specimen and their respective properties can be identified. Also, the degree of shape function is lesser as compared to the use of polynomial defined over the whole specimen. On account of earlier results discussed in ref. [3], it is expected to reduce the influence of noise which is closely related to the degree of the polynomials used for expanding the virtual fields.

It is important to note that the principle of virtual fields is valid for virtual displacement fields which are continuous over the whole specimen. In the case of plate bending, it means that the deflection and its derivatives (the slopes) computed along any direction must be continuous. This latter condition is required to ensure the continuity of the in-plane virtual displacement field according to the well known Love-Kirchhoff assumption [74]. Such a condition is generally not verified in many elements used in the finite element method for bending problems. As a result some in-plane displacement components are not continuous at the boundary of the elements [75]. The idea here is to fulfill this requirement in such a way that the principle of virtual field is strictly verified, thus avoiding any problem when this principle is used for identification purposes. Very limited number of shape functions verify such an in-plane displacement continuity in the case of plate bending [75]. In fact it can be shown that four degrees of freedom (dof) must be used at each node of rectangular elements to fulfill this requirement: $w, \theta_x \left(= \frac{\partial w}{\partial y}\right), \theta_y \left(= \frac{\partial w}{\partial x}\right), \theta_{xy} \left(= \frac{\partial^2 w}{\partial x \partial y}\right)$. Only the fourth dof ($\theta_{xy}$) ensures the slope continuity in any direction. Such a continuity is not obtained when only the first three dofs are used. This type of so-called Hermite16 element [75] defined by four nodes with four dofs at each node is therefore used in the present study, refer to Fig 2.1. It should be emphasized that the in-plane

displacements are no longer continuous if the element is a parallelogram [76]. However, a triangular element ensuring slope continuity with six dof at each of the three nodes can also be used [75, 76]. Such a triangular element is not considered in the present work to avoid additional computational complexities.

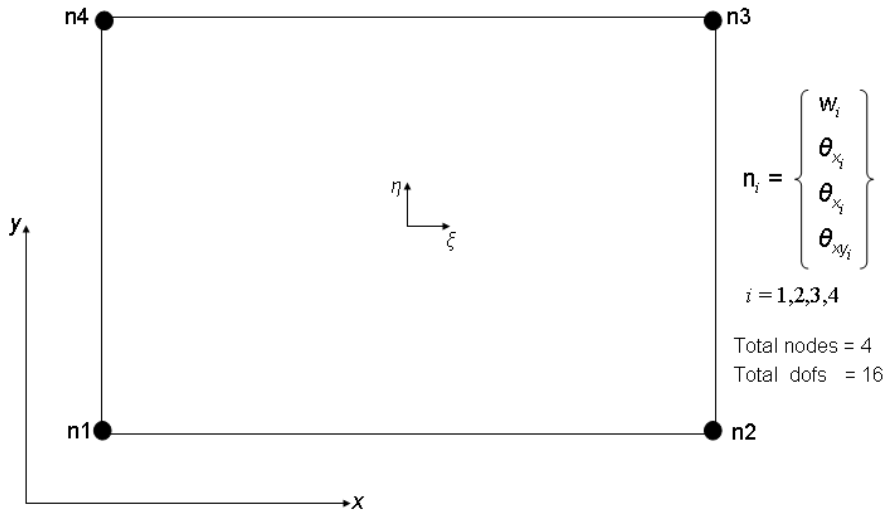

Figure 2.1: A quadrilateral 4 node element with 4 dofs at each node.

For notation purposes hereafter, let $| col >$ denotes a column vector and $< lin |$ represents a line vector. The matrix multiplication $< lin \,||\, col >$ leads to a scalar and $| col >< lin |$ results in a rectangular matrix. Now, let $< f(x, y) |$ represent the chosen shape function and $| Y^* >$ a vector whose components are in fact all the nodal dofs virtual values. This vector is *a priori* unknown and must be determined to completely define the virtual field. In case of *one* virtual element used, it is a column vector of 1×16. The length of vector $| Y^* >$ is denoted by N which depends upon the total number of virtual elements. Say, p and q denote the number of virtual elements respectively along x and y directions along the specimen. $p \times q$ gives the total number of the virtual elements which are defined in the form of a regular mesh over a given specimen. Then length N of vector $| Y^* >$ is determined as, $N = 4(p+1)(q+1)$. For example, in case of 1, 2×2 or 3×3 total virtual elements defined over the specimen's surface corresponding N is 16, 36 or 64 respectively. Fig 2.2 illustrates the use of a total of $6 \times 6 = 36$ piecewise virtual elements which are superimposed over a given specimen shape in a regular mesh form. The total number of virtual dofs, N, in this case is 196.

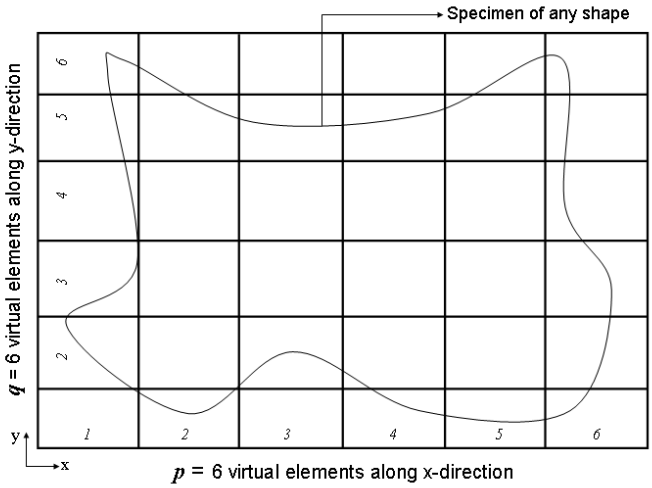

Figure 2.2: An illustration of total $6 \times 6 = 36$ piecewise virtual elements, superimposed in a regular mesh form over a given specimen shape.

Now, Eq. (2.13) below represents $\mid Y^* >$ in case of only one virtual element, however an assembly of such nodal dofs is required in case of more than one virtual elements used

$$\mid Y^* >= \begin{pmatrix} w(1,1) \\ \theta_x(1,2) \\ \theta_y(1,3) \\ \theta_{xy}(1,4) \\ . \\ . \\ . \\ w(4,1) \\ \theta_x(4,2) \\ \theta_y(4,3) \\ \theta_{xy}(4,4) \end{pmatrix} \tag{2.13}$$

The virtual deflection field in case of one element is written as follows

$$w^*(x,y) = \quad < f(x,y) \mid\mid Y^* > \tag{2.14}$$

Finally the unknown vector of virtual dofs, $\mid Y^* >$, is determined using the equations discussed below.

2.2.3 Computation of virtual curvature fields

From the virtual deflection field given by Eq. (2.14), the virtual curvature fields may be calculated as

$$\left\{\begin{array}{lrcl} k_x^*(x,y) = & -\frac{\partial^2 w^*}{\partial x^2} & = & < b_x(x,y) \,||\, Y^* > \\ k_y^*(x,y) = & -\frac{\partial^2 w^*}{\partial y^2} & = & < b_y(x,y) \,||\, Y^* > \\ k_s^*(x,y) = & -2\frac{\partial^2 w^*}{\partial x \partial y} & = & < b_s(x,y) \,||\, Y^* > \end{array}\right. \tag{2.15}$$

here $< b_x(x,y) \mid$, $< b_y(x,y) \mid$and $< b_s(x,y) \mid$ are vectorial functions of length N and are second derivatives of shape function as

$$\left\{\begin{array}{rcl} < b_x(x,y) \mid & = & -\frac{\partial^2 < f(x,y) \mid}{\partial x^2} \\ < b_y(x,y) \mid & = & -\frac{\partial^2 < f(x,y) \mid}{\partial y^2} \\ < b_s(x,y) \mid & = & -2\frac{\partial^2 < f(x,y) \mid}{\partial x \partial y} \end{array}\right. \tag{2.16}$$

2.2.4 Computation of integrals

In order to compute the integrals involved in Eq. (2.9), the actual curvatures are needed. For this, a discrete slope field (θ_x and θ_y) measured over the tested plate at n_e different points whose coordinates are represented by x_g and y_g is used. From this slope field, the actual curvatures k_x, k_y and k_s are now derived using Eq. (2.4). In this regard, Section 8.3.4 discusses in detail the procedure to obtain the required curvature fields from the measured slope fields on the surface of a tested plate. Now each term of Eq. (2.9) is calculated as

$$\left\{\begin{array}{lrcl} I_{xx} = & \int_S k_x k_x^* dA & = & < B_{xx} \,||\, Y^* > \\ I_{yy} = & \int_S k_y k_y^* dA & = & < B_{yy} \,||\, Y^* > \\ I_{ss} = & \int_S k_s k_s^* dA & = & < B_{ss} \,||\, Y^* > \\ I_{xy} = & \int_S \left(k_x k_y^* + k_y k_x^*\right) dA & = & < B_{xy} \,||\, Y^* > \\ I_{xs} = & \int_S \left(k_x k_s^* + k_s k_x^*\right) dA & = & < B_{xs} \,||\, Y^* > \\ I_{ys} = & \int_S \left(k_y k_s^* + k_s k_y^*\right) dA & = & < B_{ys} \,||\, Y^* > \end{array}\right. \tag{2.17}$$

Here, due to the discrete nature of the curvature field, the integrals are evaluated using rectangular method. It is a simple numerical integration technique well suited to problems when a discrete data is available in the form of a regular mesh. As in the present case the specimen may be considered to be superimposed by a regular mesh of identical small rectangles such that their centers correspond to the measuring points. Thus the above integrals may be computed numerically as discrete sums.

$$
\begin{cases}
B_{xx} = & \frac{S}{n_e} \sum_{i=1}^{n_e} k_{x_i}(x_g, y_g)_i \; b_x(x_g, y_g)_i \\
B_{yy} = & \frac{S}{n_e} \sum_{i=1}^{n_e} k_{y_i}(x_g, y_g)_i \; b_y(x_g, y_g)_i \\
B_{ss} = & \frac{S}{n_e} \sum_{i=1}^{n_e} k_{s_i}(x_g, y_g)_i \; b_s(x_g, y_g)_i \\
B_{xy} = & \frac{S}{n_e} \sum_{i=1}^{n_e} k_{x_i}(x_g, y_g)_i \; b_x(x_g, y_g)_i + k_{y_i}(x_g, y_g)_i \; b_y(x_g, y_g)_i \\
B_{xs} = & \frac{S}{n_e} \sum_{i=1}^{n_e} k_{x_i}(x_g, y_g)_i \; b_x(x_g, y_g)_i + k_{s_i}(x_g, y_g)_i \; b_s(x_g, y_g)_i \\
B_{ys} = & \frac{S}{n_e} \sum_{i=1}^{n_e} k_{y_i}(x_g, y_g)_i \; b_y(x_g, y_g)_i + k_{s_i}(x_g, y_g)_i \; b_s(x_g, y_g)_i
\end{cases}
\tag{2.18}
$$

Let us now examine how to determine the vector of unknown virtual dofs, $\mid Y^* >$.

2.3 Boundary conditions imposed to virtual deflection field

As the virtual deflection field is kinematically admissible it must respect the boundary conditions (BCs). Thus for a given number of supports n_s, the virtual deflection must be zero at these locations. The BCs are represented as linear constraints imposed to $\mid Y^* >$ such that the virtual deflection fields verify the BCs at these points of support. Such linear constraints are written as

$$
w^*(x,y)_i = \; < f(x,y)_i \mid\mid Y^* > \; = 0 \;\; ; \qquad \text{with } 1 \leq i \leq n_s \tag{2.19}
$$

This condition provides a first set of equations that will be used to determine $\mid Y^* >$.

2.4 Constraints imposed due to special virtual fields

With reference to Eq. (2.11) six additional constraints are imposed to $\mid Y^* >$. Recalling that for a particular special virtual field only one of the I_{ij} is equal to unity while the remaining five are zero. Thus for each special virtual deflection field $w^{*\alpha}$ corresponds a special virtual deformation field $\mid Y^{*\alpha} >$, with $\alpha = a, b, c, d, e$ and f. For instance, the six constraints for finding D_{xx} are written as

$$\begin{cases} < B_{xx} \,||\, Y^{*a} > & = 1 \\ < B_{yy} \,||\, Y^{*a} > & = 0 \\ < B_{ss} \,||\, Y^{*a} > & = 0 \\ < B_{xy} \,||\, Y^{*a} > & = 0 \\ < B_{xs} \,||\, Y^{*a} > & = 0 \\ < B_{ys} \,||\, Y^{*a} > & = 0 \end{cases} \tag{2.20}$$

Similarly, by switching the position of "1" vertically downwards and replacing its earlier position by "0" we get a new set of six constraints for special virtual deflection field "*b*" and so on for the rest of the unknown rigidities. Thus for the six parameters to be identified there are six sets of above constraints with corresponding $\mid Y^{*a} >$, $\mid Y^{*b} >$, $\mid Y^{*c} >$, $\mid Y^{*d} >$, $\mid Y^{*e} >$ and $\mid Y^{*f} >$, which are in fact the required unknown virtual dofs.

2.5 Identification of unknown rigidities

Once the above six virtual dofs ($\mid Y^{*\alpha} >$) are known, using the additional equations given below (obtained from Eq. (2.12) and Eq. (2.14)), the six unknown bending rigidities are obtained directly as follows

$$\begin{cases} D_{xx} & = & < R \,||\, Y^{*a} > \\ D_{yy} & = & < R \,||\, Y^{*b} > \\ D_{ss} & = & < R \,||\, Y^{*c} > \\ D_{xy} & = & < R \,||\, Y^{*d} > \\ D_{xs} & = & < R \,||\, Y^{*e} > \\ D_{ys} & = & < R \,||\, Y^{*f} > \end{cases} \tag{2.21}$$

where

$$< R \mid = \sum_{i=1}^{n} F_i < f(x,y)_i \mid \tag{2.22}$$

Here we may observe that the unknowns $\mid Y^{*\alpha} >$ comprise of $4(p+1)(q+1)$ components depending upon the total number of virtual elements defined over specimen geometry as discussed earlier. Considering an exemplary case of plate bending with three supports, only 9 equations are available (six from the use of special virtual fields and three from BCs). This makes it an undeterminate problem with more unknowns than equations at hand even with $p = q = 1$. In fact the additional equations are obtained here from the minimization of noise effect on identified stiffnesses introduced in ref. [68]. Chapter 3 discusses this issue in detail.

2.6 Conclusion

This chapter presents the virtual fields method for the direct identification of bending rigidities of thin anisotropic plates. Especially, it presents the adaptation of the newly proposed piecewise construction of the virtual fields over the specimen geometry.

The following chapter now introduces the noise effect on the identification procedure and presents an optimized identification procedure that is capable of direct and simultaneous identification of the unknown bending rigidities with least sensitivity to noise.

Chapter 3

Minimization of the effect of noisy data

3.1 Introduction

It is well established and known that actual experimental data are unavoidably noisy in practice. This noise must be accounted for during identification. Thus in the present study also, the curvature values of the plate under loading must necessarily contain noise. The minimization of the noise effect is used here to obtain the missing equations as discussed in Chapter 2 and the unknown vector $| Y^* >$ will be finally determined. The minimization is obtained using a method recently introduced, but in the case of virtual fields defined by the same function over the whole specimen and in the case of in-plane problems only [68]. It is adapted in the present work for the case of piecewise virtual fields and bending problems. In actual practice, deflectometry technique is used to measure the slope fields on the surface of specimen with the help of a CCD camera. Such slope fields represent noisy data on account of various noise sources originating from the light source used and from the camera used for the acquisition of images. Camera related noise sources are generally classified as external and intrinsic sources. External sources include for example, photon noise, electromagnetic noise originating from the power supply to the camera and the associated computer. However, intrinsic noise sources are related to the camera itself, some common sources are e.g., the CCD array used to capture the image, the different amplification stages and the built-in electronic circuits notably the analog to digital converters. In addition, there are some posterior noise sources arising from image treatment that is performed after the acquisition of images. Such noisy slopes fields are first fitted using a polynomial fitting before derivating to find a curvature field which is then used for identification of the unknown rigidities, refer to Section 8.3.4 for details. However the present numerical model makes use of a representative

standard Gaussian white noise added directly onto the curvature fields, purely for the reason of simplicity. In order to strictly verify the principle of virtual work using such noisy data the noise part must be eliminated and the theoretical Eq. (2.7) becomes

$$\begin{aligned} D_{xx}\int_S (k_x-\gamma N_x)\,k_x^* dA + D_{yy}\int_S (k_y-\gamma N_y)\,k_y^* dA \\ + D_{ss}\int_S (k_s-\gamma N_s)\,k_s^* dA + D_{xy}\int_S \left[(k_x-\gamma N_x)\,k_y^* + (k_y-\gamma N_y)\,k_x^*\right] dA \\ + D_{xs}\int_S \left[(k_x-\gamma N_x)\,k_s^* + (k_s-\gamma N_s)\,k_x^*\right] dA \\ + D_{ys}\int_S \left[(k_y-\gamma N_y)\,k_s^* + (k_s-\gamma N_s)\,k_y^*\right] dA = \sum_{i=1}^{n} F_i.w_i^* \end{aligned} \quad (3.1)$$

Here N_x, N_y and N_s are models of experimental noise. These are supposed to be standard Gaussian white noise (presumably having Standard Normal Distribution). γ is the standard deviation of noise. It is a positive real number and represents measurement uncertainty. Also, it is assumed that no statistical dependence exists between noise at two different measurement locations in addition to the noise components itself viz. N_x, N_y and N_s [68]. Upon rearranging the above expression and making use of the earlier substitution Eq. (2.9), we get

$$\begin{aligned} D_{xx}\left[I_{xx}-\gamma\int_S N_x k_x^* dA\right] + D_{yy}\left[I_{yy}-\gamma\int_S N_y k_y^* dA\right] + D_{ss}\left[I_{ss}-\gamma\int_S N_s k_s^* dA\right] \\ + D_{xy}\left[I_{xy}-\gamma\int_S \left(N_x k_y^* + N_y k_x^*\right) dA\right] + D_{xs}\left[I_{xs}-\gamma\int_S \left(N_x k_s^* + N_s k_x^*\right) dA\right] \\ + D_{ys}\left[I_{ys}-\gamma\int_S \left(N_y k_s^* + N_s k_y^*\right) dA\right] = \sum_{i=1}^{n} F_i.w^* \end{aligned} \quad (3.2)$$

According to Wiener processes theory, $N_x dA$, $N_y dA$, $N_s dA$, can here be replaced formally by dN_x, dN_y, dN_s in the integrals of Eq. (3.2) [68]. This substitution leads to

$$\begin{aligned} D_{xx}\left[I_{xx}-\gamma\int_S k_x^* dN_x\right] + D_{yy}\left[I_{yy}-\gamma\int_S k_y^* dN_y\right] + D_{ss}\left[I_{ss}-\gamma\int_S k_s^* dN_s\right] \\ + D_{xy}\left[I_{xy}-\gamma\int_S \left(k_y^* dN_x + k_x^* dN_y\right)\right] + D_{xs}\left[I_{xs}-\gamma\int_S \left(k_s^* dN_x + k_x^* dN_s\right)\right] \\ + D_{ys}\left[I_{ys}-\gamma\int_S \left(k_s^* dN_y + k_y^* dN_s\right)\right] = \sum_{i=1}^{n} F_i.w^* \end{aligned} \quad (3.3)$$

upon further contraction it may be written as

$$D_{xx}\left(I_{xx}-\gamma J_{xx}\right)+D_{yy}\left(I_{yy}-\gamma J_{yy}\right)+D_{ss}\left(I_{ss}-\gamma J_{ss}\right)+D_{xy}\left(I_{xy}-\gamma J_{xy}\right)$$
$$+D_{xs}\left(I_{xs}-\gamma J_{xs}\right)+D_{ys}\left(I_{ys}-\gamma J_{ys}\right)=\sum_{i=1}^{n}F_i.w_i^* \quad (3.4)$$

where

$$\left\{\begin{array}{lllll} J_{xx}=\int_S k_x^* dN_x & ; & J_{xy}=\int_S\left(k_y^* dN_x+k_x^* dN_y\right) \\ J_{yy}=\int_S k_y^* dN_y & ; & J_{xs}=\int_S\left(k_s^* dN_x+k_x^* dN_s\right) \\ J_{ss}=\int_S k_s^* dN_s & ; & J_{ys}=\int_S\left(k_s^* dN_y+k_y^* dN_s\right) \end{array}\right. \quad (3.5)$$

With the use of special virtual fields (see Eq. (2.11) a following system of six equations is obtained

$$\left\{\begin{array}{l} D_{xx}\left(1-\gamma J_{xx}^a\right)+D_{yy}\left(-\gamma J_{yy}^a\right)+D_{ss}\left(-\gamma J_{ss}^a\right)+D_{xy}\left(-\gamma J_{xy}^a\right) \\ \qquad +D_{xs}\left(-\gamma J_{xs}^a\right)+D_{ys}\left(-\gamma J_{ys}^a\right)=\sum_{i=1}^{n}F_i.w_i^{*a} \\ D_{xx}\left(-\gamma J_{xx}^b\right)+D_{yy}\left(1-\gamma J_{yy}^b\right)+D_{ss}\left(-\gamma J_{ss}^b\right)+D_{xy}\left(-\gamma J_{xy}^b\right) \\ \qquad +D_{xs}\left(-\gamma J_{xs}^b\right)+D_{ys}\left(-\gamma J_{ys}^b\right)=\sum_{i=1}^{n}F_i.w_i^{*b} \\ D_{xx}\left(-\gamma J_{xx}^c\right)+D_{yy}\left(-\gamma J_{yy}^c\right)+D_{ss}\left(1-\gamma J_{ss}^c\right)+D_{xy}\left(-\gamma J_{xy}^c\right) \\ \qquad +D_{xs}\left(-\gamma J_{xs}^c\right)+D_{ys}\left(-\gamma J_{ys}^c\right)=\sum_{i=1}^{n}F_i.w_i^{*c} \\ D_{xx}\left(-\gamma J_{xx}^d\right)+D_{yy}\left(-\gamma J_{yy}^d\right)+D_{ss}\left(-\gamma J_{ss}^d\right)+D_{xy}\left(1-\gamma J_{xy}^d\right) \\ \qquad +D_{xs}\left(-\gamma J_{xs}^d\right)+D_{ys}\left(-\gamma J_{ys}^d\right)=\sum_{i=1}^{n}F_i.w_i^{*d} \\ D_{xx}\left(-\gamma J_{xx}^e\right)+D_{yy}\left(-\gamma J_{yy}^e\right)+D_{ss}\left(-\gamma J_{ss}^e\right)+D_{xy}\left(-\gamma J_{xy}^e\right) \\ \qquad +D_{xs}\left(1-\gamma J_{xs}^e\right)+D_{ys}\left(-\gamma J_{ys}^e\right)=\sum_{i=1}^{n}F_i.w_i^{*e} \\ D_{xx}\left(-\gamma J_{xx}^f\right)+D_{yy}\left(-\gamma J_{yy}^f\right)+D_{ss}\left(-\gamma J_{ss}^f\right)+D_{xy}\left(-\gamma J_{xy}^f\right) \\ \qquad +D_{xs}\left(-\gamma J_{xs}^f\right)+D_{ys}\left(1-\gamma J_{ys}^f\right)=\sum_{i=1}^{n}F_i.w_i^{*f} \end{array}\right. \quad (3.6)$$

Now the rigidities are evaluated as

$$\begin{cases} D_{xx} = \sum_{i=1}^{n} F_i.w_i^{*a} + D_{xx}\gamma J_{xx}^a + D_{yy}\gamma J_{yy}^a + D_{ss}\gamma J_{ss}^a + D_{xy}\gamma J_{xy}^a \\ \qquad\qquad + D_{xs}\gamma J_{xs}^a + D_{ys}\gamma J_{ys}^a \\ D_{yy} = \sum_{i=1}^{n} F_i.w_i^{*b} + D_{xx}\gamma J_{xx}^b + D_{yy}\gamma J_{yy}^b + D_{ss}\gamma J_{ss}^b + D_{xy}\gamma J_{xy}^b \\ \qquad\qquad + D_{xs}\gamma J_{xs}^b + D_{ys}\gamma J_{ys}^b \\ D_{ss} = \sum_{i=1}^{n} F_i.w_i^{*c} + D_{xx}\gamma J_{xx}^c + D_{yy}\gamma J_{yy}^c + D_{ss}\gamma J_{ss}^c + D_{xy}\gamma J_{xy}^c \\ \qquad\qquad + D_{xs}\gamma J_{xs}^c + D_{ys}\gamma J_{ys}^c \\ D_{xy} = \sum_{i=1}^{n} F_i.w_i^{*d} + D_{xx}\gamma J_{xx}^d + D_{yy}\gamma J_{yy}^d + D_{ss}\gamma J_{ss}^d + D_{xy}\gamma J_{xy}^d \\ \qquad\qquad + D_{xs}\gamma J_{xs}^d + D_{ys}\gamma J_{ys}^d \\ D_{xs} = \sum_{i=1}^{n} F_i.w_i^{*e} + D_{xx}\gamma J_{xx}^e + D_{yy}\gamma J_{yy}^e + D_{ss}\gamma J_{ss}^e + D_{xy}\gamma J_{xy}^e \\ \qquad\qquad + D_{xs}\gamma J_{xs}^e + D_{ys}\gamma J_{ys}^e \\ D_{ys} = \sum_{i=1}^{n} F_i.w_i^{*f} + D_{xx}\gamma J_{xx}^f + D_{yy}\gamma J_{yy}^f + D_{ss}\gamma J_{ss}^f + D_{xy}\gamma J_{xy}^f \\ \qquad\qquad + D_{xs}\gamma J_{xs}^f + D_{ys}\gamma J_{ys}^f \end{cases} \tag{3.7}$$

The above implicit system of equations has in fact no closed-form expression. However assuming that γ is negligible in comparison to the minimum of the actual curvatures, approximate rigidity values are obtained. The assumption of negligible γ writes [68]

$$\gamma \ll Min(\| k_x \|, \| k_y \|, \| k_s \|) \tag{3.8}$$

The approximated value of the unknown rigidities can now be expressed as

$$
\begin{cases}
D_{xx} = \sum_{i=1}^{n} F_i.w_i^{*a} + D_{xx_{aprx}}\gamma J_{xx}^{a} + D_{yy_{aprx}}\gamma J_{yy}^{a} + D_{ss_{aprx}}\gamma J_{ss}^{a} + D_{xy_{aprx}}\gamma J_{xy}^{a} \\
\qquad\qquad + D_{xs_{aprx}}\gamma J_{xs}^{a} + D_{ys_{aprx}}\gamma J_{ys}^{a} \\
D_{yy} = \sum_{i=1}^{n} F_i.w_i^{*b} + D_{xx_{aprx}}\gamma J_{xx}^{b} + D_{yy_{aprx}}\gamma J_{yy}^{b} + D_{ss_{aprx}}\gamma J_{ss}^{b} + D_{xy_{aprx}}\gamma J_{xy}^{b} \\
\qquad\qquad + D_{xs_{aprx}}\gamma J_{xs}^{b} + D_{ys_{aprx}}\gamma J_{ys}^{b} \\
D_{ss} = \sum_{i=1}^{n} F_i.w_i^{*c} + D_{xx_{aprx}}\gamma J_{xx}^{c} + D_{yy_{aprx}}\gamma J_{yy}^{c} + D_{ss_{aprx}}\gamma J_{ss}^{c} + D_{xy_{aprx}}\gamma J_{xy}^{c} \\
\qquad\qquad + D_{xs_{aprx}}\gamma J_{xs}^{c} + D_{ys_{aprx}}\gamma J_{ys}^{c} \\
D_{xy} = \sum_{i=1}^{n} F_i.w_i^{*d} + D_{xx_{aprx}}\gamma J_{xx}^{d} + D_{yy_{aprx}}\gamma J_{yy}^{d} + D_{ss_{aprx}}\gamma J_{ss}^{d} + D_{xy_{aprx}}\gamma J_{xy}^{d} \\
\qquad\qquad + D_{xs_{aprx}}\gamma J_{xs}^{d} + D_{ys_{aprx}}\gamma J_{ys}^{d} \\
D_{xs} = \sum_{i=1}^{n} F_i.w_i^{*e} + D_{xx_{aprx}}\gamma J_{xx}^{e} + D_{yy_{aprx}}\gamma J_{yy}^{e} + D_{ss_{aprx}}\gamma J_{ss}^{e} + D_{xy_{aprx}}\gamma J_{xy}^{e} \\
\qquad\qquad + D_{xs_{aprx}}\gamma J_{xs}^{e} + D_{ys_{aprx}}\gamma J_{ys}^{e} \\
D_{ys} = \sum_{i=1}^{n} F_i.w_i^{*f} + D_{xx_{aprx}}\gamma J_{xx}^{f} + D_{yy_{aprx}}\gamma J_{yy}^{f} + D_{ss_{aprx}}\gamma J_{ss}^{f} + D_{xy_{aprx}}\gamma J_{xy}^{f} \\
\qquad\qquad + D_{xs_{aprx}}\gamma J_{xs}^{f} + D_{ys_{aprx}}\gamma J_{ys}^{f}
\end{cases}
\tag{3.9}
$$

From the above expression the error part may be separated as a matrix $[Err]$

$$
[Err] = \begin{bmatrix}
\gamma J_{xx}^{a} & \gamma J_{yy}^{a} & \gamma J_{ss}^{a} & \gamma J_{xy}^{a} & \gamma J_{xs}^{a} & \gamma J_{ys}^{a} \\
\gamma J_{xx}^{b} & \gamma J_{yy}^{b} & \gamma J_{ss}^{b} & \gamma J_{xy}^{b} & \gamma J_{xs}^{b} & \gamma J_{ys}^{b} \\
\gamma J_{xx}^{c} & \gamma J_{yy}^{c} & \gamma J_{ss}^{c} & \gamma J_{xy}^{c} & \gamma J_{xs}^{c} & \gamma J_{ys}^{c} \\
\gamma J_{xx}^{d} & \gamma J_{yy}^{d} & \gamma J_{ss}^{d} & \gamma J_{xy}^{d} & \gamma J_{xs}^{d} & \gamma J_{ys}^{d} \\
\gamma J_{xx}^{e} & \gamma J_{yy}^{e} & \gamma J_{ss}^{e} & \gamma J_{xy}^{e} & \gamma J_{xs}^{e} & \gamma J_{ys}^{e} \\
\gamma J_{xx}^{f} & \gamma J_{yy}^{f} & \gamma J_{ss}^{f} & \gamma J_{xy}^{f} & \gamma J_{xs}^{f} & \gamma J_{ys}^{f}
\end{bmatrix}
\tag{3.10}
$$

Now using Eq. (2.21), Eq. (3.9) is written as

$$\begin{bmatrix} D_{xx} \\ D_{yy} \\ D_{ss} \\ D_{xy} \\ D_{xs} \\ D_{ys} \end{bmatrix} = \begin{bmatrix} < R \mid\mid Y^{*a} > \\ < R \mid\mid Y^{*b} > \\ < R \mid\mid Y^{*c} > \\ < R \mid\mid Y^{*d} > \\ < R \mid\mid Y^{*e} > \\ < R \mid\mid Y^{*f} > \end{bmatrix} + [Err] \begin{bmatrix} < R \mid\mid Y^{*a}_{aprx} > \\ < R \mid\mid Y^{*b}_{aprx} > \\ < R \mid\mid Y^{*c}_{aprx} > \\ < R \mid\mid Y^{*d}_{aprx} > \\ < R \mid\mid Y^{*e}_{aprx} > \\ < R \mid\mid Y^{*f}_{aprx} > \end{bmatrix} \tag{3.11}$$

Here, $(Y^{*\alpha})$ and $(Y^{*\alpha}_{aprx})$ with $\alpha = a, b, c, d, e, f$, verify the special virtual field conditions. However, it must be noted that the above system of equations is not explicit as it makes use of initially approximate rigidity values. Its solution is discussed in Section 3.2 below.

Now the respective variances (V) of the rigidities are derived using Eq. (3.9). Recalling that the injected noise represents white noise, it implies that its mean or Expected Value (E) is zero. Hence, mean of the rigidities $E(D_{xx})$, $E(D_{yy})$, $E(D_{ss})$, $E(D_{xy})$,$E(D_{xs})$ and $E(D_{ys})$ are in fact the exact values (using Eq. (2.21)) identified without noise. Thus, for $V(D_{xx})$ it writes

$$\begin{aligned} V(D_{xx}) &= E\left[\{D_{xx} - E\left(D_{xx}\right)\}^2\right] \\ &= E\Bigg[\Bigg\{ < R \mid\mid Y^{*a} > + \gamma < R \mid\mid Y^{*a}_{aprx} > J^a_{xx} + \gamma < R \mid\mid Y^{*b}_{aprx} > J^a_{yy} \\ &\quad + \gamma < R \mid\mid Y^{*c}_{aprx} > J^a_{ss} + \gamma < R \mid\mid Y^{*d}_{aprx} > J^a_{xy} + \gamma < R \mid\mid Y^{*e}_{aprx} > J^a_{xs} \\ &\quad + \gamma < R \mid\mid Y^{*f}_{aprx} > J^a_{ys} - < R \mid\mid Y^{*a} > \Bigg\}^2\Bigg] \\ &= \gamma^2 E\Bigg[\Bigg\{ < R \mid\mid Y^{*a}_{aprx} > J^a_{xx} + < R \mid\mid Y^{*b}_{aprx} > J^a_{yy} + < R \mid\mid Y^{*c}_{aprx} > J^a_{ss} \\ &\quad + < R \mid\mid Y^{*d}_{aprx} > J^a_{xy} + < R \mid\mid Y^{*e}_{aprx} > J^a_{xs} + < R \mid\mid Y^{*f}_{aprx} > J^a_{ys} \Bigg\}^2\Bigg] \end{aligned} \tag{3.12}$$

similarly the other variances are written as

$$\begin{cases} V(D_{xx}) = & E[(D_{xx} - E(D_{xx}))^2] & = & \gamma^2 < D_{aprx} \mid E(\mid N^a >< N^a \mid) \mid D_{aprx} > \\ V(D_{yy}) = & E[(D_{yy} - E(D_{yy}))^2] & = & \gamma^2 < D_{aprx} \mid E(\mid N^b >< N^b \mid) \mid D_{aprx} > \\ V(D_{ss}) = & E[(D_{ss} - E(D_{ss}))^2] & = & \gamma^2 < D_{aprx} \mid E(\mid N^c >< N^c \mid) \mid D_{aprx} > \\ V(D_{xy}) = & E[(D_{xy} - E(D_{xy}))^2] & = & \gamma^2 < D_{aprx} \mid E(\mid N^d >< N^d \mid) \mid D_{aprx} > \\ V(D_{xs}) = & E[(D_{xs} - E(D_{xs}))^2] & = & \gamma^2 < D_{aprx} \mid E(\mid N^e >< N^e \mid) \mid D_{aprx} > \\ V(D_{ys}) = & E[(D_{ys} - E(D_{ys}))^2] & = & \gamma^2 < D_{aprx} \mid E(\mid N^f >< N^f \mid) \mid D_{aprx} > \end{cases} \tag{3.13}$$

or in general

$$V(D_{ij}) = \; E[(D_{ij} - E(D_{ij}))^2] \;\; = \;\; \gamma^2 < D_{aprx} \mid E(\mid N^{\alpha} >< N^{\alpha} \mid) \mid D_{aprx} > \tag{3.14}$$

with

$$\begin{aligned} ij &= xx, yy, ss, xy, xs, ys \\ \alpha &= a, b, c, d, e, f \\ < N^{\alpha} \mid &= [J^*_{xx}, J^*_{yy}, J^*_{ss}, J^*_{xy}, J^*_{xs}, J^*_{ys}] \\ < D_{approx} \mid &= (D^a_{aprx}, D^b_{aprx}, D^c_{aprx}, D^d_{aprx}, D^e_{aprx}, D^f_{aprx}) \\ &= (< R \mid\mid Y^{*a}_{aprx}, < R \mid\mid Y^{*b}_{aprx}, < R \mid\mid Y^{*c}_{aprx}, < R \mid\mid Y^{*d}_{aprx}, < R \mid\mid Y^{*e}_{aprx}, < R \mid\mid Y^{*f}_{aprx}) \end{aligned}$$

From above it is concluded that the variance of unknown rigidities is proportional to γ^2 and $(\eta^{\alpha})^2$ is a proportionality constant as shown in ref. [68]. This implies that the standard deviation (defined by the square root of V: $Std = \sqrt{V}$) of the rigidities is related to the standard deviation of input noise as follows

$$\begin{cases} Std\,(D_{xx}) &= (\eta^a)\gamma \\ Std\,(D_{yy}) &= (\eta^b)\gamma \\ Std\,(D_{ss}) &= (\eta^c)\gamma \\ Std\,(D_{xy}) &= (\eta^d)\gamma \\ Std\,(D_{xs}) &= (\eta^e)\gamma \\ Std\,(D_{ys}) &= (\eta^f)\gamma \end{cases} \tag{3.15}$$

Thus it is shown that the uncertainty of identification procedure is proportional to the uncertainty of the measurement method. Let η^{α} be defined as *sensitivity* of the VFM to a given random noise, then, the lower the value of η^{α} the more accurate is the identification. η^{α} may be expressed as

$$
\begin{aligned}
(\eta^{\alpha})^2 = \frac{S}{n_e}\Big[& \left[(D_{xx})^2 + (D_{xy})^2 + (D_{xs})^2\right] \int_S (k_x^{*\alpha})^2 dA \\
& + \left[(D_{yy})^2 + (D_{xy})^2 + (D_{ys})^2\right] \int_S (k_y^{*\alpha})^2 dA \\
& + \left[(D_{ss})^2 + (D_{xs})^2 + (D_{ys})^2\right] \int_S (k_s^{*\alpha})^2 dA \\
& + 2\,(D_{xx} + D_{yy})\, D_{xy} \int_S (k_x^{*\alpha} k_y^{*\alpha}) dA \\
& + 2\,(D_{xx} + D_{ss} + D_{xy})\, D_{xs} \int_S (k_x^{*\alpha} k_s^{*\alpha}) dA \\
& + 2\,(D_{yy} + D_{ss} + D_{xy})\, D_{ys} \int_S (k_y^{*\alpha} k_s^{*\alpha}) dA \Big]
\end{aligned}
\tag{3.16}
$$

Now making use of the discrete nature of curvature fields, the integrals here can be evaluated by using rectangular method for the numerical integration, as described earlier in Section 2.2.4. For this purpose a total number of n_e different data points are defined over the specimen surface whose coordinates are represented by x_g and y_g. Now the above equation becomes

$$
\begin{aligned}
(\eta^{\alpha})^2 = \left(\frac{S}{n_e}\right)^2 \sum_{i=1}^{n_e} \Big\{ & \left[(D_{xx})^2 + (D_{xy})^2 + (D_{xs})^2\right] \left[k_x^{*\alpha}(x_g, y_g)_i\right]^2 \\
& + \left[(D_{yy})^2 + (D_{xy})^2 + (D_{ys})^2\right] \left[k_y^{*\alpha}(x_g, y_g)_i\right]^2 \\
& + \left[(D_{ss})^2 + (D_{xs})^2 + (D_{ys})^2\right] \left[k_s^{*\alpha}(x_g, y_g)_i\right]^2 \\
& + 2\,(D_{xx} + D_{yy})\, D_{xy}\; k_x^{*\alpha}(x_g, y_g)_i\; k_y^{*\alpha}(x_g, y_g)_i \\
& + 2\,(D_{xx} + D_{ss} + D_{xy})\, D_{xs}\; k_x^{*\alpha}(x_g, y_g)_i\; k_s^{*\alpha}(x_g, y_g)_i \\
& + 2\,(D_{yy} + D_{ss} + D_{xy})\, D_{ys}\; k_y^{*\alpha}(x_g, y_g)_i\; k_s^{*\alpha}(x_g, y_g)_i \Big\}
\end{aligned}
\tag{3.17}
$$

In the above Eq. (3.17) one of the $\frac{S}{n_e}$ comes from Eq. (3.16) whereas the other one is due to the use of rectangular method for numerical approximation. The additional $\frac{S}{n_e}$ depends on the type of method used for numerical integration. For instance, it is not required in the case of numerical integration performed by the Gauss-Legendre method as it is already taken into account in its formulation.

Here it is important to note that the absolute value of η^{α} may not be as representative as the relative error induced in the identified rigidities due to noisy data. For example, a greater absolute value of η^{a} can be of less significance (in fact misleading) to a lesser absolute value of η^{b} if D_{xx} is much greater than D_{yy}. So, the criteria to be followed should rather be η^{a}/D_{xx} , η^{b}/D_{yy} , η^{c}/D_{ss} , η^{d}/D_{xy} , η^{e}/D_{xs} and η^{f}/D_{ys} called here noise sensitivity indices or simply *sensitivity indices*, (ratio

between sensitivity of the VFM for a given noisy data to the mean of identified rigidity).

3.2 Optimized virtual field: Minimization of noise effect

Finding an optimized virtual field means finding the vector of virtual dofs $\mid Y^* >$ that fits to the criteria of kinematically admissible special virtual fields (see Sections 2.3 and 2.4) and at the same time minimizes η^α (the effect of noisy data). Hence leading to the most accurate identification of the unknown rigidities for a given number of virtual elements. Here the benefit of using greater number of virtual elements is worth noting. Larger is the space of K.A virtual fields, greater is the opportunity of finding a unique virtual field least sensitive to noise. For this problem of minimization it can be proved that the objective function is [68]

$$(\eta^\alpha)^2 = 1/2 \ < Y^{*\alpha}\mid H \mid Y^{*\alpha} > \tag{3.18}$$

The above expression of $(\eta^\alpha)^2$ is in fact a condensed form of earlier expression given in Eq. (3.17). Here, H is a semi-definite positive symmetric matrix calculated numerically using the vectorial functions $< b_x(x,y) \mid$, $< b_y(x,y) \mid$and $< b_s(x,y) \mid$. These are second derivatives of shape functions as shown earlier in Eq. (2.16). Matrix H can be written as

$$\begin{aligned} H = 2\Big(\frac{S}{n_e}\Big)^2 \sum_{i=1}^{n_e} \Big\{ & \left[(D_{xx})^2 + (D_{xy})^2 + (D_{xs})^2\right] (\mid b_x(x_g,y_g)_i >< b_x(x_g,y_g)_i \mid) \\ & + \left[(D_{yy})^2 + (D_{xy})^2 + (D_{ys})^2\right] (\mid b_y(x_g,y_g)_i >< b_y(x_g,y_g)_i \mid) \\ & + \left[(D_{ss})^2 + (D_{xs})^2 + (D_{ys})^2\right] (\mid b_s(x_g,y_g)_i >< b_s(x_g,y_g)_i \mid) \\ & + 2\,(D_{xx} + D_{yy})\,D_{xy}\,(\mid b_x(x_g,y_g)_i >< b_y(x_g,y_g)_i \mid) \\ & + 2\,(D_{xx} + D_{ss} + D_{xy})\,D_{xs}\,(\mid b_x(x_g,y_g)_i >< b_s(x_g,y_g)_i \mid) \\ & + 2\,(D_{yy} + D_{ss} + D_{xy})\,D_{ys}\,(\mid b_y(x_g,y_g)_i >< b_s(x_g,y_g)_i \mid) \Big\} \end{aligned} \tag{3.19}$$

It is recalled here that six different objective functions $(\eta^\alpha)^2, \alpha = a,b,c,d,e,f$ must be used to determine each of the six unknowns D_{xx}, D_{yy}, D_{ss}, D_{xy}, D_{xs} and D_{ys} respectively. The above problem is a minimization under constraints, as virtual deformation field, $\mid Y^* >$, must satisfy the following two equality constraints

- it should be zero at the support points as per Eq. (2.19) (see Section 2.3).

- as the virtual field is special, $\mid Y^* >$ must satisfy Eq. (2.20) respectively for each of the six unknown rigidities (see Section 2.4).

Thus, $\mid Y^* >$ is stationary point of the Lagrangian $\mathcal{L}^\alpha$

$$\mathcal{L}^\alpha = 1/2 \ < Y^{*\alpha}| \ H \ | \ Y^{*\alpha} > + < \Lambda^\alpha| \ A \ | \ Y^{*\alpha} > - < \Lambda^\alpha| \ | \ Z^\alpha > \tag{3.20}$$

where

- $< \Lambda^\alpha|$ is the vector comprising of Lagrangian multiplicators,
- A is the matrix of equality constraint equations, refer to Sections 2.3 and 2.4 ,
- $\mid Z^\alpha >$ reads:

$$\begin{cases} < Z^a| = & (0\ 0\ 0\ \ldots .\ 0\ \ 1\ 0\ 0\ 0\ 0\ 0) \\ < Z^b| = & (0\ 0\ 0\ \ldots .\ 0\ \ 0\ 1\ 0\ 0\ 0\ 0) \\ < Z^c| = & (0\ 0\ 0\ \ldots .\ 0\ \ 0\ 0\ 1\ 0\ 0\ 0) \\ < Z^d| = & (0\ 0\ 0\ \ldots .\ 0\ \ 0\ 0\ 0\ 1\ 0\ 0) \\ < Z^e| = & (0\ 0\ 0\ \ldots .\ 0\ \ 0\ 0\ 0\ 0\ 1\ 0) \\ < Z^f| = & (0\ 0\ 0\ \ldots .\ 0\ \ 0\ 0\ 0\ 0\ 0\ 1) \end{cases}$$

Now, for the Lagrangian $\mathcal{L}^\alpha$ which depends on both $\mid Y^* >$ and $< \Lambda^\alpha|$, finding the stationary value is equivalent to finding its saddle point. As proved in ref. [68] a unique saddle point exists because $(\eta^\alpha)^2$ is a continuous convex quadratic function in the space of virtual fields. Thus, $\mid Y^{*\alpha} >$ can be found by solving the six linear system

$$\begin{bmatrix} H & A^T \\ A & 0 \end{bmatrix} \begin{bmatrix} |Y^\alpha > \\ |\Lambda^\alpha > \end{bmatrix} = \begin{bmatrix} 0 \\ 0 \\ \vdots \\ 0 \\ |Z^\alpha > \end{bmatrix} \tag{3.21}$$

Remembering the fact that the expression of H in Eq. (3.18) derived from Eq. (3.12) already depends upon the unknown rigidities (see Eq. (3.11)), the problem becomes implicit and a solution cannot be directly obtained by solving the above linear system. Therefore an iterative algorithm given below is adopted for the purpose

- *iteration 0.*
  A random value (between 0 and 1) is assigned to each of the unknown rigidities D_{xx}, D_{yy}, D_{ss}, D_{xy}, D_{xs} and D_{ys} to provide initial values in H and first set of unknown rigidities are calculated by solving the linear system.

- *iteration 1.*
  Now the above calculated rigidity values are again used in expression of H to find updated rigidity values.

- *iteration n.*
  The procedure is repeated till the relative difference of the identified values calculated at two consecutive iterations is less than 0.1%. Numerically it has been checked through various preliminary simulations that the convergence criteria is attained quite rapidly at the most up to 3rd or 4th iterations.

3.3 Conclusion

This chapter studied the noise effect onto the identification procedure based on the piecewise virtual fields method for a case of thin plate bending problem as discussed in Chapter 2. It is shown here that the minimization of noise effect results in the automatic construction of a unique virtual field in a given basis of functions. This unique virtual field on the one hand satisfies the condition of special virtual field and on the other hand is least sensitive to noise. Finally, an optimized identification procedure with minimum noise sensitivity is presented and adapted here for simultaneous identification of the unknown bending rigidities of a thin anisotropic plate.

The following chapter now presents a numerical validation of the optimized identification procedure with simulated composite plate bending problems.

Chapter 4

Numerical simulations

4.1 Introduction

The optimized identification procedure developed in the present work is validated with some numerical examples. For this purpose unidirectional orthotropic glass-epoxy composite plates $[0_4]_s$ with dimensions $L = W = 0.1m$ and $1mm$ thickness are simulated. Typical elastic constant values of glass-epoxy unidirectional composite material, $E_x = 40\ GPa$, $E_y = 10\ GPa$, $\nu_{xy} = 0.3$ and $G_{xy} = 4\ GPa$ are used as input of a FE model which provides simulated curvatures. A case of completely anisotropic plate is also briefly presented in Section 4.4.4.

The identification procedure is programmed as a Matlab 6.5 routine while ANSYS 9.0 is used to obtain simulated curvature components on the specimen top surface. A plane stress condition is assumed as the specimen is sufficiently thin. The plate finite element model (FEM) is meshed in 48×48=2304 square elements of type Shell 99. The element is defined by eight nodes and has six degrees of freedom at each node: translations in the nodal x, y, and z directions and rotations about the nodal x, y, and z-axes (Theory Reference, ANSYS, Inc). Worth noting that the elements formed in the FEM will be referred to as *real elements* to differentiate with virtual elements that define the virtual fields. The three curvatures at the center of real elements obtained from the FE model are considered as input data of the identification program.

For validation purposes, three different testing configurations plotted in Fig 4.1 are studied. All the plates have same dimensions, stacking sequence and material properties. In addition, Config-3 is also identical to the example used in ref. [3] and will be used for comparison purposes. In this reference, the virtual fields were constructed with a polynomial (of 16 unknowns) defined over the whole plate geometry and the minimization of noise effect was carried out using a semi-empirical approach (see also ref. [77]). For validation of the optimized identification procedure

and also for comparison to earlier work, simulated results for Config-3 are presented and discussed in detail here.

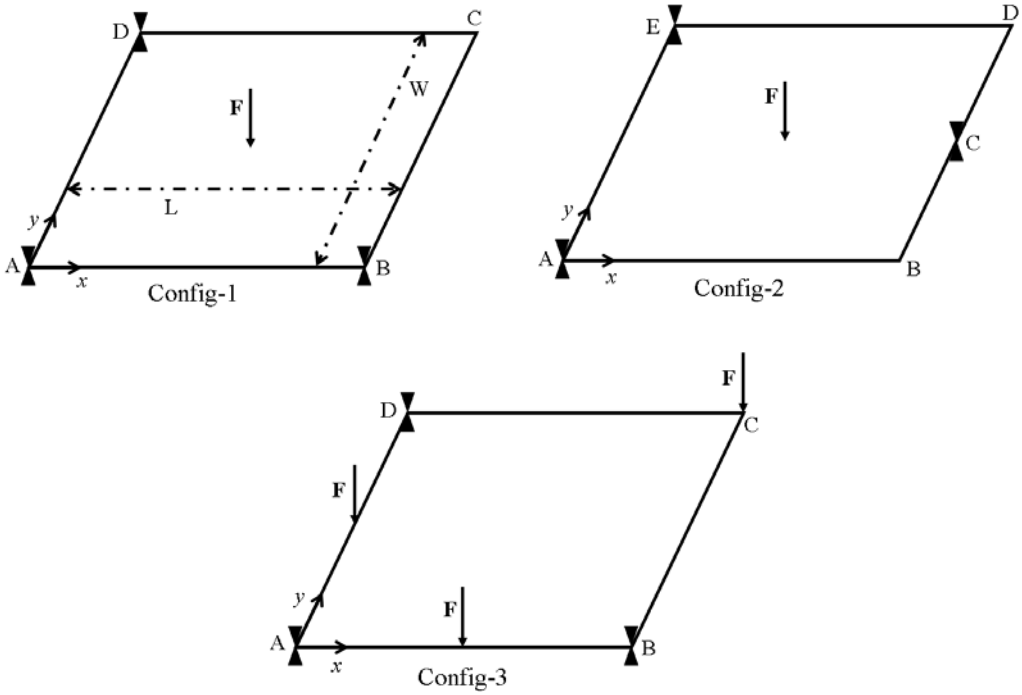

Figure 4.1: The three testing configurations with $L = W = 100mm$ and $\mathbf{F} = 100N$

The major objectives of the following sections are:

- to study the influence of virtual mesh density, in order to determine the maximum optimum number of virtual elements to be used for better identification and least sensitive to noisy data.
- to validate and support the fact that better identification is achieved when piecewise virtual fields are used in comparison of polynomials used in some earlier studies [3].

4.2 Results without noise

The present section discusses the effect of using an increasing number of virtual elements on the identification. The idea is to determine the optimal number of virtual elements to be used. The noise sensitivity index is used as a criterion. After convergence verification, a mesh density of 48×48=2304 real elements was used in the FE model to provide the simulated curvatures to be processed, but a mesh of only few virtual elements is used to limit the number of virtual degrees of freedom.

Here, it must be noted that the boundary of real and virtual elements must coincide with each other as shown in Fig 4.2 to avoid computational complexities.

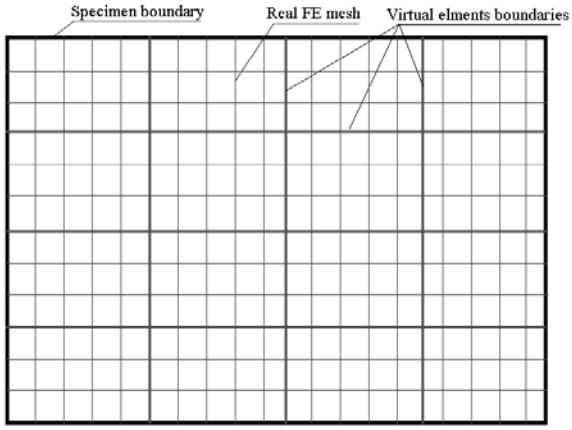

Figure 4.2: An illustration of a properly superimposed 4×4 virtual elements mesh over a real FE mesh.

Also, it is worth noting that a typical example with 4×4 virtual elements requires around 3 minutes of computation time. However, a higher number of virtual elements e.g. 20×20 and beyond should be avoided for memory problems during Matlab processing and also on account of lengthy computing time (approx 40 minutes).

4.3 Influence of the virtual elements mesh density

Table 4.1 presents the results for increasing numbers of virtual elements with respective noise sensitivity index values for Config-3.

Virtual elements	η^a/D_{xx} $(\times 10^{-3})$	η^b/D_{yy} $(\times 10^{-3})$	η^c/D_{ss} $(\times 10^{-3})$	η^d/D_{xy} $(\times 10^{-3})$
$1 \times 1 = 1$	3.8	2.7	0.2	13.8
$2 \times 2 = 4$	3.1	1.9	0.2	11.0
$4 \times 4 = 16$	3.0	1.9	0.2	10.6
$6 \times 6 = 36$	3.0	1.9	0.2	10.6
$8 \times 8 = 64$	3.0	1.9	0.2	10.5

Table 4.1: Config-3, Choice of optimum number of virtual elements.

As may be seen, the noise sensitivity indices first decrease and then remain approximately constant from $4 \times 4 = 16$ virtual elements onwards. Also, from the above table and by comparing the relative magnitudes of sensitivity index for each of the rigidity, it is evident that D_{xy} is most sensitive to noise thus most difficult to

identify with greater accuracy followed by D_{xx}, D_{yy} and D_{ss} respectively. In Fig 4.3 to Fig 4.6 below, respective special virtual deflection fields for Config-3 are presented separately for each of the rigidities with increasing numbers of virtual elements. It may be noted that from $4 \times 4 = 16$ virtual elements onwards no significant change in the shape of virtual deflection fields is observed. The perfect continuity of the deflection at the boundary of the virtual elements is observed.

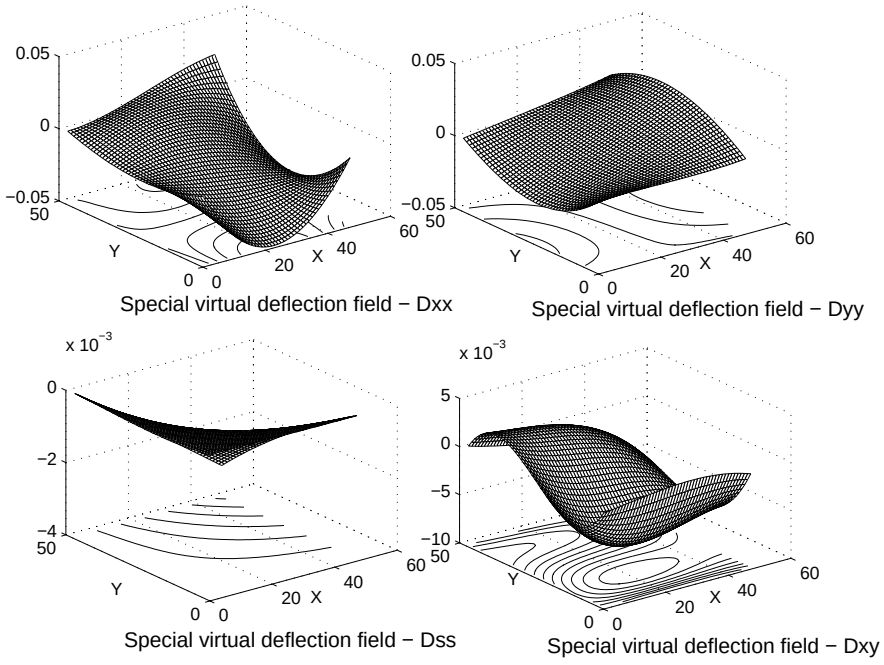

Figure 4.3: Config-3, Special virtual deflection fields using 1 virtual element.

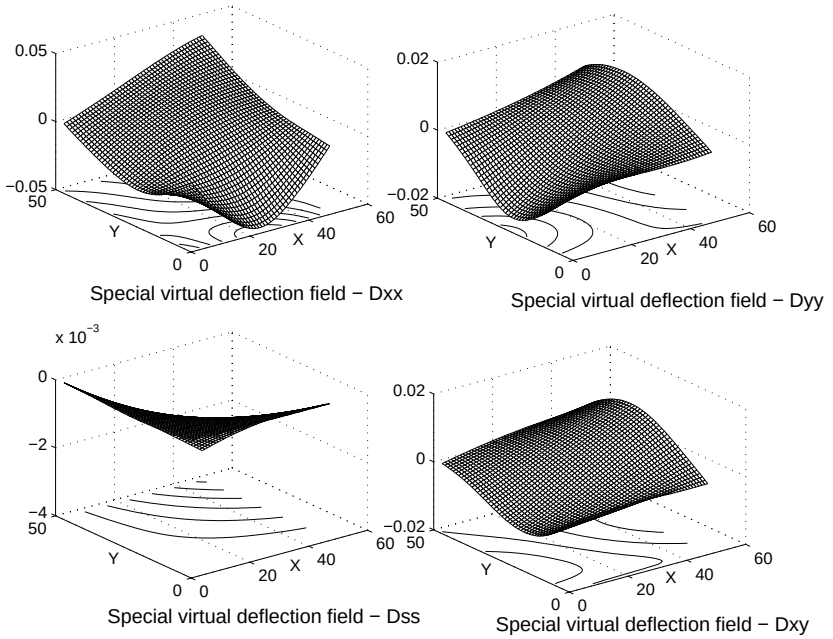

Figure 4.4: Config-3, Special virtual deflection fields using $4 \times 4 = 16$ virtual elements.

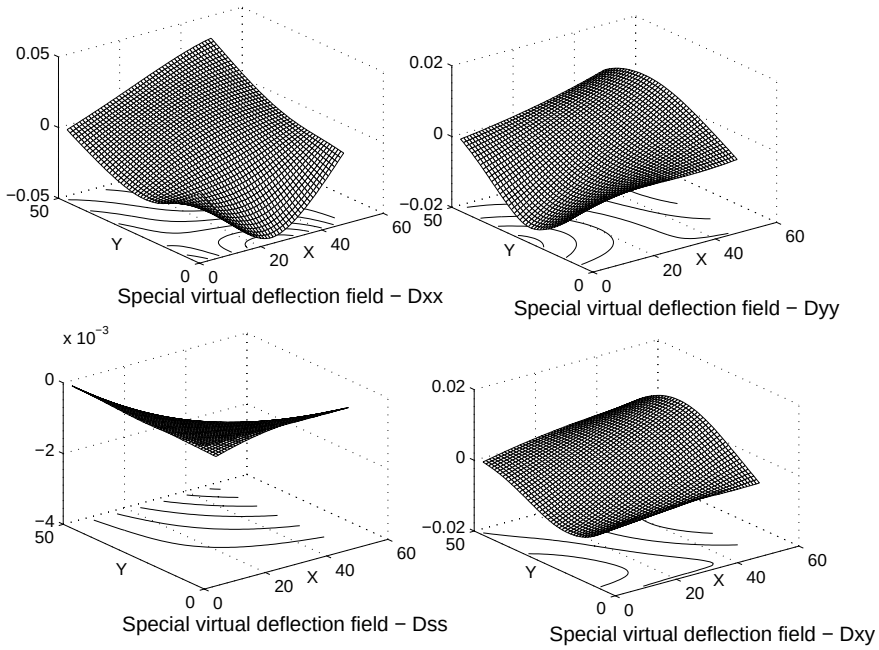

Figure 4.5: Config-3, Special virtual deflection fields using $6 \times 6 = 36$ virtual elements.

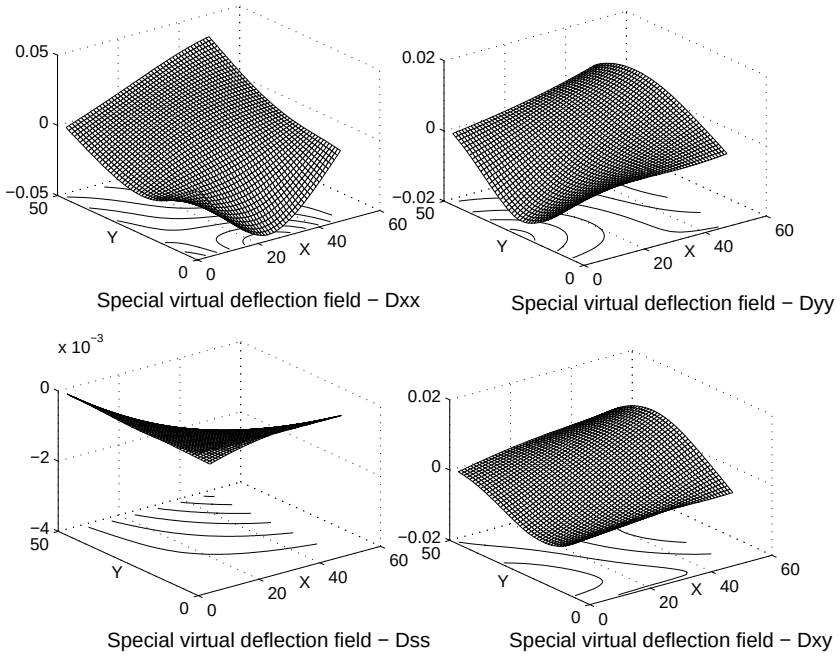

Figure 4.6: Config-3, Special virtual deflection fields using $8 \times 8 = 64$ virtual elements.

From above discussion and results for Config-3, it may be concluded that the use of $4 \times 4 = 16$ virtual elements is optimal in terms of result accuracy and lesser sensitivity to noise. It must be pointed out here that the same conclusion was achieved for the other two configurations, however the corresponding results are not reported here.

4.4 Influence of noisy data

4.4.1 Introduction

It is of prime importance to examine the stability of the procedure with respect to noise since virtual fields are here expected to minimize this effect. To simulate the noise effect, a Standard Gaussian white noise multiplied by a positive number γ is added to each of the curvature values. The maximum magnitude of γ is a predefined percentage (in the present study often taken as 5%) of the maximum of the absolute values of the three curvatures. It should be noted that in case of unbalanced values of the three curvatures k_x, k_y and k_s, this value of 5% leads in fact to significant changes and disturbances in the lowest curvature fields. This noise amplitude γ is regularly distributed in 20 intervals. The first value $\gamma = 0$ corresponds to the identification without noise and serves as reference theoretical values given by Eq.

(2.12) and Eq. (3.13). At each of the successive 20 values of γ, identification is made 50 times by changing the added white noise each time. Finally mean of the identified rigidities and standard deviations of the respective rigidities are calculated from the results of 50 iterations at each of the 20 noise levels for a given number of virtual elements.

4.4.2 Consistency of the results

For Config-3, Fig 4.7 represents standard deviations for the identified rigidities are plotted against γ for 16 virtual elements. Slope of the straight line represents theoretical sensitivity values η^{α} obtained from Eqs. (3.15) and (3.18) and it is expected to find from simulations similar results as those provided by Eq. (3.18).

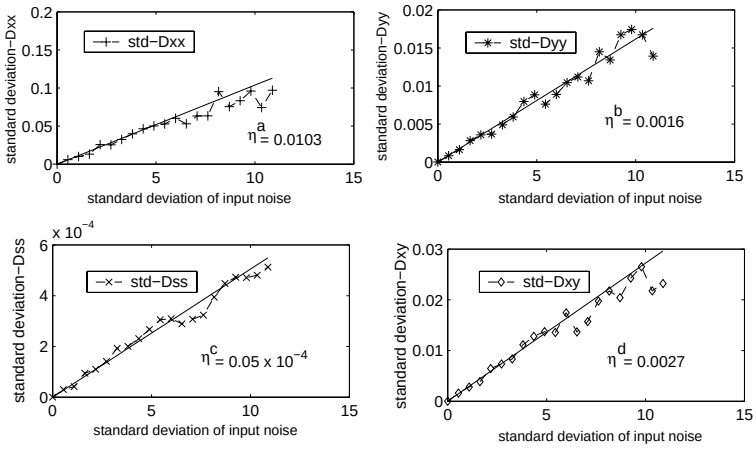

Figure 4.7: Config-3: Standard deviations of rigidities identified at increasing noise levels (γ), using $4 \times 4 = 16$ virtual elements

From above figure, it may be concluded that standard deviations of the identified rigidities are linear functions of γ and that these standard deviation values are in very good agreement with the straight line plotted using Eq. (3.18). This shows that the results obtained with simulated noisy data are consistent with theoretical expectations.

4.4.3 Comparison with some earlier results

In ref. [3], identification was achieved using the VFM with special virtual fields. However for virtual fields construction, a polynomial of 16 unknowns defined over the whole geometry of plate was used, and noise minimization was roughly performed using a semi-empirical rule (see also ref. [77]). In this section a comparison is made using the results from optimized identification approach presented above. First,

using only one virtual element defined over the specimen geometry, identification is achieved. It serves to compare this optimized method with noise minimization effect to that of ref. [3]. Use of single virtual element leads to sixteen unknowns to completely define the field (refer to Section 2.2.2) which is the same number as in the case of ref. [3], hence the two are directly comparable. In addition, results using $4 \times 4 = 16$ virtual elements are also presented which are supposed to be more robust and leading to better identification as established above. The results are presented in Table 4.2.

Procedure		D_{xx} (N m)	D_{yy} (N m)	D_{ss} (N m)	D_{xy} (N m)
	Ref Val.	3.41	0.85	0.33	0.25
ref. [3]	% var. coef	5.19	7.08	0.26	17.70
1 virtual element	% var. coef	4.50	2.62	0.18	17.36
$4 \times 4 =$ 16 virtual elements	% var. coef	3.08	1.81	0.16	8.49

Table 4.2: Config-3, comparison with earlier results [3]

From above it is seen that the present approach is better in comparison to that of ref. [3] in terms of reduced *variation coefficients* (defined by the ratio between standard deviation of the distribution and the respective average rigidity) and that the use of optimum number of virtual elements renders even lesser variation coefficient values, as expected.

4.4.4 Influence of plate anisotropy

This section illustrates the identification in case of complete anisotropy. For this purpose, using Config-3, only the stacking sequence is modified to $[0 \pm 30\ 90]_s$. Such a stacking sequence leads to an anisotropic plate in case of bending. Identification results using 16 virtual elements are presented below in Table 4.3. Results, (Percentage relative error (*rel. err(%)*) and percentage variation coefficients (*var.coef(%)*)), are recorded both for the case of noiseless data and when a random white noise (γ= 5% of the maximum of the three curvature values) is added.

Virtual elements	Ref Val. (in Nm)	D_{xx} 2.92	D_{yy} 0.97	D_{ss} 0.52	D_{xy} 0.44	D_{xs} 0.33	D_{ys} 0.12
$4 \times 4 = 16$	no noise	2.91	0.97	0.52	0.43	0.33	0.12
	rel. err(%)	*-0.42*	*-1.13*	*0.13*	*-1.14*	*-0.45*	*0.58*
	5% noise	2.81	0.95	0.51	0.40	0.31	0.11
	rel. err(%)	*-4.00*	*-1.39*	*-0.44*	*-9.68*	*-5.68*	*-4.61*
	var.coef(%)	*2.19*	*1.82*	*0.43*	*6.44*	*3.16*	*5.14*

Table 4.3: Config-3, Identification results for anisotropic plate

Table 4.3 shows the ability of the procedure to extract all the six unknown rigidities from a single test with a good accuracy. It is worth noting that the sensitivity to noise of the different identified rigidities changes from one rigidity to another. This result is directly related to the actual curvature fields which are processed and therefore to the location of the loading and support points. It is therefore a relevant issue to try to find an optimal testing configuration which minimizes either one of the sensitivities or the difference between the different sensitivities. The following chapter now discusses grading of the three testing configurations, presented in Fig 4.1, on the basis of better identifiability with minimum noise sensitivity.

4.5 Conclusion

This chapter presents a numerical validation of the piecewise virtual fields method developed in the present work. Use of the optimum number of piecewise virtual elements to define the virtual fields over a specimen is also discussed in detail. With the help of a numerically simulated example of an thin orthotropic glass-epoxy composite plate, the identification procedure is applied to extract the unknown bending rigidities. The influence of noisy data is also studied on the robustness and accuracy

of the identification results. It also compares the improvement in terms of identifiability and noise sensitivity in case of the piecewise virtual fields construction to an earlier work where the virtual fields were constructed by using polynomial functions defined over the whole specimen. In the end, an example of complete anisotropic plate is also presented to demonstrate the ability of the developed method to simultaneously identify all the six bending rigidities.

The following chapter now discusses the use of the developed piecewise virtual fields method as a tool to grade different testing configurations on account of better identifiability and reduced sensitivity to noise.

Chapter 5

Rating and classification of testing configuration

5.1 Introduction

This chapter presents the ability of the present approach to be used as a tool for grading of different testing configurations with reference to better identifiability. A testing configuration which involves all the parameters in a balanced and homogenized manner will lead to a more efficient global identification. Also, effect of load application point is discussed here in order to optimize a given testing configuration in such a way that this configuration leads to better identification with least sensitiveness to noise. For these purposes, sensitivity indices, η^{α}/D_{α} or combination of these are used as minimization criterion. However, it is important to note here that this minimization criterion should first be normalized in order to compare two different situations. The following section now discusses the normalization of the criterion used.

5.2 Normalization of minimization criterion

For comparison purposes of different configurations, a normalized noise minimization criterion is introduced here. Let δ^{α} given by Eq. (5.1) represent the normalized minimization criterion based on the sensitivity indices, it has a unit m^{-1}. It is normalized with respect to the variable parameters, maximum deflection w_{max}, total number of data points n_e and surface area S.

$$\delta^{\alpha} = \eta^{\alpha}/D_{\alpha} \times w_{max} \times \sqrt{n_e} \times (1/S) \tag{5.1}$$

This normalization results in an intrinsic criterion value with respect to the noted

parameters, thus the two different situations in terms of these parameters become directly comparable. The different normalization factors are justified below.

- Normalization with respect to maximum deflection, w_{max}. From the condition of a special virtual field recalled from Eq. (2.11)

$$\int_S k_x k_x^* dA = 1$$

it may be observed that the virtual curvatures are inversely proportional to the applied loading since k_x is proportional to the applied loading. For better understanding, a situation may be considered where the applied load is increased by a factor β, consequently the real curvatures will be increased by the same factor β.

$$F \rightarrow \beta F \; and \;\; k_x \rightarrow \beta k_x$$

However the above equality condition dictates the fact that the virtual curvatures become inversely proportional to the same factor β such that

$$k_x^* \rightarrow \frac{1}{\beta} k_x^*$$

The same is also true for any other quantity which is directly proportional to the applied load, e.g. maximum deflection, w_{max}, which is considered in the present study. Similarly, it may be said that the sensitivity to noise (η^α) is inversely proportional to the applied load or to the resulting w_{max}, as can be verified in Eq. (3.16). Thus for normalization, i.e. to make the sensitivity index independent of the force magnitude, it is multiplied by w_{max}. By this, an unbiased representative comparison is possible when force location or magnitude changes for a given testing configuration or when different testing configurations are studied.

- Normalization with respect to n_e. Now the normalization with respect to the total number of n_e different data points defined over the specimen surface is discussed. From Eq. (3.16) it is shown that for a given specimen geometry $(\eta^\alpha)^2$ values are inversely proportional to n_e. Thus in order to normalize with respect to different number of data points used from one case to another, the selection criterion should be multiplied by $\sqrt{n_e}$. By this, for a same plate, two different results using different number of data points will give same criterion values.

- Normalization with respect to plate surface area, S. Also, from Eq. (3.16), it may be observed that $(\eta^\alpha)^2$ is directly proportional to S^2. In fact, one of the S is present as a multiplicative factor in Eq. (3.16), while the other S comes from

the surface integration performed over the surface S. Thus for an independent comparison with respect to the plate size, criterion value should be divided by S.

Finally with the help of numerical examples, the effect of using normalized criterion values is presented. For this purpose, Table 5.1 records the normalized individual (δ^{α}) criteria values for two different cases in terms of variable force magnitude, total number of data points and plate size. For this illustration purpose, criteria values of Config-1 obtained by using 1×1 virtual element are compared to a case when the parameters, force magnitude, total number of data points and plate size, are changed. The values obtained in these two cases are very similar. This numerical example illustrates the fact that, after normalization the two configurations are well independent of the varied parameters and are directly comparable.

	$\delta^{a}_{(D_{xx})}$	$\delta^{b}_{(D_{yy})}$	$\delta^{c}_{(D_{ss})}$	$\delta^{d}_{(D_{xy})}$
$F = 5N$ $n_e = 48 \times 48 = 2304$ $S = 100mm \times 100mm$	29.08	25.92	10.47	69.75
$F = 100N$ $n_e = 60 \times 60 = 3600$ $S = 200mm \times 200mm$	28.77	26.68	10.62	67.26

Table 5.1: A numerical illustration to show the normalization of the sensitivity criteria with respect to force magnitude, total number of data points (n_e) and plate size.

Now, in order to consider the rigidities altogether, the following global cost function is introduced

$$\mathrm{g} = \sum_{\alpha=1}^{3} \sum_{\beta>\alpha}^{4} \left| (\delta^{(\alpha)} - \delta^{(\beta)}) \right| \tag{5.2}$$

Finally, the testing configuration which provides the rigidity corresponding to α with the lowest sensitivity to noise exhibits the lowest δ^{α}. In the same way, the testing configuration which simultaneously provides a balanced noise sensitivity from one rigidity to another exhibits the lowest value of g. Noting that a set of higher individual criteria values may also result in a lower g, therefore it is worth verifying that the individual criteria values resulting in the lowest value of g are also acceptably low.

In the following sections, using above criteria, effect of different testing configurations on the unknown bending rigidities is studied. The idea is to identify one

configuration leading to more accurate rigidities which are least sensitive to noise. In addition, optimization of a given testing configuration is also discussed with respect to search of an optimum location for force application point, in such a way that this optimized configuration will lead to more robust identification.

5.3 Rating of the three tested configurations

An important feature of the present approach is its capability to grade the different testing configurations in terms of better identifiability. It is possible by comparing the normalized sensitivity indices defined above for the different configurations. Table 5.2 shows the criterion values g for the three tested configurations described in Fig 4.1. The values are presented for $4 \times 4 = 16$ piecewise virtual elements using noiseless data.

Set-ups	g
$Config-1$	89.76
$Config-2$	6.72
$Config-3$	117.12

Table 5.2: Normalized criterion values for $4 \times 4 = 16$ virtual elements using noiseless data.

Upon comparative study of the tested three configurations with reference to the criterion g presented in the above table, Config-2 proves to be more stable, robust and leads to better identification. The same conclusion may be derived from Fig 5.1 which presents the effect of increasing numbers of virtual elements without and with noise (amplitude of 5% of the maximum of curvature values in this later case).

In case of noiseless data no significant effect is observed in all the three configurations but it is very significant in case of noisy data. For Config-1 and Config-3 the identified values especially D_{xx} and D_{xy} deteriorate very sharply at each increasing numbers of virtual elements as can be seen in Fig 5.1. However, results remain reasonably stable for Config-2. This feature is related to the normalized sensitivity criterion values (g) reported in Table 5.2.

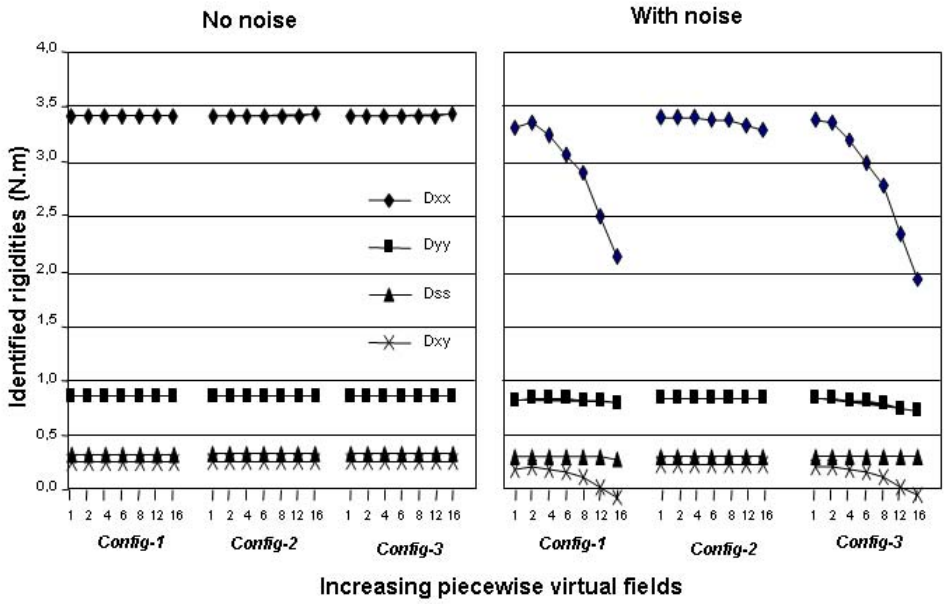

Figure 5.1: Grading of testing configurations: effect of increasing number of virtual elements.

It is interesting to note that it is also related to the virtual curvature fields obtained for configurations Config-1 and Config-2. These virtual curvature fields are respectively plotted in Fig 5.2. It may be observed that the deterioration of results in Config-1 especially in the case of noisy data is related to the pronounced discontinuity or gradients in the virtual curvature fields. On the other hand the virtual curvature fields for Config-2 are very much smoother and also the results are better.

It is shown that the present approach not only improves the identification but is also capable of indicating if a particular given testing configuration will lead to a better identification, especially in case of noisy data. Among the three studied configurations, Config-2 may be regarded as the optimum configuration, such that it will lead to more stable and robust rigidity identification when noisy data are processed.

One can also push forward the idea by moving the applied loading over the plate in search of a location which leads to the minimum value of the noise sensitivity criterion. The following section discusses this issue in detail.

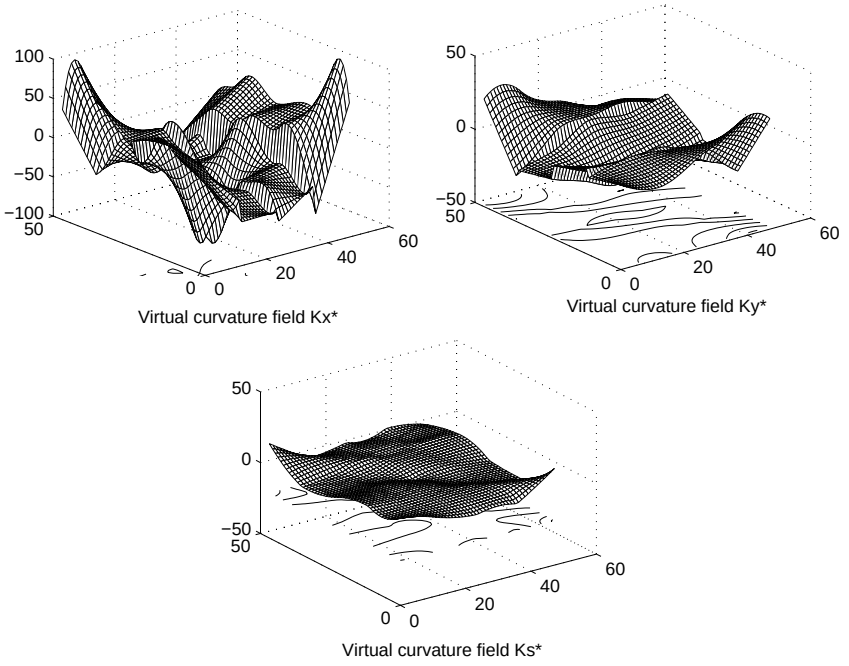

(a) Config-1

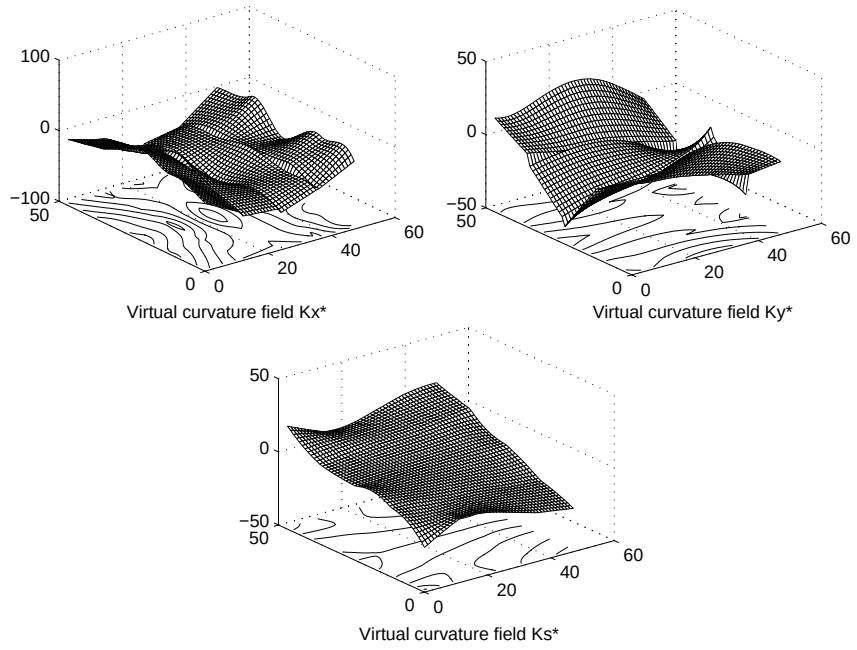

(b) Config-2

Figure 5.2: Virtual curvature fields for Config-1 and Config-2, using noisy data for $4 \times 4 = 16$ virtual elements.

5.4 Optimization of force application point

In this section, effect of loading position is studied on the specimen and corresponding identifiability. The idea is to find an optimal loading position for a given system of support locations such that better identification may be achieved.

Taking Config-1, load **F** is now moved within the plate and identification is achieved for each location. The corresponding values of δ^{α} (normalized sensitivity index) and g (global cost function) are noted for each point of force application. Recalling that, $\alpha = a, b, c, d$ represent D_{xx}, D_{yy}, D_{ss} and D_{xy} respectively. Thus, a thorough sensitivity scan is performed for the entire plate and the criteria values are recorded. Fig 5.4 presents the sensitivity analysis for each of the rigidities using the criterion $\delta^{(\alpha)}$ defined in Eq. (5.1). It also plots the sensitivity analysis using the global cost function g defined in Eq. (5.2). In the first case, the testing configuration is optimized for each of the four unknowns considered separately whereas they are globally considered in the second case.

Using the sensitivity scans in Fig 5.4, separate load application points are found for each of the unknown rigidity (at minimum value of $\delta^{(\alpha)}$). Also, a unique point using global cost function (at minimum value of g) is found which can identify all the rigidities with the best accuracy.

Fig 5.3 plots the different optimum load application points found from the individual and global sensitivity scans, whereas Table 5.3 records the noise sensitivity index values calculated at these respective optimum locations found for the noisy data with noise equal to 5% of the amplitude of the maximum of the absolute values of the three curvatures as used before.

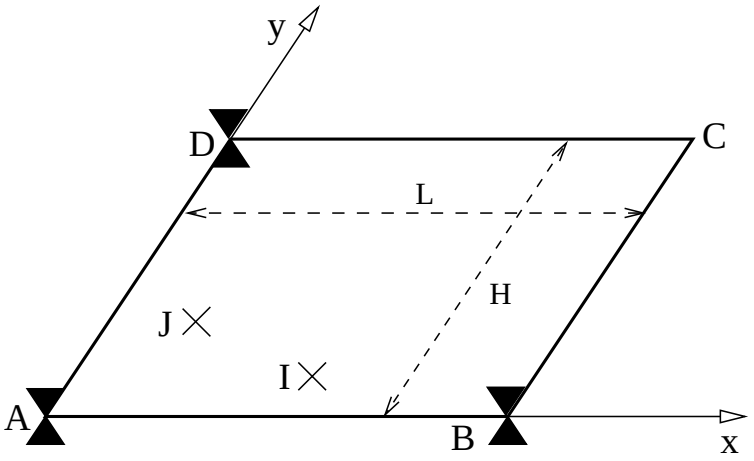

Figure 5.3: Config-1, optimum force locations, I (common to: $\delta^{(a)}$, $\delta^{(d)}$ and g) and J (common to: $\delta^{(b)}$, $\delta^{(c)}$).

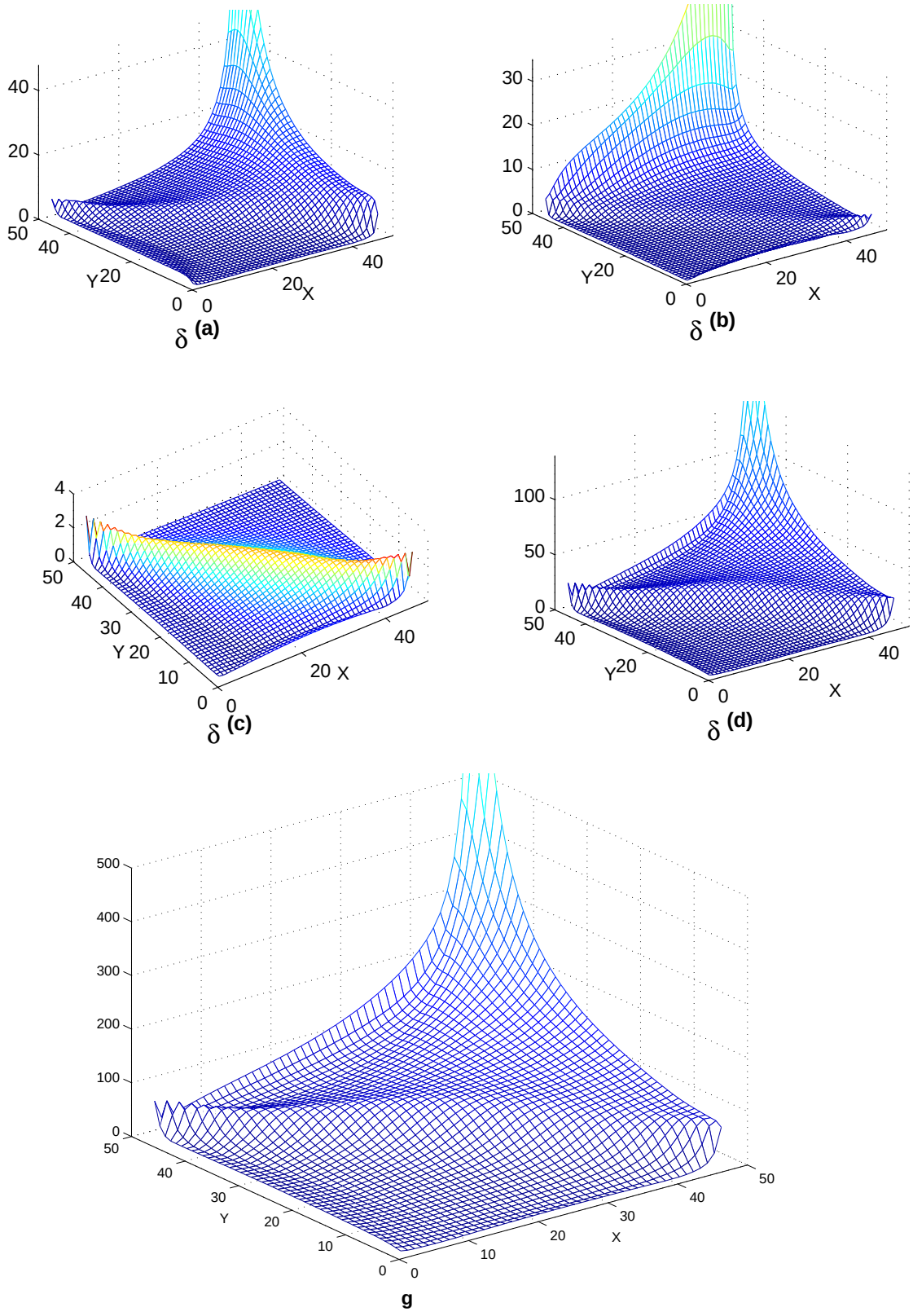

Figure 5.4: Config-1, 3D image of the respective individual and global noise sensitivity criteria.

Criteria :	force location (x,y) (mm)	$\delta^{(\alpha)}$ D_{xx}	D_{yy}	D_{ss}	D_{xy}	g
$\delta^{(a)}$, $\delta^{(d)}$, g	I(46,10)	0.65	0.96	0.56	2.4	5.83
$\delta^{(b)}$, $\delta^{(c)}$	J(17,27)	1.44	0.27	0.38	2.88	8.89

Table 5.3: Noise sensitivity index values $\delta^{(\alpha)}$ at optimum force locations for Config-1.

It is interesting to note that the identified location using the criterion g is common to both D_{xx} and D_{xy}. It must also be pointed out that the index values reported in Table 5.3 are more balanced in line1 as in line2, as expected. It may be concluded that a single test can effectively be performed to extract all the unknown rigidities rather than performing separate tests for each rigidity, without much loosing in terms of result stability and accuracy. Also it is worth noting that it should be avoided to choose a loading applied along the diagonal drawn between the two opposite supports. Another feature is the fact that the cost function is flat over large zones, meaning there will not be important loss of accuracy when moving the applied loading over these zones. However, a load position in close proximity to the supports should not be used due to little deflections thus produced.

configuration:	$\delta^{(\alpha)}$ D_{xx}	D_{yy}	D_{ss}	D_{xy}	g
Config-1	6.72	2.4	1.92	30.24	89.76
Applied loading at I(46,10)	0.65	0.96	0.56	2.4	5.83

Table 5.4: Config-1: results before and after optimization.

Finally Table 5.4 compares the results of Config-1 in terms of noise sensitivity index values, $\delta^{(\alpha)}$, to that of optimized configuration obtained from global criterion g. The improvement in identification is observed in terms of accuracy and robustness in case of optimized force application point $I(46, 10)$.

Regarding Config-1, another important point to be noted is that an applied loading located at the free corner of the plate (point C) is the worst situation for D_{xx}, D_{yy} and D_{xy}. In this case the plate is under pure twisting (i.e. $k_x = k_y = 0$, $k_s = constant$) as shown in refs. [74, 78]. D_{xx}, D_{yy} and D_{xy} do not influence at all the response of the plate in this case. Consequently they cannot be identified whatever the identification method used. This latter loading case is often referred to as 'anticlastic bending'. It is interesting to note that because of the flatness of cost function δ^c, several locations for the applied loading could be used in practice. For instance, it can be checked that C and J are approximately equivalent in terms of

value of the cost function. At this latter point however, not only results are better for D_{ss} but it is also capable of finding other rigidities with a good accuracy too.

5.5 Effect of material

In this section effect of using a different material is considered on the sensitivity analysis and eventual identification of an optimal force location. The idea is to study if a change in material leads to a new optimum force location or has only a slight effect. Fig 5.5 presents global sensitivity scan using criterion g for carbon-epoxy composite plates with typical elastic constants as: $E_x = 130\ GPa$, $E_y = 10\ GPa$, $\nu_{xy} = 0.3$ and $G_{xy} = 5\ GPa$. The experimental set up is the kept the same as that of Config-1.

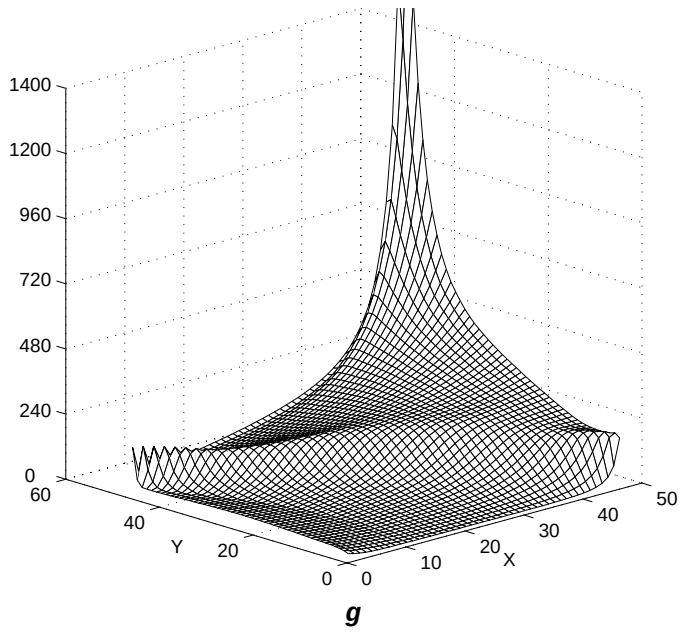

Figure 5.5: Config-1, 3D image of the noise sensitivity criteria for carbon epoxy : g

The sensitivity scans for the two different materials, glass epoxy and carbon-epoxy, represent almost the same behavior. Thus for the above studied case it may be concluded that results are not very sensitive to the choice of material used.

5.6 Conclusion

This chapter presents an important application of the developed piecewise virtual fields method with noise minimization effect [79, 80, 81]. It is shown that the method can be used as grading tool when different testing configurations are to be compared. The normalization of the selection criterion based on the noise sensitivity index is also discussed. It is important when different testing configurations are to be compared. With the help of numerically simulated examples of three different testing configurations it is shown that the configurations can be graded with respect to better identifiability and least sensitivity to noise. Optimization of a given testing configuration is also discussed, though it is limited to the search of an optimized force application point only. Making use of simulated noisy data, the improvement in terms of identifiability and reduced noise sensitivity is compared when identification is achieved by using such an optimized force application point. An illustrative example of a carbon-epoxy composite plate is also studied. For the studied case, it is observed that the optimized location of a force application point remains largely insensitive to the choice of material.

Now the following chapter discusses the optimization of testing configuration in detail. Such that effect of different variable parameters like fiber angle, plate width, location of force application point, location of support points and specimen shape are studied.

Chapter 6

Optimization of testing configuration

6.1 Introduction

In this chapter the effect of different parameters like fiber angle, plate width, location of force application point, location of support points and specimen shape are studied on the noise sensitivity criterion such that better identification is achieved. In order to evaluate the gain in terms of robustness and accuracy of the results, the different variable parameters, considered separately and also in combination are as follows:

1. Angle of fiber.
2. Width of specimen.
3. Width + angle.
4. Force.
5. Support (restricted along specimen boundary) + force.
6. Support (restricted along specimen boundary) + force + angle.
7. Support + force.
8. Support + force + angle.
9. Shape of specimen.
10. Shape of specimen + support + force.

The idea is to study and verify the fact that when greater number of above variable parameters are considered collectively, greatest is the gain in terms of reduced noise sensitivity.

This is due to the fact that increasing number of degrees of freedom are available for solving the problem. In order to compare the different situations where specimen dimension or eventually shape is altered, normalized sensitivity criteria values δ^{α} defined earlier in Section 5.2 are used. Recalling that, $\alpha = a, b, c, d$ represent D_{xx}, D_{yy}, D_{ss} and D_{xy} respectively. For quick reference this normalized sensitivity index given earlier in Eq. (5.1) is reported below.

$$\delta^{\alpha} = \eta^{\alpha}/D_{\alpha} \times w_{max} \times \sqrt{n_e} \times (1/S)$$

6.1.1 Definition of global cost functions

In order to consider the effect of the rigidities altogether, four different global cost functions are introduced here. These are noted as: $g1$ (sum), $g2$ (balanced), $g3$ (ratio balanced) and $g4$ (ratio squared balanced) and are defined as follows

$$g1 = \sum_{\alpha=1}^{4} \left|\delta^{(\alpha)}\right| \tag{6.1}$$

$$g2 = \sum_{\alpha=1}^{3} \sum_{\beta>\alpha}^{4} \left|(\delta^{(\alpha)} - \delta^{(\beta)})\right| \;=\; \mathrm{g} \tag{6.2}$$

$$g3 = \frac{g2}{g1} \tag{6.3}$$

$$g4 = \frac{\sum_{\alpha=1}^{3} \sum_{\beta>\alpha}^{4} \left|(\delta^{(\alpha)} - \delta^{(\beta)})^2\right|}{\sum_{\alpha=1}^{4} \left|\delta^{(\alpha)2}\right|} \tag{6.4}$$

It is interesting to note that $g1$ takes into account all the respective individual sensitivity values by simple addition whereas $g2$ (similar to g as noted in Eq. (5.2)) considers their relative differences. Due to this a minimum $g2$ value will represent a more balanced combination of individual sensitivity values as their respective weights are also taken into consideration. However, as mentioned earlier in Section 5.2, it is important to verify that the corresponding set of individual criteria values resulting in a minimum $g2$ value are also acceptably low. Now, for both criteria, $g3$ and $g4$, it may be noted that they present a ratio formulation and are slight variants of one another. This type of cost function has earlier been used in the literature [82]. One advantage of their utilization may be the fact that they are independent of any sort of normalization as it is automatically taken into account in their formulation. However, it is interesting to note that both $g3$ and $g4$ may result in individual criteria values which are not minimal. For better understanding, such a situation may be imagined where all the individual sensitivity values are higher. Now the numerator in both of these criteria which is a relative difference

will remain minimum but the denominator which is a simple addition will result in a maximum. Finally a ratio involving a division of a minimum value by a maximum value will lead to a even more lesser result. Thus, a minimum $g3$ or $g4$ criterion value may correspond to a combination of maximum possible individual sensitivity indices, which is not desirable. The present study gives an opportunity to study the effect of these different criteria and to identify the one that is more representative.

It should be noted here that the present study makes use of only one virtual element in order to avoid the computational complexities especially for the case when specimen shape is optimized. In addition the identification program is modified for the case of orthotropic plates, such that only four rigidities are identified in the fiber direction. This gives a common reference platform when optimum fiber angle is searched and while other parameters are made variable along with fiber angle. In the present study, Config-1 and Config-2 described earlier in Section 4.1, are used to study the effect of different variable parameters. These two testing configuration are replotted in Fig 6.1.

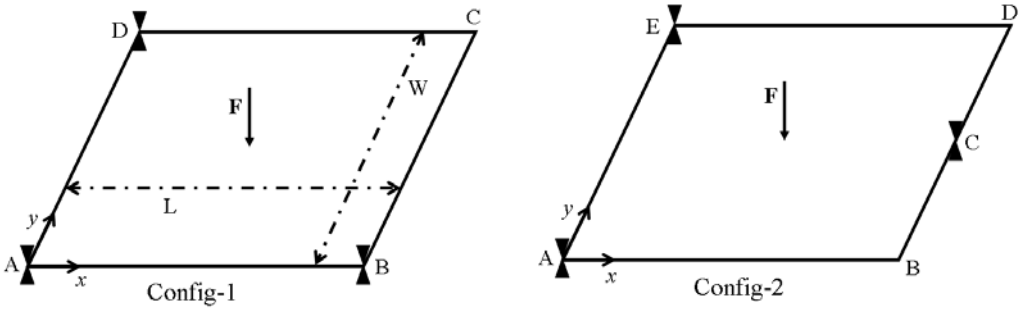

Figure 6.1: The two testing configuration used to study the effect of different variable parameters.

Reference global and individual criteria values for Config-1 and Config-2 are recorded in Table 6.1 and Table 6.2 respectively. This serves as reference values when different variable parameters will be discussed and using their optimum values new criteria values are evaluated.

	Config - 1	**Config - 2**
Crt:	crt. values	crt. values
$g1$	26.60	6.60
$g2$	55.70	11.35
$g3$	2.10	1.72
$g4$	1.98	1.86

Table 6.1: Reference global criteria values for Config-1 and Config-2.

	Config - 1	**Config - 2**
Crt:	crt. values	crt. values
$\delta^{(a)}$	7.43	0.94
$\delta^{(b)}$	1.56	0.75
$\delta^{(c)}$	0.50	0.59
$\delta^{(d)}$	17.11	4.31

Table 6.2: Reference individual noise sensitivity values for Config-1 and Config-2, $\delta^{(\alpha)}$, $\alpha = a, b, c, d$ represent D_{xx}, D_{yy}, D_{ss} and D_{xy} respectively.

Now the following section first discusses the effect of varying fiber angles in order to identify the optimum fiber angle which will result in reduced noise sensitivity.

6.2 Optimization of fiber angle

In this section effect of changing fiber angle is studied on the rigidity identification. Plate dimension, support and force application points remain unchanged. Using Config-1 and Config-2, fiber angles are varied from 0° to 180° with 5° regular increments. For a given fiber angle, rigidities and associated criteria values are calculated in the fiber direction.

Change in respective criteria values with respect to varying fiber angles are plotted in Fig 6.2 and Fig 6.3 respectively for Config-1 and Config-2. It may be observed that no unique value is found from all the criteria. However it is interesting to note that the first two criteria, $g1$ and $g2$, result in the same optimum fiber angle. Separately, similar optimum fiber angles are found using criteria $g3$ and $g4$. Here it is interesting to note the presence of two symmetry axes respectively at 45° and 135° in case of Config-1 whereas one symmetry axis is located at 90° for Config-2. Additionally with respect to global cost functions $g1$, $g2$ and individual sensitivity values $\delta^{(\alpha)}$, it is observed that for each fiber angle used, corresponding sensitivity values for Config-1 are in general greater than that of Config-2.

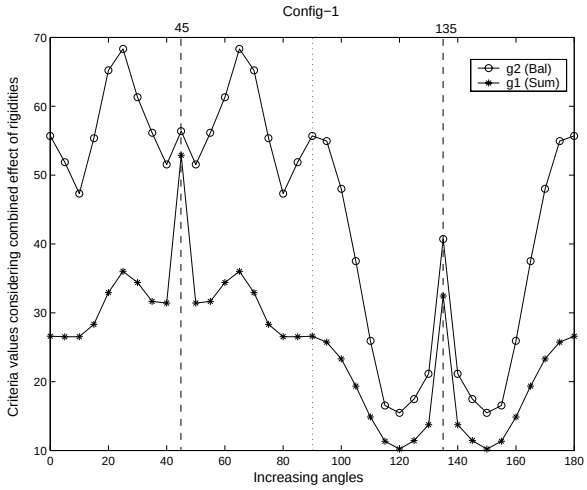

(a) Global minimization criteria values using cost functions: $g1$ and $g2$

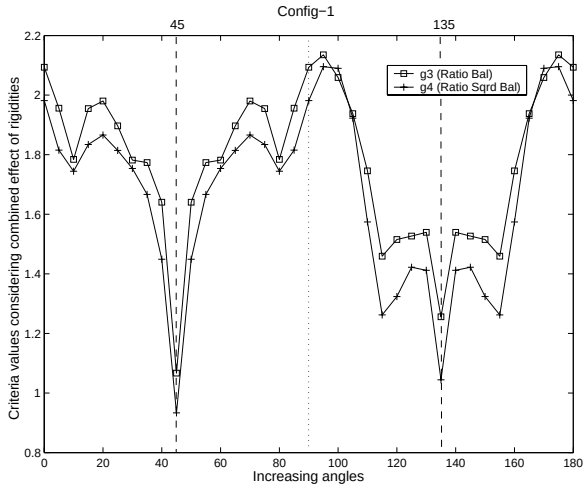

(b) Global minimization criteria values using cost functions: $g3$ and $g4$

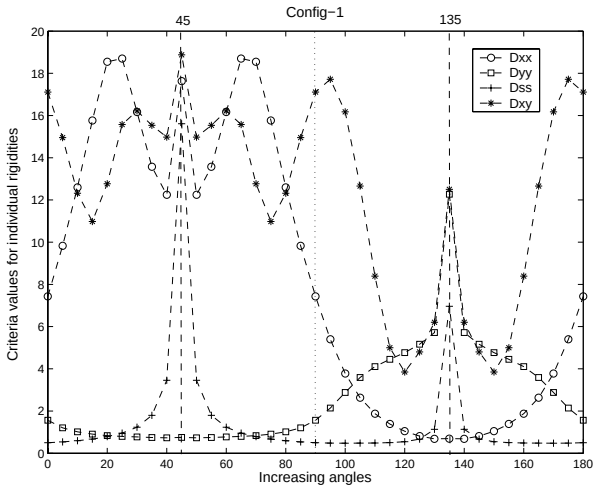

(c) Individual minimization criteria values using cost functions: $\delta^{(\alpha)}$

Figure 6.2: Config-1, Effect of varying angles on different minimization criteria values using fixed plate dimension, supports and force points.

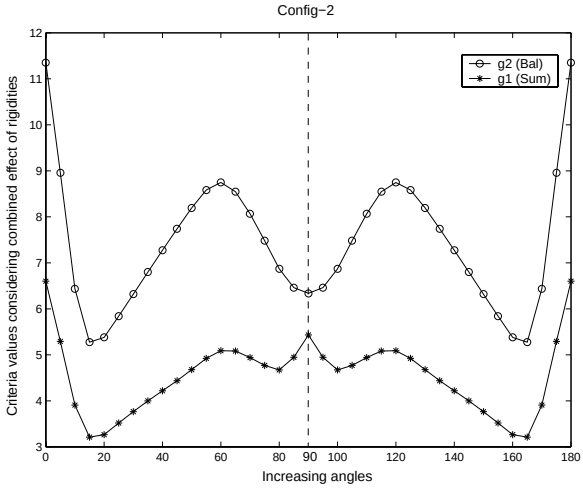

(a) Global minimization criteria values using cost functions: $g1$ and $g2$

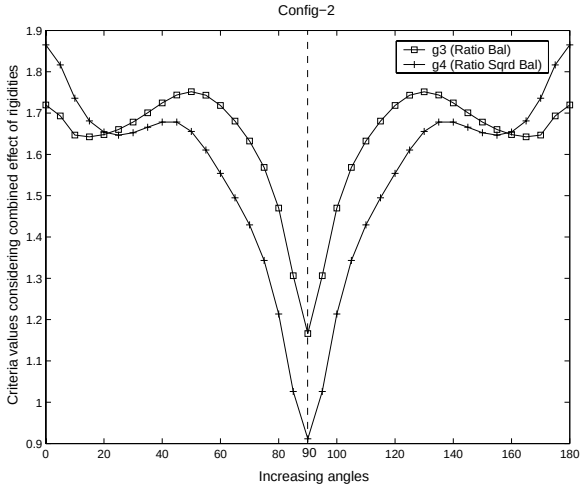

(b) Global minimization criteria values using cost functions: $g3$ and $g4$

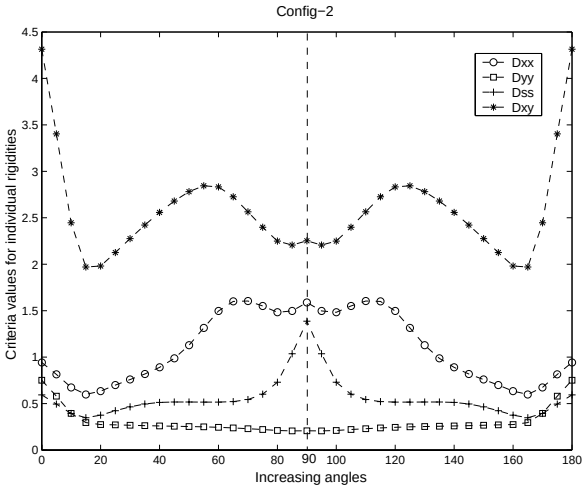

(c) Individual minimization criteria values using cost functions: $\delta^{(\alpha)}$

Figure 6.3: Config-2, Effect of varying angles on different minimization criteria values using a constant dimension plate, fixed supports and force points.

On this basis it may also be said that Config-2 is comparatively better than Config-1 and is less sensitive to noise. Table 6.3 presents the optimum fiber angle when combined effect of all the four rigidities is considered using the global cost functions, $g1$, $g2$, $g3$ and $g4$. Table 6.4 presents the optimum fiber angle for better identification of separate rigidities at minimum values of $\delta^{(\alpha)}$ (sensitivity index). The idea is to determine the optimum fiber angle for a given testing configuration which leads to better identification with minimum sensitivity to noise.

	Config - 1		**Config - 2**	
Crt:	crt. values	angles °	crt. values	angles °
$g1$	10.20	150	3.21	15
$g2$	15.46	150	5.27	15
$g3$	1.07	45	1.17	90
$g4$	0.93	45	0.91	90

Table 6.3: Optimum fiber angles considering combined effect of rigidities.

	Config - 1		**Config - 2**	
Crt:	crt. values	angles °	crt. values	angles °
$\delta^{(a)}$	0.68	140	0.60	15
$\delta^{(b)}$	0.73	40	0.20	95
$\delta^{(c)}$	0.48	170	0.35	165
$\delta^{(d)}$	3.84	150	1.97	15

Table 6.4: Optimum fiber angles separately for individual rigidities.

	Config - 1		**Config - 2**	
Crt:	crt. values at 150 ° ($g1$, $g2$)	crt. values at 45 ° ($g3$, $g4$)	crt. values at 15 ° ($g1$, $g2$)	crt. values at 90 ° ($g3$, $g4$)
$\delta^{(a)}$	1.04	17.63	0.60	1.59
$\delta^{(b)}$	4.77	0.75	0.29	0.21
$\delta^{(c)}$	0.55	15.61	0.34	1.39
$\delta^{(d)}$	3.84	18.87	1.97	2.25

Table 6.5: Comparison of individual criteria values $\delta^{(\alpha)}$ at optimum fiber angles found for different global criteria.

Total four different global criteria, viz. $g1$, $g2$, $g3$ and $g4$ are used to find the optimum fiber angles. From the results quoted in Table 6.3 it may be observed that

the first two criteria, $g1$ and $g2$, find the same optimum fiber angle. Separately, similar optimum fiber angles are found using criteria $g3$ and $g4$.

Table 6.5 records values of individual sensitivity indices ($\delta^{(\alpha)}$) for respective rigidities at these different optimum fiber angles for the two tested configurations. From this comparative study, it is observed that the global criteria, $g1$ or $g2$ is more efficient and results in lesser noise sensitivity indices ($\delta^{(\alpha)}$) especially for Config-1, as compared to the corresponding values at optimum fiber angle found using criteria $g3$ or $g4$. As explained earlier in Section 6.1.1, it is due to the ratio formulation of these criteria, such that a minimum $g3$ or $g4$ criteria value may correspond to a combination of maximum possible individual sensitivity indices, which is not desirable. The same observation is also visible in Fig 6.2 and Fig 6.3. For example, for the case of Config-1, in Fig 6.2(a) and Fig 6.2(b), the presence of sharp peaks respectively at 45° and 135° may be explained on account of the higher individual sensitivity values found at these angles in Fig 6.2(c). Contrary to this a minimum $g1$ or $g2$ criteria value corresponds to a combination of minimum possible individual sensitivity indices. Thus, using these global criteria, best identification is possible for all the unknown rigidities with least sensitivity to noise. Recalling that criteria $g2$ is a summation of differences of rigidities, a minimum value of $g2$ represents a situation where the respective weights of all the sensitivity indices corresponding to each rigidity are more balanced. However it is worth verifying that the corresponding set of individual criteria values in case of $g2$ are also lower than the ones used in $g1$.

6.3 Optimization of specimen width

In this section effect of varying plate dimensions are studied such that plate length is kept fixed whereas its width is varied, thus leading to a variable aspect ratio. A constant 0° fiber angle is used. For Config-1 and Config-2, plate length is kept fixed to $0.1m$ while width is varied from $0.03m$ to $0.15m$ successively with $0.01m$ regular increments. However, same positions of support application points (at the plate corners) and force application point (at the center of plate) are considered in each case.

The observed variations in respective criteria values with respect to varying widths are plotted in Fig 6.4 and Fig 6.5 respectively for Config-1 and Config-2. Table 6.6 presents the optimum width when combined effect of all the four rigidities is considered. Table 6.7 presents the optimum width for better identification of separate rigidities for a fixed plate length of $0.1m$ and 0° fiber angle.

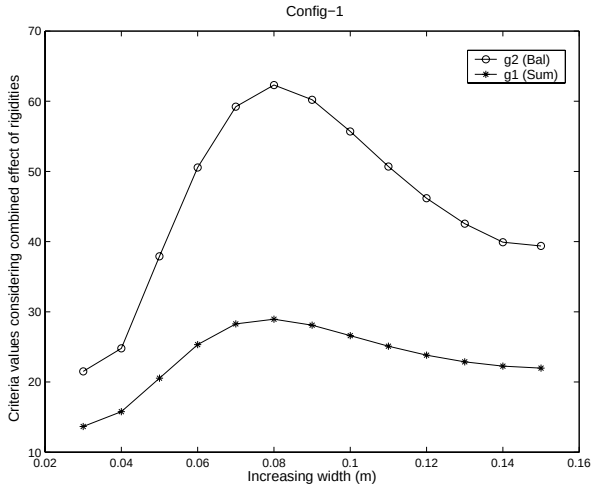

(a) Global minimization criteria values using cost functions: $g1$ and $g2$

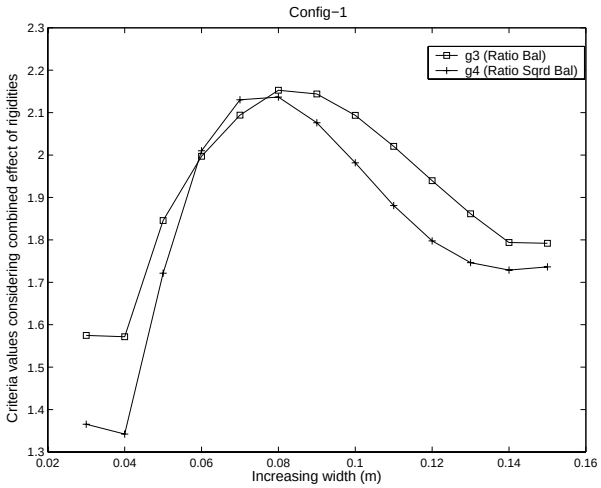

(b) Global minimization criteria values using cost functions: $g3$ and $g4$

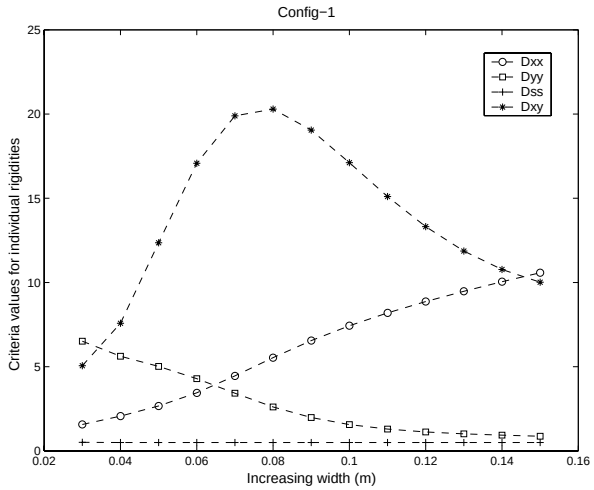

(c) Individual minimization criteria values using cost functions: $\delta^{(\alpha)}$

Figure 6.4: Config-1, Effect of varying widths on different minimization criteria values using a plate of constant length, fixed 0° fiber angle, supports and force points.

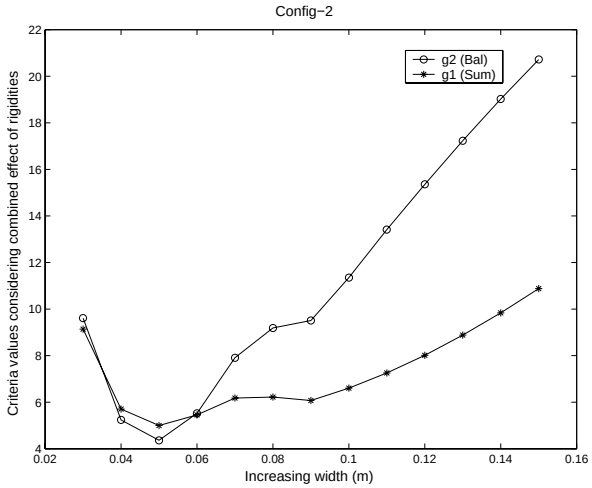

(a) Global minimization criteria values using cost functions: $g1$ and $g2$

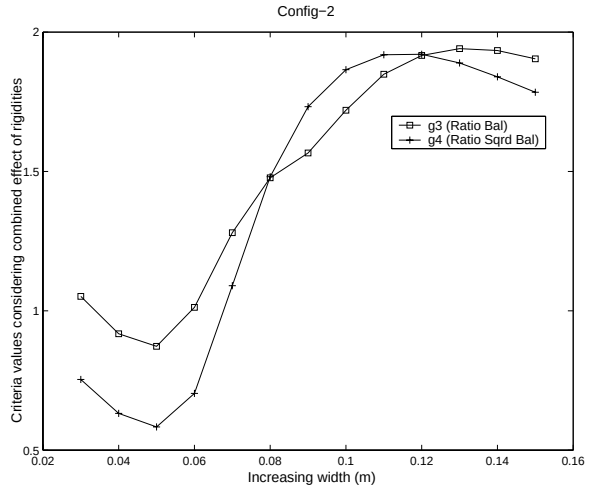

(b) Global minimization criteria values using cost functions: $g3$ and $g4$

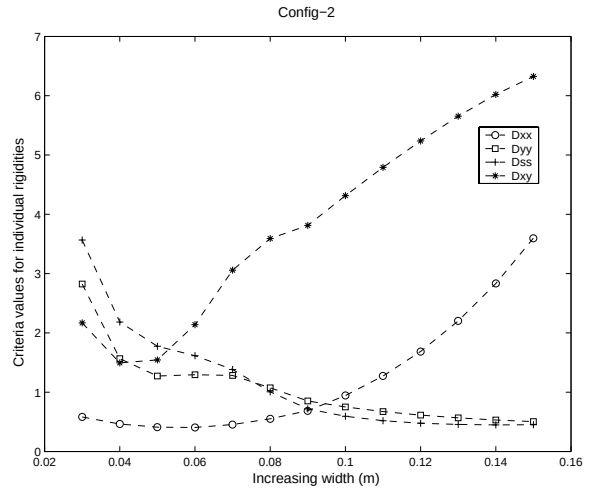

(c) Individual minimization criteria values using cost functions: $\delta^{(\alpha)}$

Figure 6.5: Config-2, Effect of varying widths on different minimization criteria values using a plate of constant length, fixed 0° fiber angle, supports and force points.

	Config - 1		Config - 2	
Crt:	crt. values	width (mm)	crt. values	width (mm)
$g1$	13.65	30	5.00	50
$g2$	21.51	30	4.36	50
$g3$	1.57	40	0.87	50
$g4$	0.93	40	0.58	50

Table 6.6: Optimum plate widths considering combined effect of rigidities.

	Config - 1		Config - 2	
Crt:	crt. values	width (mm)	crt. values	width (mm)
$\delta^{(a)}$	1.57	30	0.40	60
$\delta^{(b)}$	0.87	150	0.50	150
$\delta^{(c)}$	0.50	50	0.45	140
$\delta^{(d)}$	5.06	30	1.49	40

Table 6.7: Optimum plate widths separately for individual rigidities.

From the obtained results it may be concluded that lesser is the width as compared to length better would be the results. Here it is important to note that the slope fields obtained on top surface of the specimen are practically captured using a camera, typically equipped with rectangular CCD array. For instance Basler A113P camera, used in the present study for capturing experimental slope fields, is equipped with a CDD array of 1296×1030 pixels, with an aspect ratio of 1.26. This limits the use of very elongated specimen as the CCD camera is then not best suited. Hence a rectangular specimen with aspect ratio closer to that of the CCD array is more preferable than a very elongated one.

6.4 Optimization of specimen width and fiber angle

In this section the effect of both width and fiber angle is studied. The idea is to identify a combination of optimum width and fiber angle for Config-1 and Config-2 for better and robust identifiability of rigidities. For this purpose identification is achieved for the widths varying from $0.03m$ to $0.15m$ successively with $0.01m$ regular increments using a given fiber angle. Also for each width, identification is achieved for all the angles varying from 0° to 180° with 5° regular increments. Finally, that combination of optimum width and fiber angle is identified which results in the least values of global minimization criteria and similarly for individual criteria.

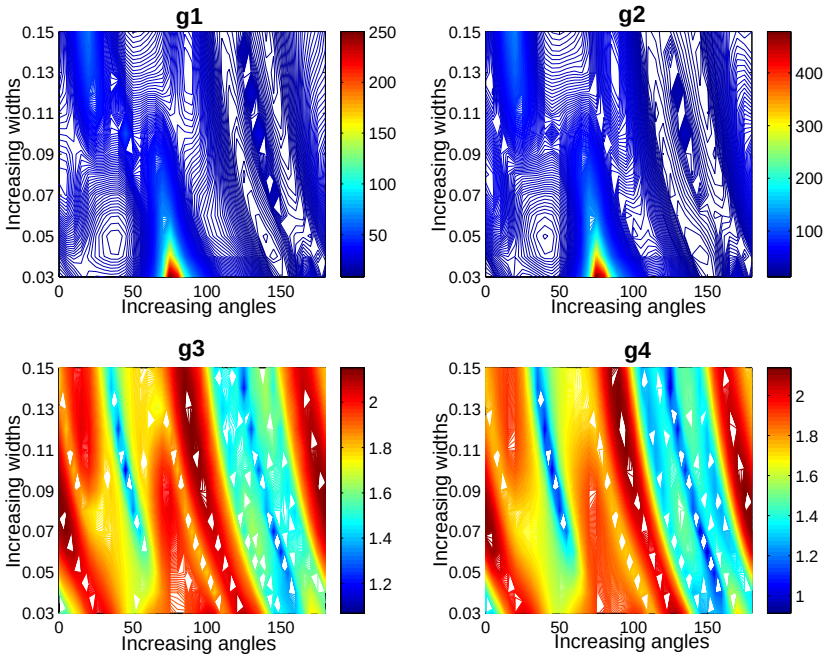

(a) Global criteria contour plots: $g1$, $g2$, $g3$ and $g4$

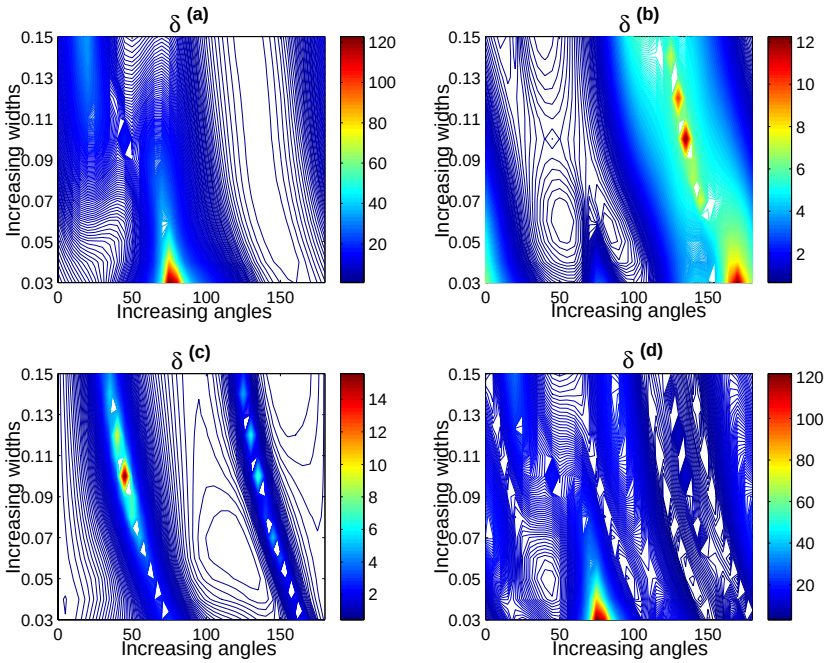

(b) Individual criteria contour plots: $\delta^{(a)}$, $\delta^{(b)}$, $\delta^{(c)}$ and $\delta^{(d)}$

Figure 6.6: Config-1, Effect of varying widths and angles on the global and individual minimization criteria respectively.

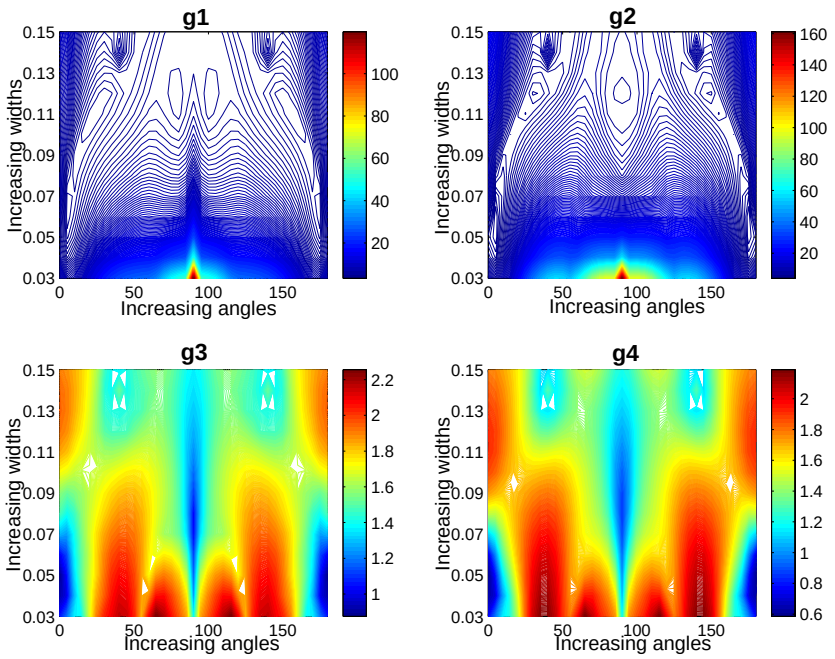

(a) Global criteria contour plots: $g1$, $g2$, $g3$ and $g4$

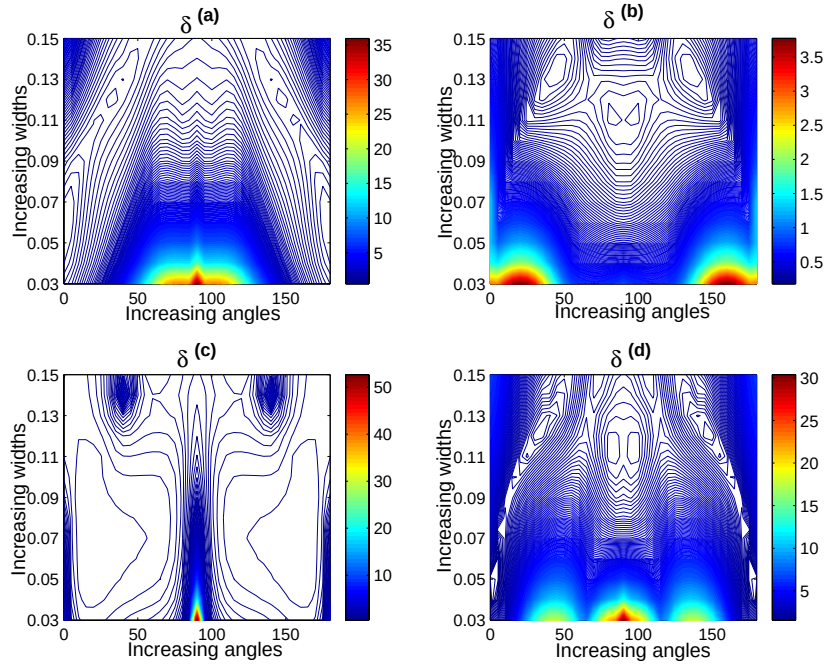

(b) Individual criteria contour plots: $\delta^{(a)}$, $\delta^{(b)}$, $\delta^{(c)}$ and $\delta^{(d)}$

Figure 6.7: Config-2, Effect of varying widths and angles on the global and individual minimization criteria respectively.

As before, same positions of support application points (at the plate corners) and force application point (at the center of plate) are considered in each case.

Fig 6.6 and Fig 6.7 present the contour plots using global and individual cost functions respectively for Config-1 and Config-2. These plots record the respective criteria values for the widths varying from $0.03m$ to $0.15m$ with $0.01m$ regular increments and the angles varying from $0°$ to $180°$ with $5°$ regular increments. In general, it may be observed that for a given configuration, the two criteria $g1$ and $g2$ exhibit a similar pattern, and the same is separately true for $g3$ and $g4$. Also, it may be observed that, both $g1$ and $g2$ result in comparatively less complicated contour maps with distinct flat regions having lesser criteria values.

On the other hand, the contour maps of $g3$ and $g4$ are very uneven with sharp fluctuations and as such no flat zones with lesser criteria values are visible. Regarding the individual criteria maps in both the configurations, flat zones with lesser respective criterion values are easily visible. Additionally, for Config-2, a symmetric pattern is remarkable in all the plots.

	Config - 1			**Config - 2**		
Crt:	crt. values	width (mm)	angles °	crt. values	width (mm)	angles °
$g1$	8.09	40	145	3.08	110	25
$g2$	12.17	40	145	3.70	60	5
$g3$	1.07	100	45	0.87	50	180
$g4$	0.91	60	150	0.58	50	180

Table 6.8: Optimum plate widths and angles considering combined effect of rigidities.

	Config - 1			**Config - 2**		
Crt:	crt. values	width (mm)	angles °	crt. values	width (mm)	angles °
$\delta^{(a)}$	0.58	150	125	0.40	60	0
$\delta^{(b)}$	0.61	60	50	0.17	130	40
$\delta^{(c)}$	0.42	150	150	0.35	100	165
$\delta^{(d)}$	2.95	150	140	1.49	40	0

Table 6.9: Optimum plate widths and angles separately for individual rigidities.

Table 6.8 records the optimum combination of width and fiber angle for Config-1 and Config-2 based on the global minimization criteria. Table 6.9 records the optimum combination based on the individual minimization criterion for each of the rigidities. From above results, it is observed that for better and more robust identification elongated specimens sizes are preferred choice. Similar conclusion was also observed earlier in Section 6.3. However as explained earlier in Section 6.3,

from experimental point of view where a CCD camera is used to capture the full field data, use of very elongated specimens is not recommended.

6.5 Optimization of force application point

This section presents the effect of location of load application point when it is moved from one position to another. The detailed search procedure for an optimized force application point is already discussed in Section 5.4. The present case only differs on account of using one virtual element in addition to an identification of the four orthotropic rigidities along the fiber directions instead of six. This leads to different noise sensitivity criteria values compared to their counterparts found in Section 5.4. Hence, the program is launched again with four unknowns instead of six and corresponding values of global and individual cost functions in addition to the location of optimum force application point are recorded here in Table 6.10 and Table 6.11 respectively.

	Config - 1			**Config - 2**		
Crt:	crt. values	F_x (mm)	F_y (mm)	crt. values	F_x (mm)	F_y (mm)
$g1$	5.19	37.5	8.3	4.76	58.3	41.6
$g2$	6.68	60.4	4.2	8.54	58.3	41.6
$g3$	1.19	37.5	4.2	1.63	18.7	4.2
$g4$	1.02	43.7	4.2	1.46	12.5	97.9

Table 6.10: Optimum location of force application point considering combined effect of rigidities.

	Config - 1			**Config - 2**		
Crt:	crt. values	F_x (mm)	F_y (mm)	crt. values	F_x (mm)	F_y (mm)
$\delta^{(a)}$	0.53	64.5	4.2	0.71	58.3	41.6
$\delta^{(b)}$	0.31	16.6	31.2	0.34	4.1	85.4
$\delta^{(c)}$	0.35	6.2	77.1	0.26	29.1	27.1
$\delta^{(d)}$	1.85	66.6	2.1	3.12	58.3	41.6

Table 6.11: Optimum location of force application point separately for individual rigidities.

From above results it is observed that the use of optimal load application point leads to considerable reduction in noise sensitivity values. However it is observed that different global criteria result in different optimum locations. For Config-1 it may be said that they are more or less close to each other but not in case of Config-2. Table

	Config - 1				Config - 2			
Crt:	$g1$	$g2$	$g3$	$g4$	$g1$	$g2$	$g3$	$g4$
$\delta^{(a)}$	0.55	0.55	0.57	0.58	0.71	0.71	1.06	0.95
$\delta^{(b)}$	1.09	2.15	2.4	2.45	0.63	0.63	1.74	1.80
$\delta^{(c)}$	0.44	0.55	0.69	0.68	0.29	0.29	0.29	0.29
$\delta^{(d)}$	3.11	2.24	2.42	2.33	3.12	3.12	3.83	3.68

Table 6.12: Comparison of individual criteria values $\delta^{(\alpha)}$ at optimum force locations found for different global criteria.

6.12 records individual sensitivity values of respective rigidities found at the optimum force application points using global cost functions. A similar pattern is observed as before in Table 6.5. Thus, it may be said that global criteria $g1$ and $g2$ are more performing as they are related to lesser individual sensitivity values. Contrary to this, minimum values of $g3$ and $g4$ are related to a combination of somewhat higher individual sensitivity values. Recalling that the criterion $g2$ is a summation of differences of rigidities. Hence a minimum value represents a situation where the respective weights of all the sensitivity indices corresponding to each rigidity are more balanced. This makes it most suitable choice as a global optimization criteria based on noise minimization which is able to identify one optimal situation for best possible identification of all the unknown rigidities.

Now the following section further extends the optimization scope. It discusses the effect of optimized fiber angle, support locations and force application point in order to study the combined effect of all these variable parameters on the noise sensitivity values. For the following study Config-1 is used as reference testing configuration whereas global criterion $g2$ is used as the selection criterion.

6.6 Optimization of support points, force point and fiber angle for fixed specimen shape

6.6.1 Introduction

This section now discusses the effect of different variable parameters viz. support positions, force application point and fiber angle. For this study Config-1 serves as a reference and starting point. To be noted that for all the studies to follow, optimum parameter values are found using the global minimization criterion $g2$. The idea is to find optimum values of these parameters in addition to verifying the fact that better identification is possible with increasing number of optimized variables. For this

purpose using the optimized criteria values, percentage reductions in comparison to the reference values for Config-1 as noted in Table 6.1 and Table 6.2, are evaluated. In this regard, Table 6.13 summarizes the results of the criteria values along with the *% reductions* obtained for the different optimization cases undertaken in an orderly way as listed in Section 6.1.

Comparison of the criteria values and *% reduction* for the different optimization cases					
Cases	$g2$	$\delta^{(a)}$	$\delta^{(b)}$	$\delta^{(c)}$	$\delta^{(d)}$
Ref values Config-1	55.70 -	7.43 -	1.56 -	0.50 -	17.11 -
1. Angle	15.46 *72.24*	1.04 *85.98*	4.77 *-204.93*	0.55 *-9.38*	3.84 *77.55*
2. Width	21.51 *61.39*	1.57 *78.87*	6.52 *-317.15*	0.51 *-1.80*	5.06 *70.43*
3. Width + angle	12.17 *78.15*	0.78 *89.25*	3.83 *-144.80*	0.49 *1.30*	2.97 *82.63*
4. Force	6.68 *88.00*	0.55 *92.63*	2.15 *-37.24*	0.55 *-9.58*	2.24 *86.90*

Table 6.13: A successive comparison of the reference global ($g2$) and individual sensitivity criteria ($\delta^{(\alpha)}$) for the different optimization cases as listed in Section 6.1.

6.6.2 Optimization procedure

This section presents the procedure to select a successively improved location of variable parameters. For this purpose, Fig 6.8 illustrates the search method used for finding the optimized positions for variable parameters. It has a total of eight variable parameters, representing positions in x and y directions for three supports and one force point. Also it contains a real mesh grid as used in Ansys for simulation purposes and the resulting *pitch* size. Pitch depends on the mesh size used, denser is the mesh grid smaller is the pitch size. The intersection points of vertical and horizontal lines represent allowable possible positions where these variable parameters can be placed.

Now to start the search procedure, first keeping all the variable parameters location unchanged, identification is achieved and the selection criterion value $g2$ is noted. Now one of the parameters is taken and its location is changed by giving a predefined displacement, referred to as *step* respectively in $+x$ direction and identification is achieved along with recording the new criterion value of $g2$. The step size may be taken equal to the pitch or its factor (e.g. twice or four times of the pitch size). In a similar manner, the same original location is given displacements

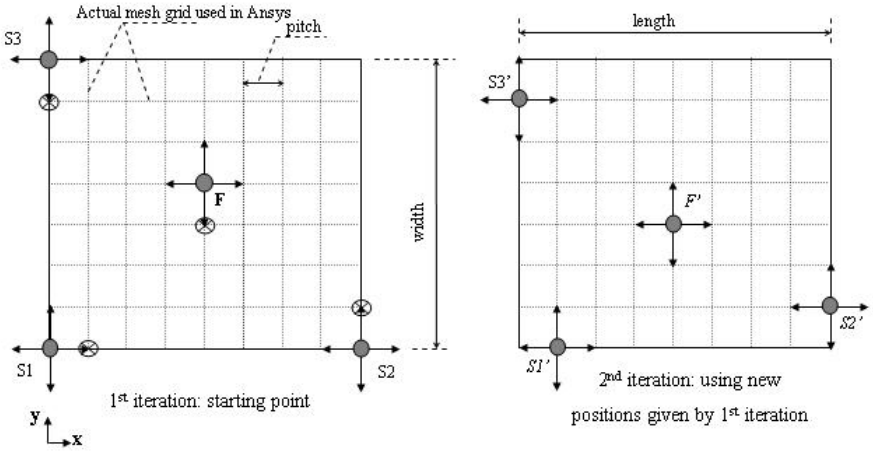

Figure 6.8: An illustration to describe the search method for new successively optimized locations.

respectively in $-x$, $+y$ and $-y$ directions separately. At all these new locations identification is achieved one after another and $g2$ value is noted. Finally for this parameter total five different values of $g2$ are available among which the least value is identified and corresponding location is retained, which is represented in the illustration by $\otimes$. This new location will now be used afterwards for this tested variable parameter for subsequent loop of optimum search. Same procedure is now applied to the remaining three variable parameters and subsequent new locations are found for each of them one after another. This complete loop for four parameters as used in this example is referred to as first *iteration*. Finally at the end of first iteration, four new locations are available respectively for the four parameters which now serve as a starting point for the subsequent second iteration. This procedure is continued till the relative difference of criteria values for each variable parameter separately becomes less than or equal to 0.1%.

It is important to note that in order to save computational time, the step size which is the starting incremental displacement may be taken initially as some factor of the pitch (e.g. twice or four times of the pitch size). However, at the attainment of above limiting condition the step size is reduced to the pitch size and the search procedure is continued. In fact, this refinement helps to find the minimum with

a greater resolution accuracy. Now when this limiting condition of 0.1% is again achieved separately for each of the variable parameter then the optimization procedure is stopped and resulting optimum positions are noted. If two searches are performed with different initial step sizes, for example in one case it is taken equal to four times while in other it is kept twice of the pitch, it would be interesting to note the final results. If different results are obtained in these two searches, it may be linked to the existence of more than one local minima.

Now first in the following section, using a constant 0° fiber angle, support and force points are optimized. However the support points are restricted to move only along the specimen boundary.

6.6.3 Supports (restricted to specimen boundary) and force points

This section discusses the optimal positioning of support and force points for a given specimen shape and size such that best possible identification is achieved with minimum noise sensitivity. To be noted that a constant 0° fiber angle is used and support points are only allowed to be placed along the specimen boundary. Initially using Config-1 which serves as a starting point, reference criterion value, $g2$, is obtained along with individual sensitivity indices for respective rigidities. Now in a systematic manner defined before, all the variable parameters are moved and identification is achieved and criterion value $g2$ is determined such that optimum locations are found.

Optimization is achieved by using a step size equal to four times the pitch. Moreover, to check if there exist several local minima, additional results using a step size equivalent to twice the pitch is also presented. The two optimum configurations thus found are plotted in Fig 6.9 along with all the intermittent points before arriving at the final optimum configuration. It also plots the successive criteria values and it can be observed that at each new set of locations it decreases till it becomes stationary which represents the optimum combination of variable parameters. To give an idea of calculation time such a procedure approximately takes two to three hours on a standard Pentium4 computer with 1GB Ram. For the case of step size equal to four times the pitch, Table 6.14 records the global minimization criterion value, $g2$, and the respective individual sensitivity indices $\delta^{(\alpha)}$, whereas Table 6.15 records coordinates of the optimum support and force locations. Also, results for the case of step size equal to twice the pitch are presented in Table 6.16 and Table 6.17 respectively.

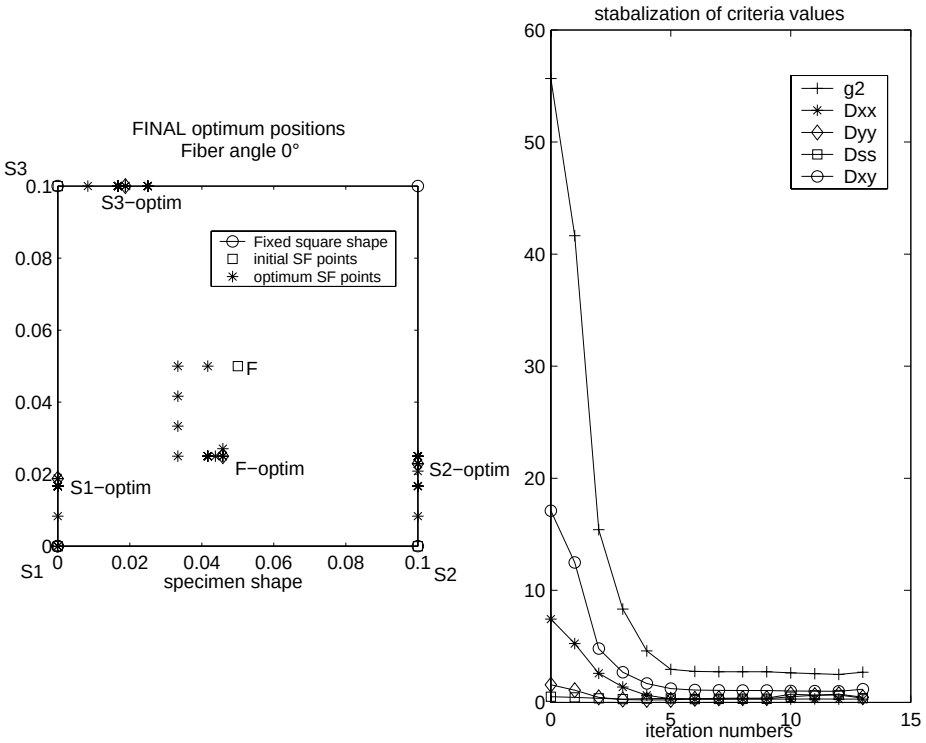

(a) Optimized Config-1, step is 4× pitch

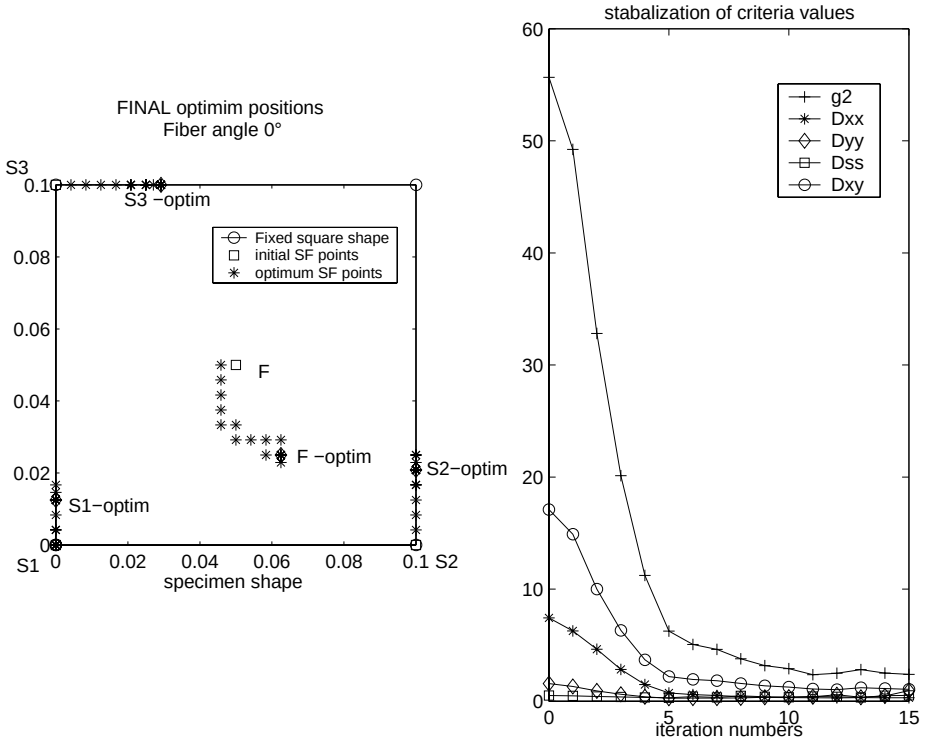

(b) Optimized Config-1, step is 2× pitch

Figure 6.9: Optimized Config-1 with optimum supports (restricted to plate boundary) and force points.

Sensitivity index values for an optimized Config-1					
Crt:	$g2$	$\delta^{(a)}$	$\delta^{(b)}$	$\delta^{(c)}$	$\delta^{(d)}$
final values	2.49	0.30	0.74	0.66	0.99
% reduction	*95.53*	*96.01*	*65.91*	*-32.31*	*94.19*

Table 6.14: Sensitivity index values for an optimized Config-1: optimum supports (restricted to specimen boundary) and force application point, step = $4 \times pitch$.

Optimum supports and force locations				
	S1	S2	S3	**F**
x (mm)	0	100	19	46
y (mm)	19	23	100	25

Table 6.15: Coordinates of optimum supports (restricted to specimen boundary) and force locations for the optimized Config-1, refer Table 6.14.

Sensitivity index values for an optimized Config-1					
Crt:	$g2$	$\delta^{(a)}$	$\delta^{(b)}$	$\delta^{(c)}$	$\delta^{(d)}$
final values	2.39	0.31	0.94	0.52	1.05
% reduction	*95.70*	*95.84*	*39.91*	*-3.51*	*93.85*

Table 6.16: Sensitivity index values for an optimized Config-1: optimum supports (restricted to specimen boundary) and force application point, step = $2 \times pitch$.

It is important to note that the use of two different initial step sizes resulted in two different final optimum combinations of variable parameters, hence it may be concluded that there exist local minimum for optimum combinations of the variable parameters. It is worth noting that the final $g2$ values in both the cases are in close vicinity, it may be said that the cost functions are probably very flat. In both cases it is important to note that the two lower supports ($S1$ and $S2$) and the force point fall more or less on a same horizontal level. In both cases all three support points are largely found at similar locations however the force is somewhat shifted to right side in the case when $2 \times$ pitch is used. However, an increase in sensitivity values for D_{ss} is observed in both the cases, but considering the fact that the reference initial value is itself small in comparison to others, this increase is not very significant. In future works, it would be interesting to use such an optimization scheme, e.g. genetic algorithm, which is capable of searching the unique global minimum solution.

Optimum supports and force locations				
	S1	S2	S3	**F**
x (mm)	0	100	30	63
y (mm)	13	21	100	25

Table 6.17: Coordinates of optimum supports (restricted to specimen boundary) and force locations for the optimized Config-1, refer Table 6.16.

Comparison of the criteria values and *% reduction* for the different optimization cases					
Cases	$g2$	$\delta^{(a)}$	$\delta^{(b)}$	$\delta^{(c)}$	$\delta^{(d)}$
Ref values Config-1	55.70 -	7.43 -	1.56 -	0.50 -	17.11 -
1. Angle	15.46 *72.24*	1.04 *85.98*	4.77 *-204.93*	0.55 *-9.38*	3.84 *77.55*
2. Width	21.51 *61.39*	1.57 *78.87*	6.52 *-317.15*	0.51 *-1.80*	5.06 *70.43*
3. Width + angle	12.17 *78.15*	0.78 *89.25*	3.83 *-144.80*	0.49 *1.30*	2.97 *82.63*
4. Force	6.68 *88.00*	0.55 *92.63*	2.15 *-37.24*	0.55 *-9.58*	2.24 *86.90*
5. Support (restricted) + force	2.49 *95.53*	0.30 *96.01*	0.74 *65.91*	0.66 *-32.31*	0.99 *94.91*

Table 6.18: A successive comparison of the reference global ($g2$) and individual sensitivity criteria ($\delta^{(\alpha)}$) for the different optimization cases as listed in Section 6.1.

From the comparative study of the results recorded in Table 6.18, it is observed that with optimized support and force application points, a significant reduction is achieved in noise minimization criterion $g2$ and respective individual sensitivity indices, with an exception in the case of D_{ss}.

Now the following section discusses optimization when fiber angle is also considered as a variable parameter. The idea is to study if this additional freedom results in further decrease in the minimization criterion values.

6.6.4 Supports (restricted to specimen boundary), force point and fiber angle

This section discusses the effect of adding an extra variable parameter i.e, fiber angle for the case studied in Section 6.6.3. The idea is to study its effect on the minimization criterion value $g2$ and respectively on the individual sensitivity indices for each rigidity. Using a step size equal to 4 $\times$ pitch, for each of the fiber angle varying from 0° to 180° with 5° regular increments final optimum supports (restricted to specimen boundary only) and force application points are found. At final optimized positions using increasing fiber angles, corresponding criteria values, $g2$ are noted along with sensitivity indices for individual rigidities. These minimum criteria values $g2$ with increasing fiber angles are plotted in Fig 6.10.

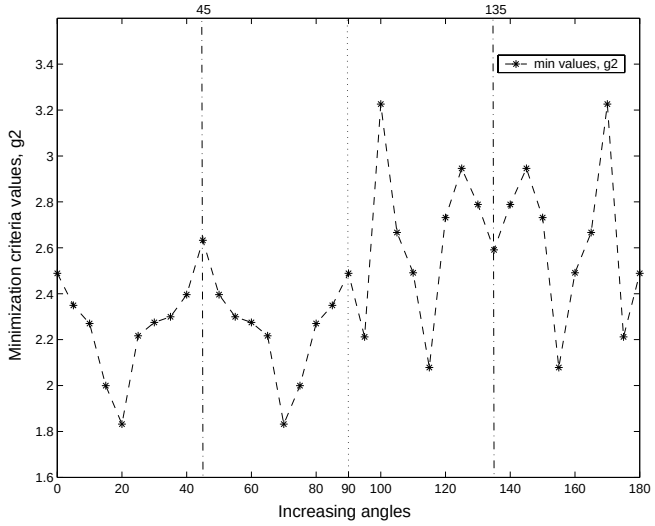

Figure 6.10: Config-1: Search of optimum fiber angle with optimized supports (restricted to specimen boundary) and force point

From Fig 6.10, it may be observed that for the two different fiber angles, 20° and 70°, same minimum $g2$ value is obtained. Also it is interesting to note the two symmetry axes respectively at 45° and 135°. By noting the variation of $g2$ values from one angle to another, it is observed that it varies within a very small range. Therefore, it may be said that the effect of angle optimization is not very significant. Fig 6.11 plots the final optimum configurations, showing optimized support points (restricted to specimen boundary) and force application point for the two optimum fiber angles, 20° and 70° respectively. These two configurations are in fact mirror images with respect to a symmetrical axis at 45°.

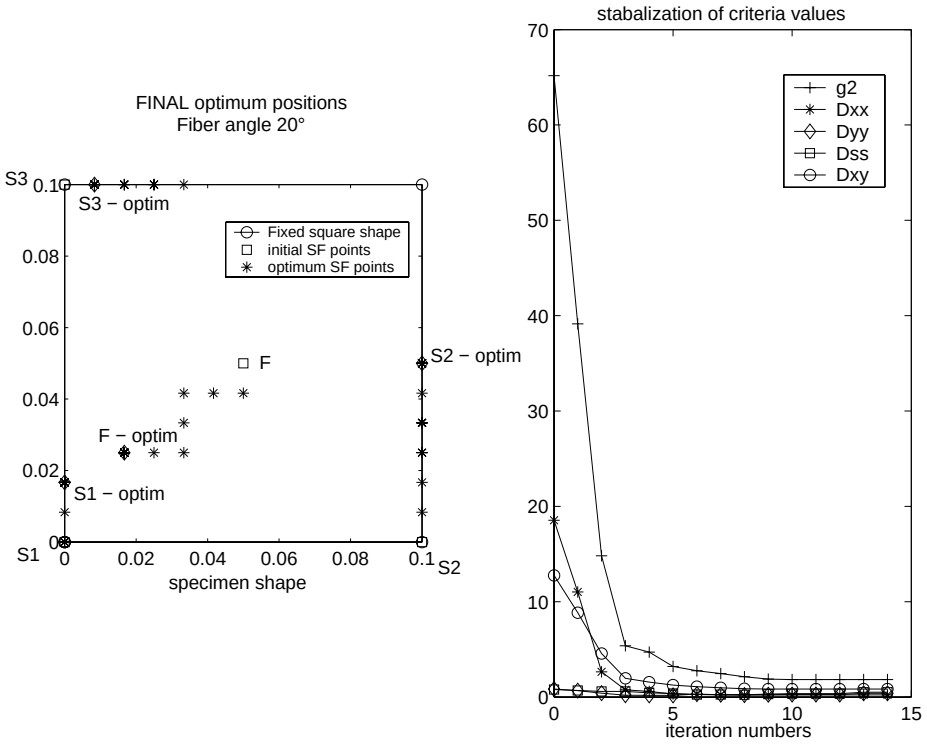

(a) Optimized Config-1 using 20° fiber angle

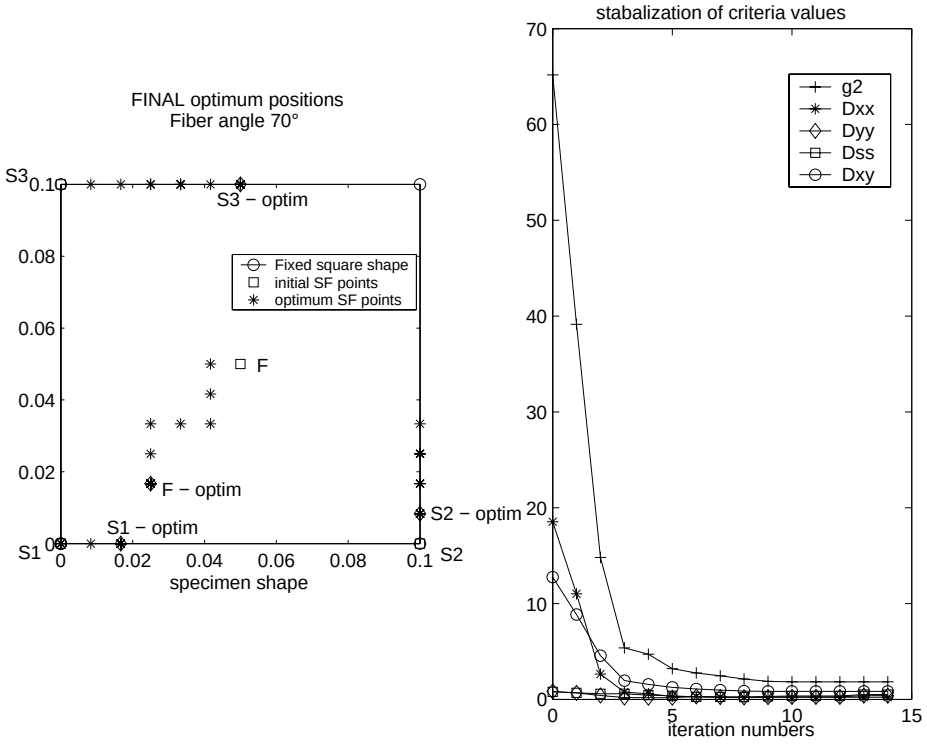

(b) Optimized Config-1 using 70° fiber angle

Figure 6.11: Optimized Config-1 with two optimum fiber angles resulting in similar criterion values, $g2$; optimum supports (restricted to specimen boundary) and force points.

The criteria values obtained for these optimum configurations are presented in Table 6.19 whereas the Table 6.20 records the coordinates of supports and force points, for the optimum configurations found with 20° and 70° fiber angle respectively.

Sensitivity index values for an optimized Config-1 Identical values for the two optimum fiber angles, 20° and 70°					
Crt:	$g2$	$\delta^{(a)}$	$\delta^{(b)}$	$\delta^{(c)}$	$\delta^{(d)}$
final values	1.83	0.22	0.39	0.50	0.83
% reduction	*96.71*	*96.99*	*75.12*	*-0.73*	*95.12*

Table 6.19: Optimized Config-1: Similar sensitivity index values for two different optimum fiber angles, 20° and 70°, resulting in optimum supports (restricted to specimen boundary) and force application point, step = $4 \times pitch$.

Optimum supports and force locations								
	for 20° optimum fiber angle				for 70° optimum fiber angle			
	S1	S2	S3	**F**	S1	S2	S3	**F**
x (mm)	0	100	8	17	17	100	50	25
y (mm)	17	50	100	25	0	8	100	17

Table 6.20: Optimized Config-1: Coordinates of optimum supports (restricted to specimen boundary) and force locations for the the two optimum fiber angles 20° and 70°, refer Table 6.19.

By comparing the results quoted in Table 6.21, it may be observed that the sensitivity values are slightly lessened overall, however a significant improvement is achieved for $\delta^{(c)}$ which is the sensitivity index corresponding to rigidity D_{ss}. Now it is only 0.73% in excess to the reference value as compared to 32.31% earlier. Finally, it may be said that the additional variable parameter of fiber angle results in further decrease of sensitivity indices but the overall influence remains insignificant.

Now the following section discusses optimization when an additional freedom is given to the system by allowing support points to be placed within the plate. Initially 0° fiber angle is used for this study.

Comparison of the criteria values and *% reduction* for the different optimization cases					
Cases	$g2$	$\delta^{(a)}$	$\delta^{(b)}$	$\delta^{(c)}$	$\delta^{(d)}$
Ref values Config-1	55.70 -	7.43 -	1.56 -	0.50 -	17.11 -
1. Angle	15.46 *72.24*	1.04 *85.98*	4.77 *-204.93*	0.55 *-9.38*	3.84 *77.55*
2. Width	21.51 *61.39*	1.57 *78.87*	6.52 *-317.15*	0.51 *-1.80*	5.06 *70.43*
3. Width + angle	12.17 *78.15*	0.78 *89.25*	3.83 *-144.80*	0.49 *1.30*	2.97 *82.63*
4. Force	6.68 *88.00*	0.55 *92.63*	2.15 *-37.24*	0.55 *-9.58*	2.24 *86.90*
5. Support (restricted) + force	2.49 *95.53*	0.30 *96.01*	0.74 *65.91*	0.66 *-32.31*	0.99 *94.91*
6. Support (restricted) + force + angle	1.83 *96.71*	0.22 *96.99*	0.39 *75.12*	0.50 *-0.73*	0.83 *95.12*

Table 6.21: A successive comparison of the reference global ($g2$) and individual sensitivity criteria ($\delta^{(\alpha)}$) for the different optimization cases as listed in Section 6.1.

6.6.5 Supports and force points

This section now discusses the effect of adding an extra freedom to the case studied earlier in Section 6.6.3. As before, Config-1 with 0° fiber angle serves as starting point, except that support points are now allowed to be placed within the specimen area contrary to the earlier case when they were restricted only to the specimen boundary. Optimization is performed by using a step size equal to 4 × pitch and the resulting optimum configuration is plotted in Fig 6.12. Table 6.22 records the global minimization criterion value, $g2$, and the respective individual sensitivity indices $\delta^{(\alpha)}$, whereas Table 6.23 records coordinates of the optimum supports and force locations.

Sensitivity index values for an optimized Config-1					
Crt:	$g2$	$\delta^{(a)}$	$\delta^{(b)}$	$\delta^{(c)}$	$\delta^{(d)}$
final values	1.69	0.24	0.25	0.26	0.80
% reduction	*96.96*	*96.82*	*84.22*	*48.04*	*95.33*

Table 6.22: Sensitivity index values for an optimized Config-1: optimum supports and force application point, step = 4 × *pitch*.

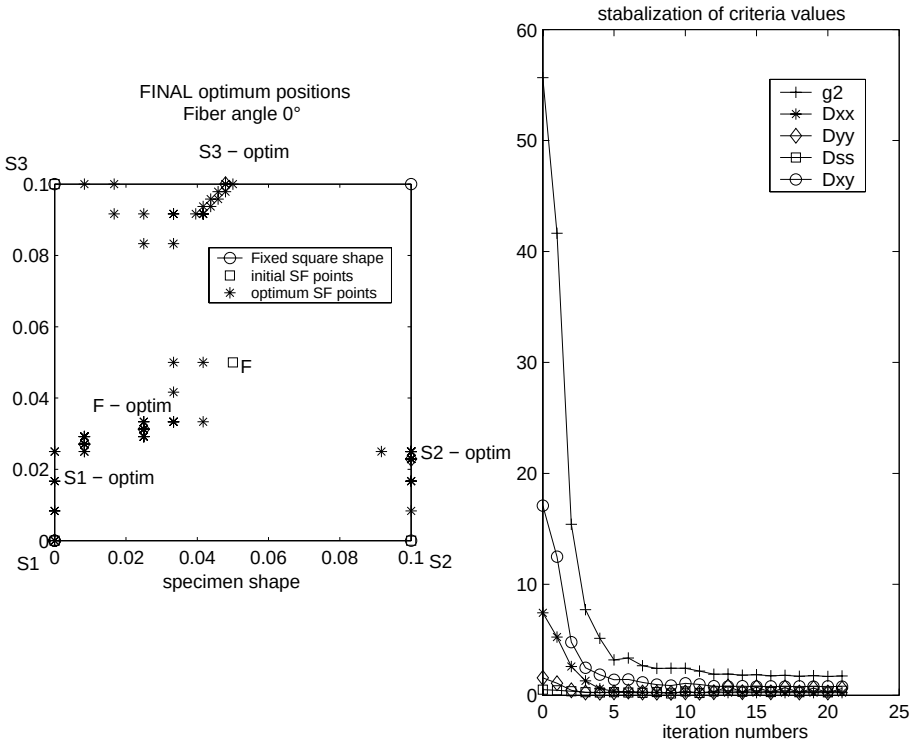

Figure 6.12: Optimized Config-1 with optimum supports and force points.

Optimum supports and force locations				
	S1	S2	S3	**F**
x (mm)	8	100	48	25
y (mm)	27	23	100	31

Table 6.23: Coordinates of optimum support and force locations for the optimized Config-1, refer Table 6.22.

A comparison of results quoted in Table 6.24 shows an overall improvement particularly with reference to case no. 5. Specially for $\delta^{(c)}$, which is the individual sensitivity index for D_{ss}, a significant improvement is noted. Now it is reduced by 48% whereas it was earlier found to be increased by 32.31% in comparison to the reference value. Similarly for $\delta^{(b)}$ representing D_{yy}, a 84.22% reduction is observed as compared to earlier 65.91%. Also, the final positions are consistent with the fact that the three supports are found far away from each other on the extremities of the specimen thus resulting in larger deflections for a given load.

Now the following section discusses the effect of setting fiber angle also as a variable parameter for the system studied above.

Comparison of the criteria values and *% reduction* for the different optimization cases					
Cases	$g2$	$\delta^{(a)}$	$\delta^{(b)}$	$\delta^{(c)}$	$\delta^{(d)}$
Ref values Config-1	55.70 -	7.43 -	1.56 -	0.50 -	17.11 -
1. Angle	15.46 *72.24*	1.04 *85.98*	4.77 *-204.93*	0.55 *-9.38*	3.84 *77.55*
2. Width	21.51 *61.39*	1.57 *78.87*	6.52 *-317.15*	0.51 *-1.80*	5.06 *70.43*
3. Width + angle	12.17 *78.15*	0.78 *89.25*	3.83 *-144.80*	0.49 *1.30*	2.97 *82.63*
4. Force	6.68 *88.00*	0.55 *92.63*	2.15 *-37.24*	0.55 *-9.58*	2.24 *86.90*
5. Support (restricted) + force	2.49 *95.53*	0.30 *96.01*	0.74 *65.91*	0.66 *-32.31*	0.99 *94.91*
6. Support (restricted) + force + angle	1.83 *96.71*	0.22 *96.99*	0.39 *75.12*	0.50 *-0.73*	0.83 *95.12*
7. Support + force	1.69 *96.96*	0.24 *96.82*	0.25 *84.22*	0.26 *48.04*	0.80 *95.33*

Table 6.24: A successive comparison of the reference global ($g2$) and individual sensitivity criteria ($\delta^{(\alpha)}$) for the different optimization cases as listed in Section 6.1.

6.6.6 Supports, force point and fiber angle

For the present study, same system as in Section 6.6.5 is used with the only addition that the fiber angle is now also treated as a variable parameter. The effect of this additional parameter on the final optimized configuration and corresponding sensitivity indices is discussed here. Using initial step size equal to 4 $\times$ pitch, final optimum configurations are obtained for the fiber angles varying from 0° to 180°. For each angle used the resulting minimized final criterion value $g2$ is noted along with respective individual sensitivity indices. Fig 6.14 plots these final criterion values, $g2$, corresponding to the final optimized configuration achieved at each increasing angle. In Fig 6.14, it is interesting to observe a pattern as before in Fig 6.10. Here also, a same minimum $g2$ value is obtained for two different fiber angles 5° and 85°, in addition to the existence of two symmetry axes respectively at 45° and 135°. Fig 6.13 plots the final optimum configurations, showing optimized support points and force application point for these two optimum fiber angles. Table 6.25 records the criteria values corresponding to the final optimized configurations.

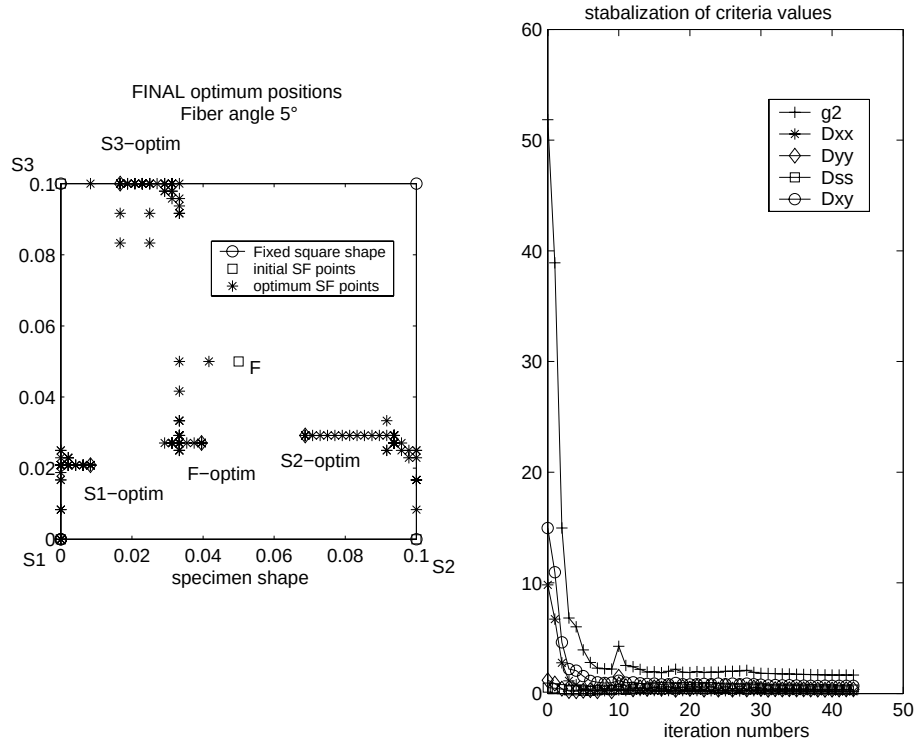

(a) Optimized Config-1 using 5° fiber angle

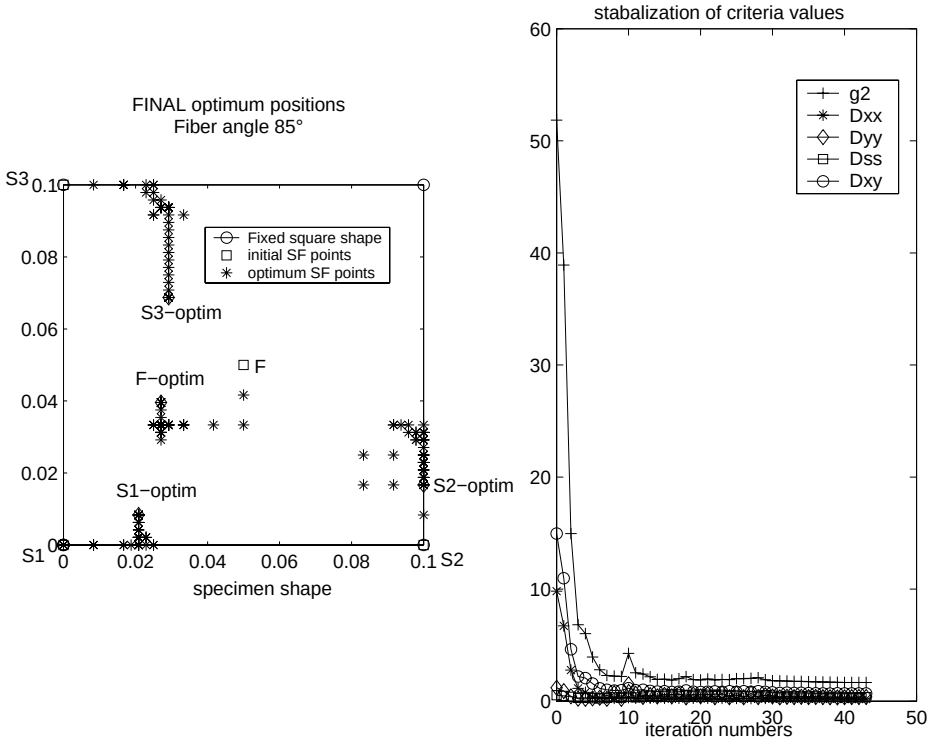

(b) Optimized Config-1 using 85° fiber angle

Figure 6.13: Optimized Config-1 with two optimum fiber angles resulting in similar criterion values, $g2$; optimum supports and force points.

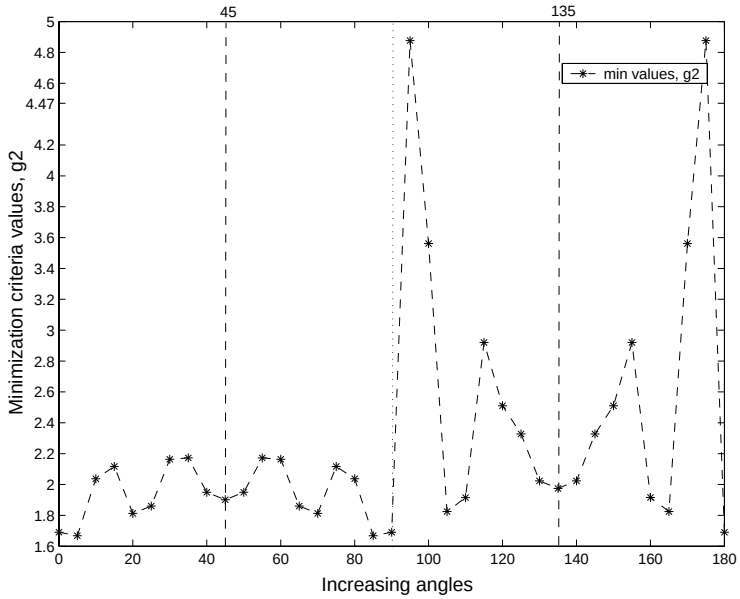

Figure 6.14: Config-1: Search of optimum fiber angle with optimized supports and force point

These two configurations are in fact mirror images with respect to a symmetry axis at 45°. Table 6.26 records the supports and force points coordinates for the two optimum configurations found with 5° and 85° fiber angle respectively.

Sensitivity index values for an optimized Config-1 Identical values for the two optimum fiber angles, 5° and 85°					
Crt:	$g2$	$\delta^{(a)}$	$\delta^{(b)}$	$\delta^{(c)}$	$\delta^{(d)}$
final values	1.67	0.19	0.37	0.36	0.69
% reduction	*97.00*	*97.37*	*76.10*	*27.58*	*95.97*

Table 6.25: Optimized Config-1: Similar sensitivity index values for two different optimum fiber angles, 5° and 85°, resulting in optimum supports and force application point, step $= 4 \times pitch$.

To observe the effect of using fiber angle as a variable parameter, above results are compared to those of Section 6.6.5. The comparative results of all the cases studied are recorded in Table 6.27. Upon comparing the latest results especially with reference to case 7, only a very slight improvement is observed in criterion value, $g2$, from 96.96% to 97.00%. Although, the use of an additional variable parameter is justified though the gain is very minimal and insignificant. For respective individual rigidities marginal improvement is also observed for rigidities D_{xx} and D_{xy}, however

Optimum supports and force locations								
	for 5° optimum fiber angle				for 85° optimum fiber angle			
	S1	S2	S3	**F**	S1	S2	S3	**F**
x (mm)	8	69	17	40	21	100	29	27
y (mm)	21	29	100	27	8	17	69	40

Table 6.26: Optimized Config-1: Coordinates of optimum support and force locations for the the two optimum fiber angles 5° and 85°, refer Table 6.25.

Comparison of the criteria values and *% reduction* for the different optimization cases					
Cases	$g2$	$\delta^{(a)}$	$\delta^{(b)}$	$\delta^{(c)}$	$\delta^{(d)}$
Ref values Config-1	55.70 -	7.43 -	1.56 -	0.50 -	17.11 -
1. Angle	15.46 *72.24*	1.04 *85.98*	4.77 *-204.93*	0.55 *-9.38*	3.84 *77.55*
2. Width	21.51 *61.39*	1.57 *78.87*	6.52 *-317.15*	0.51 *-1.80*	5.06 *70.43*
3. Width + angle	12.17 *78.15*	0.78 *89.25*	3.83 *-144.80*	0.49 *1.30*	2.97 *82.63*
4. Force	6.68 *88.00*	0.55 *92.63*	2.15 *-37.24*	0.55 *-9.58*	2.24 *86.90*
5. Support (restricted) + force	2.49 *95.53*	0.30 *96.01*	0.74 *65.91*	0.66 *-32.31*	0.99 *94.91*
6. Support (restricted) + force + angle	1.83 *96.71*	0.22 *96.99*	0.39 *75.12*	0.50 *-0.73*	0.83 *95.12*
7. Support + force	1.69 *96.96*	0.24 *96.82*	0.25 *84.22*	0.26 *48.04*	0.80 *95.33*
8. Support + force + angle	1.67 *97.00*	0.19 *97.37*	0.37 *76.10*	0.36 *27.58*	0.69 *95.97*

Table 6.27: A successive comparison of the reference global ($g2$) and individual sensitivity criteria ($\delta^{(\alpha)}$) for the different optimization cases as listed in Section 6.1.

results for D_{yy} and D_{ss} are not as good as before. It may be explained by recalling that the criterion $g2$ considers the relative differences of the individual sensitivities. Due to this a minimum $g2$ value represents a more balanced combination of individual sensitivities. However, there may be situations where individually higher criterion values result in a minimum $g2$ value, such as in the present case. But, considering that these individual sensitivity values are still significantly low, these are acceptable.

Finally, it can be argued that there is no significant gain by using fiber angle as a variable parameter to the case when it was fixed to 0°, additionally it is found less efficient for individual rigidities D_{yy} and D_{ss}, hence the earlier configuration with fixed fiber angle at 0° is more efficient and is most capable to identify all the rigidities with least noise sensitivity.

Now the following section discusses the effect on noise sensitivity criterion when specimen shape is also optimized along with location of supports and force application points.

6.7 Optimization of specimen shape, supports and force point

This section now discusses the shape optimization along with supports and force application points with fixed fiber angle at 0°. For the purpose of shape optimization, specimen geometry is defined by a spline passing through 8 interpolation points as shown in Fig 6.15.

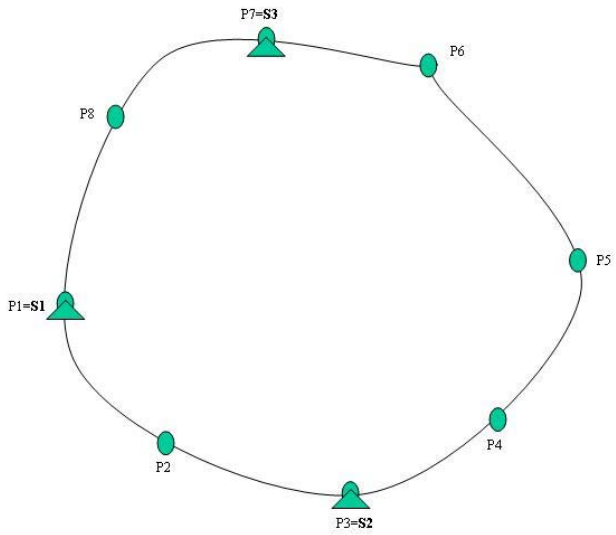

Figure 6.15: An irregular shaped specimen formed by a spline passing through eight points.

It is important to note here that in the present study support points are restricted to specimen boundary. Hence the required number of supports are attributed to corresponding interpolation points at respective positions. Thus among the total

eight interpolation points, three points are used to define both the shape and support locations whereas the remaining five points are solely defining the specimen shape. Before discussing the specimen shape optimization, following section first describes discretization of an irregular shaped specimen.

6.7.1 Discretization of an irregular shape specimen

6.7.1.1 Introduction

It is important to note that up till now the specimen represented a regular shape and hence during simulation using Ansys a regular meshing was easily possible. But in the case when shape points are allowed to move, an irregular shaped specimen is likely to be obtained whose regular meshing is not possible using functions available in Ansys package. To overcome this difficulty and to obtain a regular mesh for an irregular shaped specimen, a special discretization procedure developed by Mathias [83, 1] during his PhD work regarding composite patches is adapted here. The discretization procedure is briefly recalled blow.

6.7.1.2 Procedure

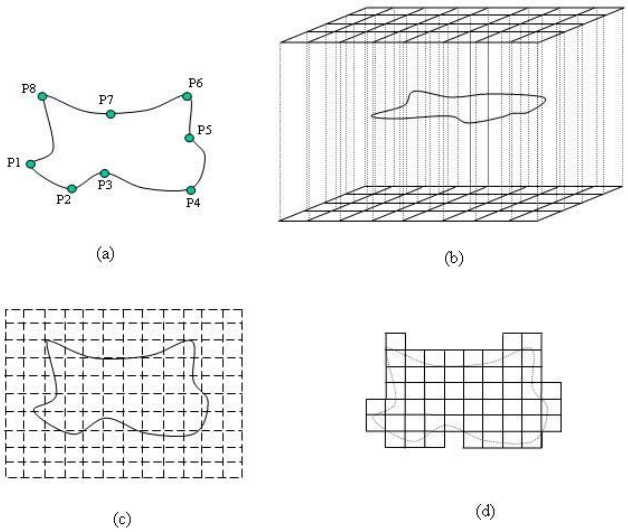

Figure 6.16: An illustration of discretization procedure [1].

The procedure is illustrated in Fig 6.16 and is as follows:

- an irregular shaped surface defined by the above mentioned eight interpolation points is created by using the Ansys SPLINE function, Fig 6.16(a).

- two square plates, called here *discretizing plates* are created. These are placed exactly on top of each other with a predefined separating distance in between. On these plates a required regular mesh density can be easily imposed. Now the irregular surface which is needed to be meshed in a regular pattern is placed in between these two discretizing plates, Fig 6.16(b).

- the regular mesh imposed on these discretizing plates is now projected on this irregular surface, Fig 6.16(c).

- finally all the discrete mesh areas found enclosed within the spline are retained thus resulting in a discretized irregular shape specimen with a regular mesh pattern.

However it is worth mentioning that this discretizing procedure is comparatively lengthy and takes approximately 3 minutes compared to normal meshing operation which hardly takes a couple of seconds. Thus the total simulation time for an irregular shaped specimen is considerably greater than that of a regular shaped specimen.

6.7.1.3 Limitations

It is important to note that the boundary of discretizing plates serves to limit the irregular shaped surface as it is not allowed to pass this limit. Hence if an interpolation point reaches this limit, it is stopped and cannot proceed further outside the discretizing plate dimension. In fact this is important in restricting the evolving shape not to be elongated only in one direction. As otherwise it will result in a overly elongated shape which is not very suitable for experimental purposes especially with reference to the use of CCD camera, as already discussed in Section 6.3.

Additionally, it is important to discuss here an inherent procedural limitation when two interpolation points come very close to each other. This results in a crossed spline with a loop and the further advancement of the simulation routine is programmed to be terminated at this point. This situation represents an end to the ongoing search for optimization. Though by using a different step size afresh or by changing the initial point locations, this situation may be avoided due to the presence of local minima as observed in earlier results.

6.7.1.4 Definition of starting reference configuration

For the purpose of present shape optimization, a configuration similar to Config-1 in terms of supports and load locations serves as a starting point. However considering the significant computation time especially to obtain a regular discretized

surface, the specimen size in Config-1 is reduced by half to get $0.05m \times 0.05m$ square specimen plate. Fig 6.17 plots the shape of this reduced specimen size using a continuous spline passing through the eight interpolation points. Worth mentioning that this size reduction is already taken care in the criterion value when it is normalized with respect to specimen area, refer Eq. (5.1). Thus, the criterion values resulting from this reduced specimen shape are therefore directly comparable to the respective values for the reference Config-1.

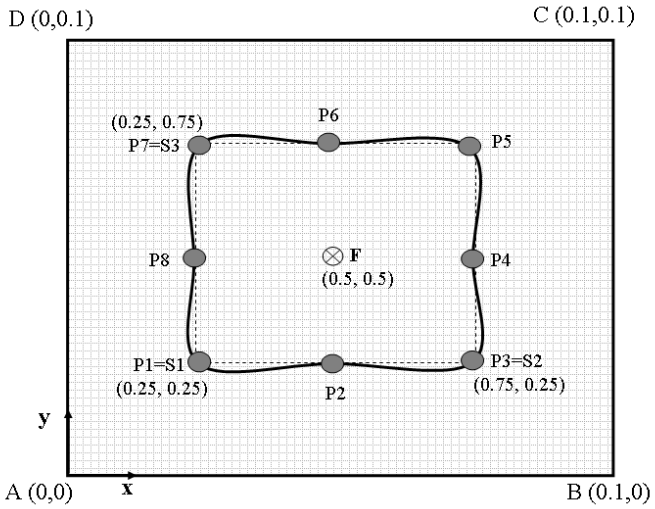

Figure 6.17: Figure to illustrate starting configuration to be used for shape optimization.

It is important to recall that the boundary of the discretizing plates, described earlier in Section 6.7.1.2, serves to limit the evolving shape not to be elongated only in one direction. For this purpose, if an interpolation point reaches this limit, it is stopped and cannot proceed further outside the discretizing plate dimension. The present example uses the two square discretizing plates of $0.1m \times 0.1m$ such that the starting close to square specimen shape may well be accommodated within these plates. This leaves sufficient space for the interpolation points to look around in search of optimal location without coming closer to the limiting zone too early.

Now the following sections discuss two optimization examples of Config-1 using constant 0° fiber angle, initially when the force application point and three interpolation points defining supports are kept fixed while the remaining five interpolation points defining plate geometry are free to move and are optimized. Later a complete optimization of all the eight interpolation points and force application point is presented. For these examples a real mesh size of 60×60 with step size equal to $3\times$ pitch is used. This in fact gives more flexibility to search around for optimum locations before coming too close to the limiting discretizing plate and also to each

other, thus resulting in a crossed spline where the search stops.

The following section now discusses a shape optimization case with fixed supports and force application points.

6.7.2 Optimization of specimen shape using fixed supports and force points

This section presents shape optimization of Config-1. Initially in this section the shape is optimized by using as variable parameters only the five interpolation points purely defining the specimen geometry. The remaining three interpolation points which also define the three simple supports and the force application point are fixed constant. Same optimization procedure described before in Section 6.6 is used to find a new successive location for each of the interpolation points to define a new geometry of specimen shape till a final optimized shape is achieved. Fig 6.18 plots the final optimum configuration, showing optimized points which define the specimen geometry with fixed supports and force application points. It also plots the final optimum shape formed by a spline passing through these eight interpolations points along with its discretized shape. Table 6.28 presents the final results obtained for such an optimization. It is important to note that due to the discritizing procedure, it was rather lengthy operation and took about 9 hrs to arrive at final optimum shape on a standard Pentium4 computer with 1GB Ram.

Sensitivity index values for an optimized Config-1					
Crt:	$g2$	$\delta^{(a)}$	$\delta^{(b)}$	$\delta^{(c)}$	$\delta^{(d)}$
final values	15.95	1.83	0.59	0.27	5.17
% reduction	*68.58*	*74.91*	*59.12*	*38.49*	*66.42*

Table 6.28: Shape optimization Config-1: Sensitivity index values for optimized shape using fixed supports and force application point.

By comparing with the results recorded in Table 6.29, it is observed that the final shape obtained using fixed supports and force application point is not very interesting in terms of percentage reduction in noise sensitivity criterion value, $g2$ and also for the individual rigidities. Much greater reductions were observed in earlier sections for the cases when shape was fixed and only supports and force points were optimized as summarized in the Table 6.29. This may be attributed to the fact that the support and force application points in the present case were kept fixed. Also it would be interesting to compare with the following case where these are optimized also.

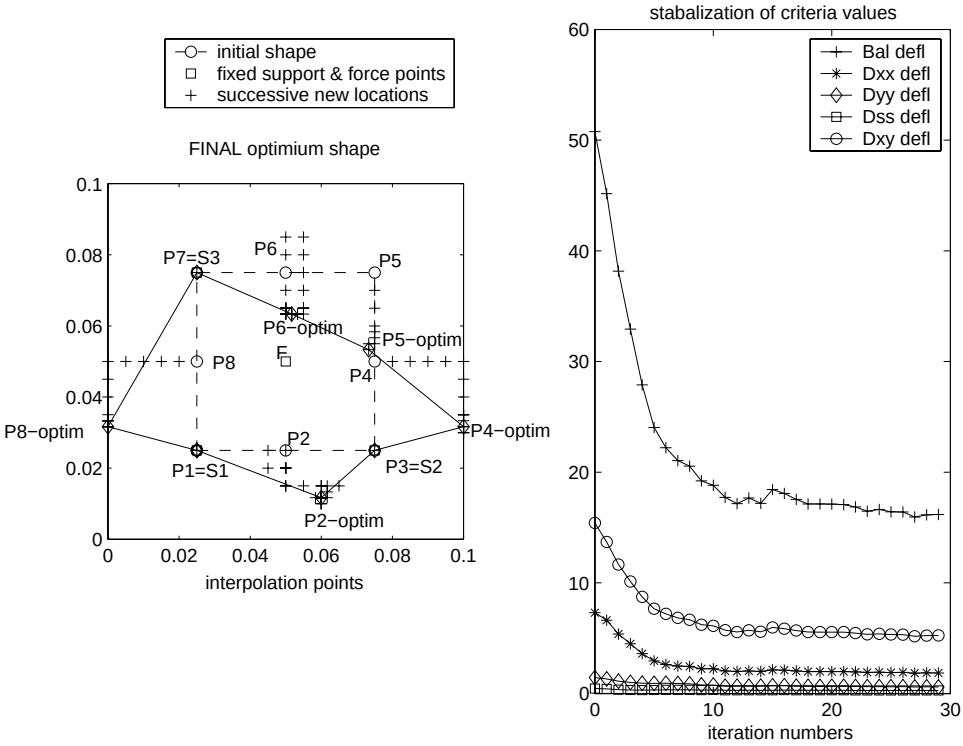

(a) Shape optimization Config-1: fixed supports and force application point.

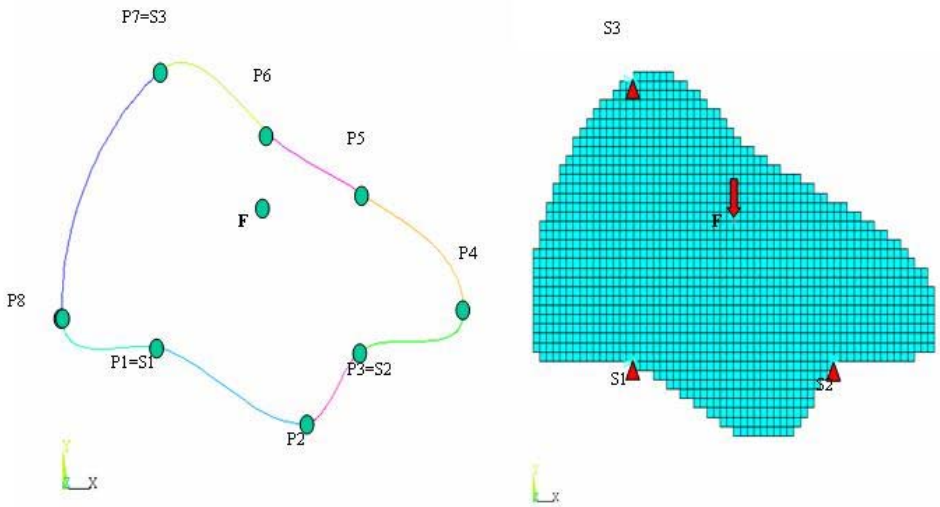

(b) Shape optimization Config-1: Spline passing through eight interpolation points and its discretization.

Figure 6.18: Shape optimization of Config-1 using fixed supports and force application point.

Comparison of the criteria values and *% reduction* for the different optimization cases					
Cases	$g2$	$\delta^{(a)}$	$\delta^{(b)}$	$\delta^{(c)}$	$\delta^{(d)}$
Ref values Config-1	55.70 -	7.43 -	1.56 -	0.50 -	17.11 -
1. Angle	15.46 *72.24*	1.04 *85.98*	4.77 *-204.93*	0.55 *-9.38*	3.84 *77.55*
2. Width	21.51 *61.39*	1.57 *78.87*	6.52 *-317.15*	0.51 *-1.80*	5.06 *70.43*
3. Width + angle	12.17 *78.15*	0.78 *89.25*	3.83 *-144.80*	0.49 *1.30*	2.97 *82.63*
4. Force	6.68 *88.00*	0.55 *92.63*	2.15 *-37.24*	0.55 *-9.58*	2.24 *86.90*
5. Support (restricted) + force	2.49 *95.53*	0.30 *96.01*	0.74 *65.91*	0.66 *-32.31*	0.99 *94.91*
6. Support (restricted) + force + angle	1.83 *96.71*	0.22 *96.99*	0.39 *75.12*	0.50 *-0.73*	0.83 *95.12*
7. Support + force	1.69 *96.96*	0.24 *96.82*	0.25 *84.22*	0.26 *48.04*	0.80 *95.33*
8. Support + force + angle	1.67 *97.00*	0.19 *97.37*	0.37 *76.10*	0.36 *27.58*	0.69 *95.97*
9. Shape	15.95 *68.58*	1.83 *74.91*	0.59 *59.12*	0.27 *38.49*	5.17 *66.42*

Table 6.29: A successive comparison of the reference global ($g2$) and individual sensitivity criteria ($\delta^{(\alpha)}$) for the different optimization cases as listed in Section 6.1.

However, on account of the observed results, it may be said that the effect of only shape shape optimization is not very interesting in terms of reduced noise sensitivity. The following section now presents an example of shape optimization where all the eight interpolation points defining specimen geometry and force application is optimized. The idea is to study the improvements in terms of noise sensitivity reduction.

6.7.3 Complete shape optimization of a specimen

This section finally presents a complete shape optimization of Config-1 with 0° fiber angle, where all the eight interpolation points defining specimen shape are treated as variable parameters in addition to a ninth variable that is force application point. Remembering here that the three supports are attached to respective three interpolation points and are thus restricted on the specimen boundary.

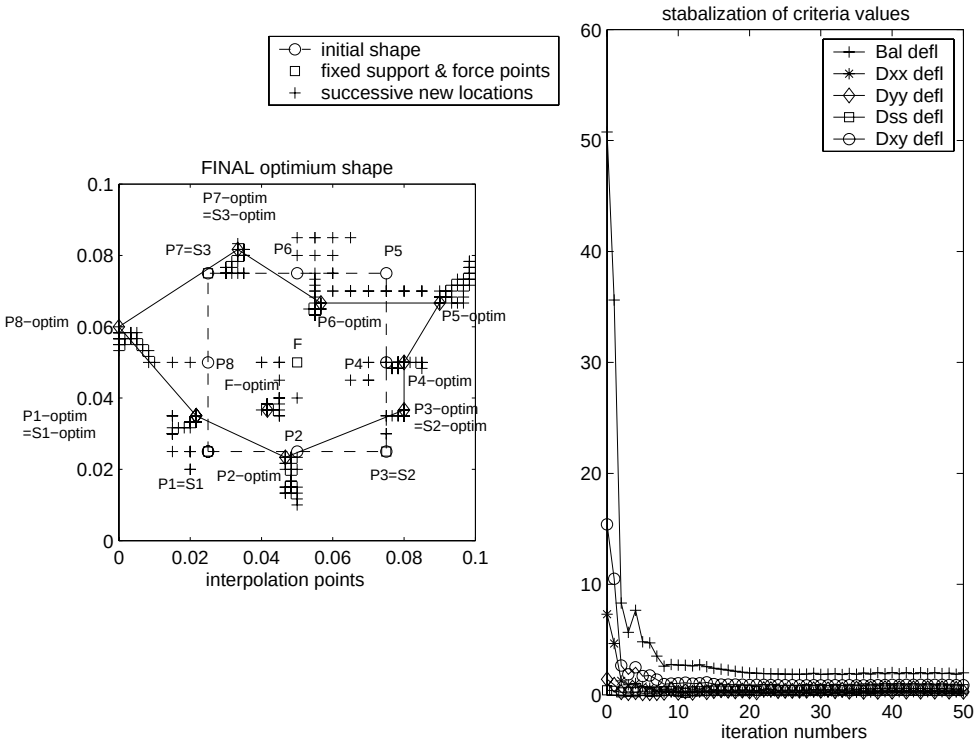

(a) Complete shape optimization of Config-1.

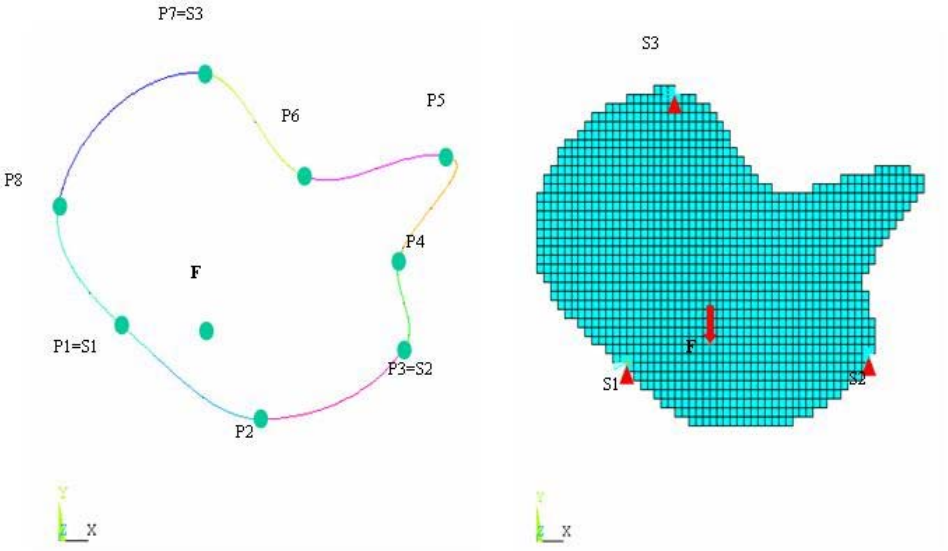

(b) Complete shape optimization Config-1: Spline passing through eight interpolation points and its discretization.

Figure 6.19: Complete shape optimization of Config-1 with optimized eight interpolation points and force application point.

Sensitivity index values for an optimized Config-1					
Crt:	$g2$	$\delta^{(a)}$	$\delta^{(b)}$	$\delta^{(c)}$	$\delta^{(d)}$
final values	1.89	0.29	0.57	0.57	0.90
% reduction	*96.27*	*96.04*	*60.34*	*-29.31*	*94.15*

Table 6.30: Complete shape optimization Config-1: Sensitivity index values for optimized shape.

Similar procedure as before is used to find a successive optimized shape staring from Config-1 such that a final optimized shape is identified. At this final shape either the criterion value remains unchanged or the difference is less than or equal to 0.1% to precedent one. Fig 6.19 plots the final optimum configuration, showing the optimized eight interpolation points which define the specimen geometry and the force application point. It also plots, the final optimum shape formed by a spline passing through these eight optimized interpolations points along with its discretized shape. Table 6.30 presents the final results obtained for such an optimization. It is worth noting that this illustration took 23hrs to arrive at final optimum shape.

Now for the present case of complete shape optimization a considerable reduction in criterion values, $g2$ is observed in comparison to the results quoted in Table 6.31 especially for the case no.9, where support and force points were kept fixed. However no improvement is noted when compared to the earlier cases, for instance, case no.6 and case no.7 where shape was fixed as to that of Config-1 and only supports and force points and additionally the fiber angle were optimized respectively. Sensitivity results of $\delta^{(c)}$ representing D_{ss} is now found to be increased by 29.31% whereas for above mentioned cases they were significantly reduced by 48.04% and 27.58%.

Though this shape optimization may be extended further by setting fiber angle also as a variable parameter in addition to separately defining interpolation and support points contrary to present case when they represent only one variable parameter. These enrichments are not undertaken in the present work. However, considering the increased level of simulation complexities due to an irregular shape and the required processing time, it is interesting to discuss the actual advantage and eventual benefit in terms of reduced sensitivity to noise for an optimized specimen shape. As noted above there is no significant gain or improvement hence use of such an optimized shape may not be justified. Also, most importantly from practical point of view it is very difficult to obtain such a special shaped specimen by cutting a composite plate to a given irregular shape. Finally it may be argued that use of a fixed shape square specimen as Config-1 with optimized supports and force application points is more preferable.

Comparison of the criteria values and *% reduction* for the different optimization cases					
Cases	$g2$	$\delta^{(a)}$	$\delta^{(b)}$	$\delta^{(c)}$	$\delta^{(d)}$
Ref values Config-1	55.70 -	7.43 -	1.56 -	0.50 -	17.11 -
1. Angle	15.46 *72.24*	1.04 *85.98*	4.77 *-204.93*	0.55 *-9.38*	3.84 *77.55*
2. Width	21.51 *61.39*	1.57 *78.87*	6.52 *-317.15*	0.51 *-1.80*	5.06 *70.43*
3. Width + angle	12.17 *78.15*	0.78 *89.25*	3.83 *-144.80*	0.49 *1.30*	2.97 *82.63*
4. Force	6.68 *88.00*	0.55 *92.63*	2.15 *-37.24*	0.55 *-9.58*	2.24 *86.90*
5. Support (restricted) + force	2.49 *95.53*	0.30 *96.01*	0.74 *65.91*	0.66 *-32.31*	0.99 *94.91*
6. Support (restricted) + force + angle	1.83 *96.71*	0.22 *96.99*	0.39 *75.12*	0.50 *-0.73*	0.83 *95.12*
7. Support + force	1.69 *96.96*	0.24 *96.82*	0.25 *84.22*	0.26 *48.04*	0.80 *95.33*
8. Support + force + angle	1.67 *97.00*	0.19 *97.37*	0.37 *76.10*	0.36 *27.58*	0.69 *95.97*
9. Shape	15.95 *68.58*	1.83 *74.91*	0.59 *59.12*	0.27 *38.49*	5.17 *66.42*
10. Shape + support + force	1.89 *96.27*	0.29 *96.04*	0.57 *60.34*	0.57 *-29.31*	0.90 *94.15*

Table 6.31: A successive comparison of the reference global ($g2$) and individual sensitivity criteria ($\delta^{(\alpha)}$) for the different optimization cases as listed in Section 6.1.

6.8 Effect of material

In order to study the effect of using a different material on the optimization result, an illustrative example using a carbon-epoxy composite with typical elastic constants (quoted earlier in Section 5.5) is presented here. For this purpose, an optimization case similar to case no. 5, discussed earlier in Section 6.6.3 is studied. It is selected on account of the observed significant % reductions in addition to the comparative simplicity from other other cases. The idea is to study the effect of using a different material on the optimized supports (restricted along the specimen boundary) and force locations using a constant 0° fiber angle. For an initial step size equal to four times the pitch, Fig 6.20 plots the final optimum configuration. It is compared to the corresponding case of a glass-epoxy plate presented in Fig 6.9(a).

From the respective figures for the two different materials, it is interesting to

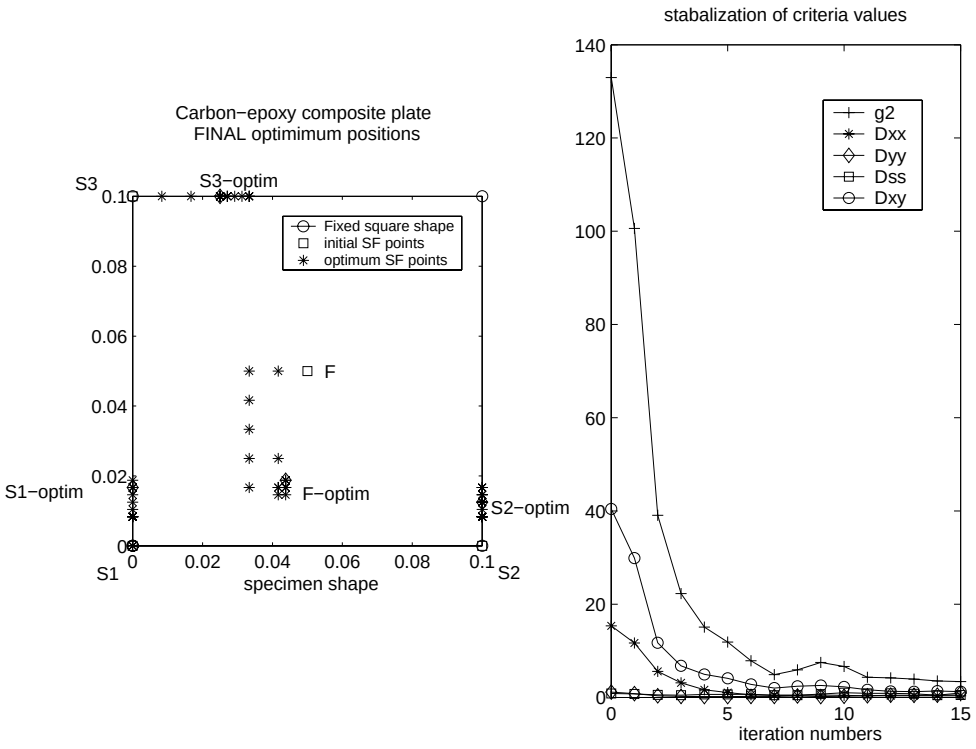

Figure 6.20: Carbon-epoxy composite plate, Optimized Config-1 with optimum supports (restricted to the plate boundary) and force points.

observe a very similar final optimum placement of the support and force application points. Similar conclusion my be drawn in terms of *% reduction* by comparing the results quoted in Table 6.32 to that of the corresponding case no.5 in Table 6.31.

Sensitivity index values for an optimized Config-1					
Crt:	$g2$	$\delta^{(a)}$	$\delta^{(b)}$	$\delta^{(c)}$	$\delta^{(d)}$
Ref values	132.95	15.35	1.14	0.83	40.42
final values	3.16	0.34	0.93	0.50	1.25
% reduction	*97.62*	*97.79*	*18.77*	*40.43*	*96.89*

Table 6.32: Carbon-epoxy composite plate, sensitivity index values for an optimized Config-1: optimum supports (restricted to specimen boundary) and force application point, step $= 4 \times pitch$.

Thus it may be concluded that for the above studied example the material has no apparent effect on the final optimum positions when both the supports and force application points are optimized.

6.9 Conclusion

In this chapter optimization of a testing configuration is presented and discussed in detail. Effect of different parameters like fiber angle, plate width, location of force application point, location of support points and specimen shape are studied on the noise sensitivity criterion. All these parameters are considered separately and also in combination so as to evaluate the gain in terms of robustness and accuracy of the results. In this regard, Fig 6.21 presents a comparison of all the different optimizations achieved using separate or a combination of variable parameters in terms of noise sensitivity criterion value with reference to initial Config-1.

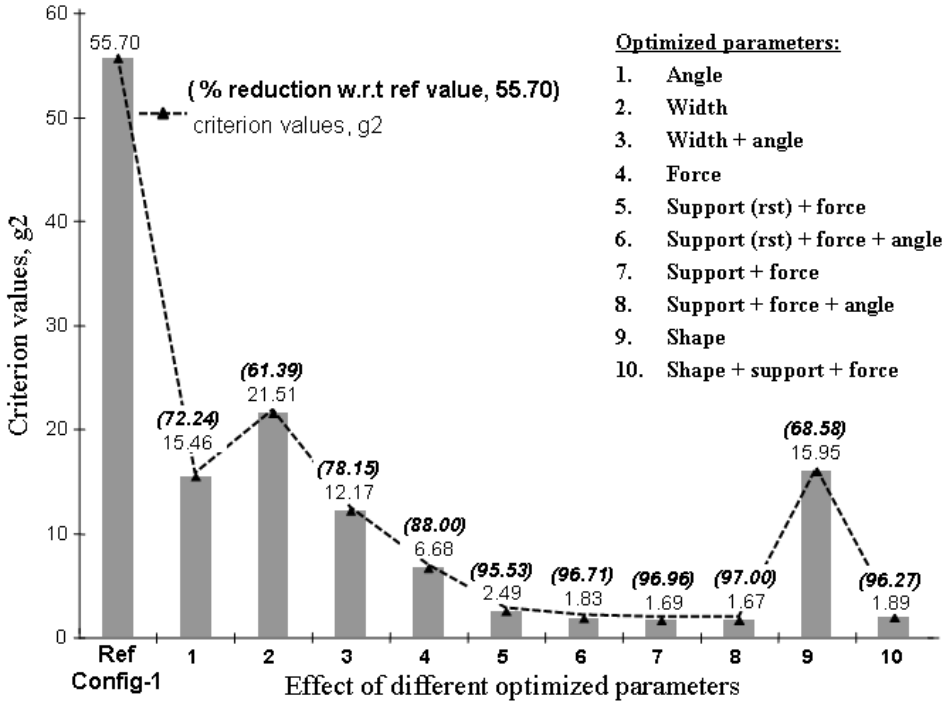

Figure 6.21: A comparative performance graph of all the optimizations studied using various parameters.

This graphs validates the point that when greater number of variable parameters are considered collectively, greatest is the gain in terms of reduced noise sensitivity leading to more robust identification. From this comparative study it may be observed that greatest gain in terms of percentage reduction of reference criterion value is achieved for case no. 8 which represents a combination of optimized supports (free to be placed within the specimen boundary), force application point and fiber angle. However, percentage reductions obtained for cases 5, 6, 7 and 10, are also more or less of the same order and do not exhibit significant differences.

Now in order to identify one best optimum combination of parameters it is important to consider its performance but also ease of its implementation especially from a practical point of view. On this basis an optimization based on specimen shape along with support and force application points (case no. 10) is not a very evident choice. Also from experimental point of view it is reasonably difficult to obtain an irregular shaped specimen. Now, among the remaining solutions an important consideration may be the placement of the optimized support locations. It is quite likely that due to limitations in experimental setup, it is difficult to perform experiments with configurations where supports are to be placed within the specimen and not on the boundary, hence such situations (e.g. case no. 7 and case no. 8) should be avoided. Now, from experimental point of view the last two optimization proposals (cases no. 5 and case no. 6) are equally executable. In both of these, an optimized force application point along with optimized support points are proposed, but the supports are restricted to be placed on the specimen boundary. However the former uses a composite specimen where fibers are oriented along 0° whereas in the later case they are at an optimized angle (20°). Finally case no. 5, optimized supports restricted to specimen boundary, optimized force application point and constant fiber angle along 0°, may be regarded as the better optimization proposal in terms of the equally good performance (a reduction of 95.53% against the maximum 97%) and ease of experimental execution.

It may be concluded that this chapter presents a detailed numerical study where effect of different variable parameters on the better identifiability with minimum noise sensitivity is investigated. The present study is one of the few of its kind where effect of different variable parameters are studied in an effort to optimize a given testing configuration. The effect of different parameters both separately and in combination is studied. The presence of several minima for a combination of variable parameters is also observed. It would be interesting in future to further enrich the optimization algorithm by using for example, genetic algorithms such that a unique global minimum is identified in cases of prevailing local minima as observed in the present work. After a comparative study of the different optimization cases, such a case is identified which on the one hand results in significant reduction of the noise sensitivity criterion and on the other hand is easily applicable from practical point of view. With an illustrative example by using a different testing material, it is also observed here that for the studied case there is as such no effect of using a different material on the final optimized configuration.

In future, it would be interesting to experimentally validate the optimization proposals presented and identified in this chapter especially the ones which are more performing and also easily applicable. In this regard Chapter 8 later presents the first experimental results where the effect of using an optimized force application

point is experimentally evaluated especially in the context of the resulting minimized noise sensitivity on the identification results.

The following chapter now discusses an application of the piecewise virtual fields method. An adaptation of the method is presented for a composite plate with two separate zones of different properties. The idea is to simultaneously identify the set of the different rigidities in the two separate zones.

Chapter 7

An application of piecewise VFM: Identification of a damaged composite plate

7.1 Introduction

This chapter presents an important application of the piecewise VFM. In the previous chapters, bending rigidities are assumed to be constant over the whole plate, this assumption is not considered here. The present work deals with the simultaneous identification of the unknown bending rigidities in two distinct zones having different material properties, for a given composite plate. It presents an adaptation of the identification procedure developed earlier in Chapter 2 for the case when the bending rigidities are no more constant over the whole plate. The present work is in fact a contribution to a separate research work conducted by J.H. Kim, jointly supervised by F. Pierron and M.R. Wisnom respectively from LMPF, ENSAM Châlons, France and Department of Aerospace Engineering, University of Bristol, GB. The research topic is the identification of the local stiffness reduction of a damaged composite plate using the virtual fields method. Such a stiffness reduction is normally observed in case of composite panels. It may be due to a delamination damage caused by an impact or by some manufacturing defects. Such defected panels are prone to premature failure especially in compression loading due to local buckling effects. Thus it is necessary to locate and quantitatively asses the damage criticality for safe working of the concerned component. References [84, 85] fall under the scope of this collaborative work.

With reference to a defect zone, several studies for example, infrared thermography [86], ultrasonic scanning [87], shearography [88], Lamb waves [89], acoustic emission [90], are published in the literature. All of these techniques mainly deal with defect localization and not with the measurement of in situ damaged stiffnesses. Though, there exit some studies related to measurement in change of eigenfrequencies [91] for instance, but it is a global indicator and is not sensitive to a local change in stiffness. To the best of author's knowledge, the present study is the first attempt to measure the local loss in stiffness with the VFM. Some other methods were already used for this purpose such as the CEGM and EGP, refer to Section 1.3.2 and Section 1.3.3 respectively.

The major objectives of the present work are

- to simultaneously identify the plate rigidity in both undamaged and damaged zones with a prior knowledge of the damaged zone location.
- to propose an optimized force application point such that more robust and accurate identification is possible, especially for the damaged zone.
- to apply the piecewise VFM for defect zone localization in a damaged plate and extraction of the damaged zone coordinates.

The adaptations and the methodology used for the above outlined objectives are accordingly discussed here. These are also numerically validated through a simulated example of a damaged composite plate. The simulated damaged composite plate used in the present work is first described in the following section.

7.2 Damaged composite plate description

As per supplied specifications and testing configuration from the fellow collaborators, an example of a damaged composite plate with induced delamination is studied here. It represents a 300mm x 200mm rectangular unidirectional carbon-epoxy composite plate, with 1.68mm thickness. It consists in 6 unidirectional layers with constant thickness of 0.28mm each. The plate contains a delamination defect of 50mm x 50mm in size at a given location. The plate is simply supported at three corners and a vertically downward load **F** of 20N is applied at the center of plate i.e. at point C, refer Fig 7.1.

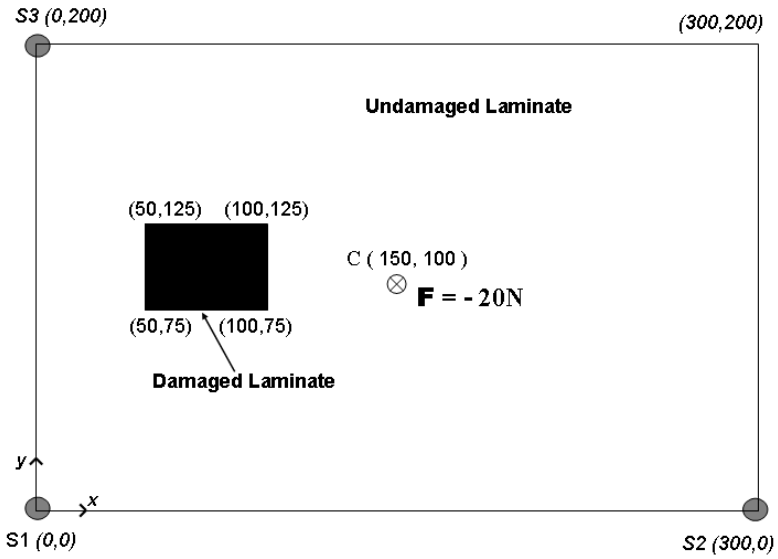

Figure 7.1: A composite plate with simulated delamination effect, loading and boundary conditions.

For the present numerical study, the damaged plate is modeled using ANSYS 9.0 package. The plate finite element model is meshed in 120 x 80 regular square elements of type Shell 99. To numerically simulate the damage zone within the plate, comparatively lesser engineering constant values are assigned for the layers properties contained in this defect zone. This represents an induced defect to simulate the delamination effect. Let A represents the elastic mechanical properties of the layers outside the defect zone whereas B for the layers which are compromised. These respective lamina properties are quoted in Table 7.1. However in an actual scenario, such an induced defect to simulate a delamination may be achieved by cutting few predefined intermittent laminate layers around the contour of the defect region. This results in reduced laminate strength and stiffnesses within the defect zone. Fig 7.2 shows the two types of laminate sequence respectively for undamaged and damaged zones. The corresponding reference rigidity values for these two zones are recorded in Table 7.2. Here it is interesting to note that approximately a constant 25% reduction is obtained in all the damaged zones stiffnesses. The following section now presents the ability of the piecewise VFM to simultaneously identify the bending rigidities separately for the damaged and undamaged zones.

	A $(Undamaged)$	B $(Damaged)$
E_{xx}	140GPa	$140MPa$
E_{yy}	10GPa	$10MPa$
E_{zz}	10GPa	$10MPa$
nu_{xy}	0.3	0.3
nu_{xz}	0.3	0.3
nu_{yz}	0.45	0.45
G_{xy}	5GPa	$5MPa$
G_{xz}	5GPa	$5MPa$
G_{yz}	3.44GPa	$3.44MPa$
$Density$	$1477kg/m^3$	$1477kg/m^3$

Table 7.1: Lamina properties used for modeling undamaged and damaged zones.

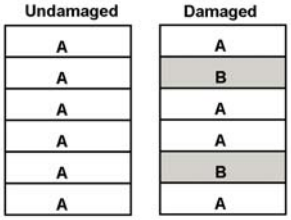

Figure 7.2: Laminate sequence in the undamaged and damaged zones.

Bending rigidities (Nm)	*Undamaged zone*	*Damaged zone*
D_{xx}	55.68	41.26
D_{yy}	3.98	2.95
D_{ss}	1.98	1.46
D_{xy}	1.19	0.88

Table 7.2: Reference rigidity values for undamaged and damaged zones.

7.3 Simultaneous identification of rigidities in damaged and undamaged zones

7.3.1 Introduction

This section presents the adaptation of piecewise VFM when identification is required for plates with separate zones of different properties. For this purpose a case of a damaged composite plate described in Section 7.2 is treated here. It is worth noting that the damaged zone location and size is assumed to be known in advance. It is shown here that making use of the piecewise VFM, simultaneous identification in damaged and undamaged zones is effectively achieved. This enables to evaluate the local loss in stiffness due to delamination. Influence of noisy data onto the identification is also studied here in order to measure the robustness and accuracy of the results. The adaptation of the VFM is now discussed below.

7.3.2 Adaptation of the piecewise VFM for a case of damaged composite plate

For the present identification problem of a damaged plate involving two zones with different rigidities, the principle of virtual work as discussed in Section 2.1 is rewritten for these two zones separately. The global static equilibrium of the specimen is now written by separately considering the contribution of internal virtual work for undamaged and damaged zones. Thus the earlier Eq.(2.1) becomes

$$\underbrace{-\int_{V1} \boldsymbol{\sigma} : \boldsymbol{\varepsilon}^{\star} dV}_{Undamaged\ zone: W_i^*} \underbrace{-\int_{V2} \boldsymbol{\sigma} : \boldsymbol{\varepsilon}^{\star} dV}_{Damaged\ zone: W_i^*} \underbrace{+\int_{S_f} \mathbf{T} \cdot \mathbf{u}^{\star} dA}_{W_e^*} = 0 \quad \forall \ \mathbf{u}^{\star}, \boldsymbol{\varepsilon}^{\star}; K.A \tag{7.1}$$

where, $V1$ and $V2$ are the respective volumes for the undamaged and damaged zones. Let D° and $D^{\dagger}$ represent the respective rigidities in undamaged and damaged zones, then upon developing for the case of plate bending the above equilibrium equation becomes

$$\begin{aligned} &\left(D^{\circ}_{xx} I_{xx} + D^{\circ}_{yy} I_{yy} + D^{\circ}_{ss} I_{ss} + D^{\circ}_{xy} I_{xy} + D^{\circ}_{xs} I_{xs} + D^{\circ}_{ys} I_{ys}\right)^{undamaged\ zone} \\ &\quad + \left(D^{\dagger}_{xx} I_{xx} + D^{\dagger}_{yy} I_{yy} + D^{\dagger}_{ss} I_{ss} + D^{\dagger}_{xy} I_{xy} + D^{\dagger}_{xs} I_{xs} + D^{\dagger}_{ys} I_{ys}\right)^{damaged\ zone} \\ &\qquad = \sum_{i=1}^{n} F_i \cdot w_i^* \end{aligned} \tag{7.2}$$

Hence for the direct and simultaneous identification of these unknown rigidities, it is required to find a total number of twelve special virtual fields. These special virtual fields are obtained in a similar manner using piecewise VFM with noise minimization effect as discussed in detail in Chapter 2 and Chapter 3 respectively. Also for the damaged plate having zones with different properties, matrices A and H, as used in Eq. (3.21), are required to be calculated separately for these corresponding zones. Due to this reason, the coordinates of the damaged zone should be known in advance, which are used here as input. The main idea here is the piecewise construction of the virtual fields separately over the damaged and undamaged zones. Worth noting that for the damaged plate, the virtual elements are chosen in such a way that the damaged zone is perfectly superimposed by either one or a combination of virtual elements and no virtual element is shared by the two different zones.

Now simultaneous identification of damaged and undamaged zone is possible. First using noiseless data, identification is achieved and effect of increasing virtual mesh density is studied in order to identify the optimum number of virtual elements to be used. To measure the result accuracy and robustness, influence of noisy data is also studied on the identification results. For this purpose, as described earlier in Section 4.4.1 a copy of Standard Gaussian white noise is added to the simulated data and standard deviations of identified rigidities both in damaged and undamaged zones are found separately. These are then compared to theoretical expected values to verify the consistency of simulated results as discussed earlier in Section 4.4.2.

Finally, the *variation coefficients* (defined by the ratio between standard deviation of the distribution and the respective average rigidity) are calculated. For a given testing configuration, this gives an idea about identifiability of respective rigidities with respect to noise sensitivity, lesser are the values, minimum is the noise sensitivity.

The identification procedure presented above is numerically validated in the following section for the case of a given damaged composite plate.

7.3.3 Numerical validation: Rigidity identification in damaged and undamaged zones

This section presents a numerical validation of the adapted piecewise VFM as discussed in Section 7.3.2 for simultaneous identification of zones having different properties. The procedure is applied to an example of the plate described in Section 7.2. Simulated data of the damaged composite plate using ANSYS 9.0 package is processed here.

7.3.3.1 Allowable combination of virtual elements

For the present case of damaged plate, such a combination of same sized virtual elements is allowed which ensures that the damaged zone is perfectly superimposed by either one or a combination of such same sized virtual elements and no virtual element is shared by the two different zones. Additionally, as discussed earlier in Section 4.2, it is also important to ensure that the boundary of real and virtual elements must coincide with each other. Now, making use of the known defect zone coordinates, it is required to find such an allowable combination of virtual elements. Considering the known coordinates of the defect zone and the size of given plate, which is meshed in 120 x 80 real elements, it is evident to use minimum 6x8 virtual elements as shown in Fig 7.3. Such a combination leads to the virtual elements of same size and ensures that the virtual element boundary is coincident to the real finite element and also that no virtual element is common to the two different zones.

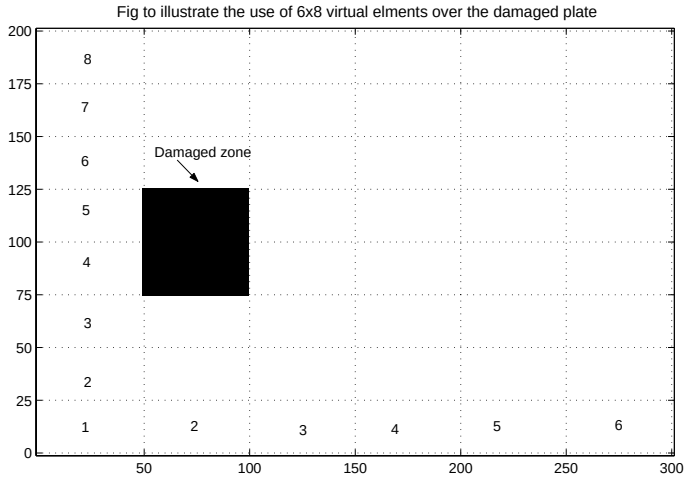

Figure 7.3: Figure to illustrate the minimum allowable use of same sized 6x8 virtual elements over the studied damaged plate

In fact 6x8 virtual elements ensure two virtual elements, of same dimension, over the damaged zone. However other allowable combinations may be 12x16 and 24x40 virtual elements which will ensure that the damaged zone is properly covered by 4 and 10 virtual elements respectively. Identification using these allowable combination of virtual elements are presented in the following section.

7.3.3.2 Identification results without noise

Using noiseless data, simultaneous identification results for damaged and undamaged zones are presented in this section. Identification is achieved using allowable combinations of 6x8, 12x16 and 24x40 virtual elements. However, combinations resulting in even more greater number of virtual elements within the damaged zone

could not be tested due to memory limitations while computation. Identified rigidity values found separately for undamaged and damaged zones, are presented in Table 7.3.

	Undamaged Zone				**Damaged Zone**				
Ref values (N-m)	D_{xx} *55.68*	D_{yy} *3.98*	D_{ss} *1.98*	D_{xy} *1.19*	D_{xx} *41.26*	D_{yy} *2.95*	D_{ss} *1.46*	D_{xy} *0.88*	time
6 x 8 VE	55.77	3.98	1.98	1.21	42.18	3.06	1.49	0.49	9 sec
% rel. err	*0.15*	*0.12*	*0.03*	*1.09*	*2.22*	*3.94*	*2.07*	*-44.77*	-
12 x 16 VE	55.76	3.98	1.98	1.20	41.83	3.04	1.49	0.68	32 sec
% rel. err	*0.14*	*0.11*	*0.03*	*0.96*	*1.38*	*3.05*	*1.87*	*-23.44*	-
24 x 40 VE	55.46	3.98	1.97	1.19	41.52	3.00	1.49	0.64	31 mn
% rel. err	*-0.38*	*0.12*	*-0.09*	*-0.36*	*0.63*	*1.86*	*1.95*	*-27.49*	-

Table 7.3: Identification results of damaged plate without noise.

Table 7.3 records the identification results without noise and shows the capability of piecewise VFM, such that all the unknown rigidities in two separate zones are simultaneously identified. However it is observed that D_{xy} in the damaged zone is poorly identified in all cases. Here it is important to note the small size of the damaged zone, it is only about 4% of the plate total area. It is related to a reduced influence on the plate overall response under loading. Also, this may be related to the fact that for the identification purpose, only 400 simulated measuring points are available for the small sized damage zone, which is very less and insignificant as compared to the available 9200 simulated measuring points for rest of undamaged zone. All these factors may contribute to the difficulty in identification of rigidities within the damaged zone. The following section now discusses the influence of noisy data on the rigidity identification.

7.3.3.3 Influence of noisy data

This section now discusses the effect of noisy data on the identification procedure to examine the robustness of the procedure and the accuracy of the results. Due to computational reasons 6x8 virtual elements are used to study the noise effect. As already described in Section 4.4.1, a Standard Gaussian white noise, γ, equivalent to 5% of the maximum of the absolute values of the three curvatures is used to simulate the noise effect. It is regularly distributed in 6 intervals. The first value $\gamma = 0$ corresponds to the identification without noise. Now, identification is achieved

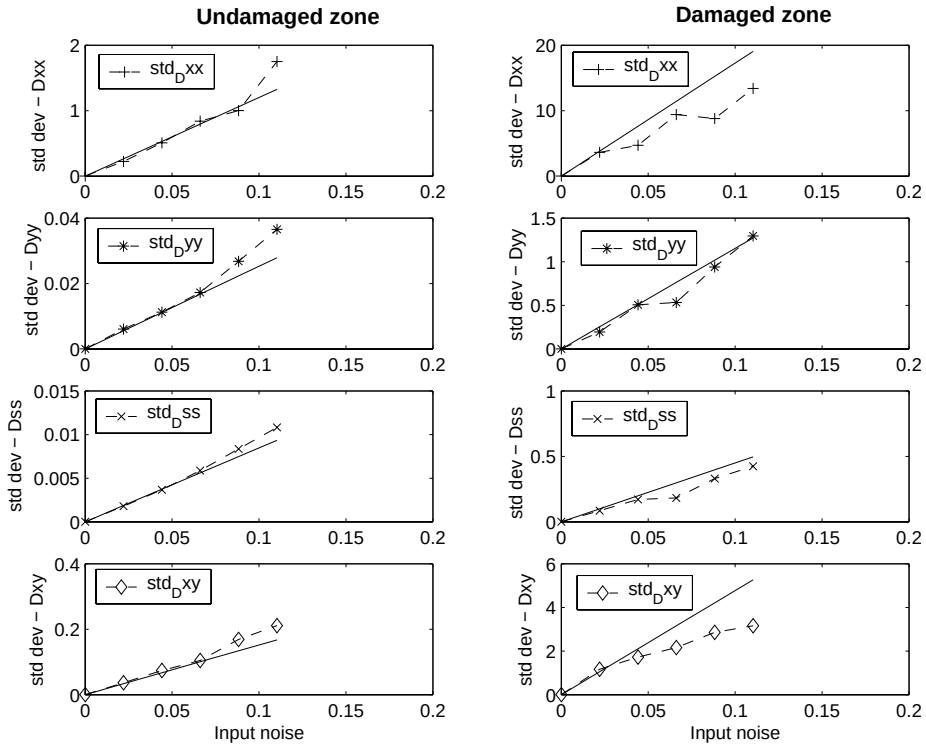

Figure 7.4: Standard deviations of mean rigidities identified at increasing noise levels (γ), using 6x8 virtual elements with load applied at point C.

.

50 times at each of the successive 6 values of γ which will be used to find the standard deviation at a given noise level.

To check the consistency of the simulated results using noisy data, as earlier discussed in Section 4.4.2, standard deviations of identified rigidities are compared to that of the theoretical expectations. These are obtained using the same procedure as in Chapter 4 where undamaged plates are considered. For this purpose, standard deviations of the identified rigidities separately for undamaged and damaged zones are plotted against γ in Fig 7.4. From this figure, for the undamaged zone, it may be concluded that standard deviations of the identified mean rigidities are linear functions of γ, as expected, and that these standard deviation values are in good agreement with the straight line plotted using Eq.(3.18). Also, for the damaged zone they are also fairly acceptable except for some greater variations in case of D_{xx} and D_{xy}. As mentioned before, this is probably related to the relatively smaller size of the damaged zone and the availability of very few measuring points in the damaged zone for identification as compared to the rest of undamaged zone. Moreover, the localization of the loading and the supports is not optimized in this case. For the two zones it may be concluded that the results obtained with simulated noisy data

	Undamaged Zone				Damaged Zone			
Ref Val.	D_{xx}	D_{yy}	D_{ss}	D_{xy}	D_{xx}	D_{yy}	D_{ss}	D_{xy}
(in Nm)	55.68	3.98	1.98	1.19	41.26	2.95	1.46	0.88
no noise	55.77	3.98	1.98	1.21	42.18	3.06	1.49	0.49
rel. err(%)	*0.15*	*0.12*	*0.03*	*1.09*	*2.22*	*3.94*	*2.07*	*-44.77*
5% noise	51.40	3.95	1.95	0.84	28.06	3.00	1.46	-0.11
rel. err(%)	*-7.69*	*-0.60*	*-1.21*	*-29.44*	*-31.99*	*1.69*	*0.02*	*-112.54*
var.coef(%)	*3.14*	*0.92*	*0.55*	*17.69*	*32.46*	*43.98*	*28.98*	*357.06*

Table 7.4: Damaged plate: Identification results using 6x8 virtual elements with noisy data.

are consistent with theoretical expectations. However, it is interesting to observe that, for the undamaged zone, standard deviations for all the rigidities are slightly greater than the expected theoretical values, whereas for the damaged zones for all the identified rigidities, they are all lower than the expected theoretical values.

Finally, the variation coefficients are calculated from the results of 50 iterations. These are presented in Table 7.4 for undamaged and damaged zones respectively. It may be concluded that for the undamaged zone the rigidities are fairly stable to the noisy data except a comparatively higher deviation for D_{xy}. However, especially for the damaged zone, it is evident that the identified rigidities are very much sensitive to noise and particularly D_{xy} is extremely sensitive. This may be a justification for poor identification of D_{xy} even in the case of noiseless data, refer to Table 7.3. As discussed earlier, this may be related to the small size of the damaged zone in addition to the very few measuring points available over this small zone in comparison to the larger undamaged zone. All these factors contribute to the difficulty in identification of rigidities within this zone.

On account of the observations made earlier in Section 5.4, such a sensitivity to noise may be due to the fact that the loading position is not optimized as it is found on the diagonal formed between the two supports. Now to further extend the idea, such a testing configuration may be searched which results in more robust and accurate identification with least sensitiveness to noise especially for the damaged zone. This issue of optimum testing configuration is now discussed in the following section.

7.4 Optimization of force application point

7.4.1 Introduction

For a given system of boundary conditions, the effect of loading position is studied here on the identification results, especially for the better identifiability of damaged zone. The idea is to find such an optimal load position which leads to a more robust identification with reduced sensitivity to noise. The detailed procedure is already discussed in Section 5.4.

7.4.2 Optimized force application point

For a quick reference of the damaged zone location, Fig 7.5 replots the testing configuration with three corner supports (S1, S2 and S3) for the given damaged composite plate. In order to find an optimized load application point, the applied load $\mathbf{F}$ is now moved within the plate and identification is achieved at each location. Thus, a thorough sensitivity scan is performed for the entire plate. For the identified damaged zone rigidities $D^{\dagger}$ at each point of force application, the corresponding values of the individual sensitivity values, δ^{α} (refer to Eq. (5.1)) and global cost function g (refer to Eq. (5.2)) are noted. These respective sensitivity scans are plotted in Fig 7.6 and Fig 7.7. In the first case, testing configuration is optimized for each of the four unknowns considered separately whereas they are globally considered in the second case.

From these sensitivity scans it can be observed that there are very significant variations in sensitivity values over most of the plate surface. To compare with a plate without a damaged zone, Fig 7.8 presents a sensitivity analysis based on global criterion g for a composite plate with exactly the same specifications as that of the studied damaged plate except that no damage is induced in this plate. The two scans presented in Fig 7.7 and Fig 7.8 respectively for a damaged and undamaged plate are now compared. It is evident that in case of an undamaged plate it is more regular with no drastic variations from one point to other. However, for damaged plate it is very variable. Using the sensitivity scans in Fig 7.6, separate load application points are found for each of the unknown damaged zone rigidity (at minimum values of $\delta^{(\alpha)}$). Also a unique point using global cost function (at minimum values of g) is found from Fig 7.7 which can identify all the damaged zone rigidities with best accuracy and robustness. These respective optimum loading positions denoted as I, J, K are shown in Fig 7.9. However it is worth noting that for the flat regions observed in the scans, an applied loading can be placed within this region, though the sensitivity value is not minimum but acceptable. Table 7.5 records the noise sensitivity index values for the above found optimum load application points.

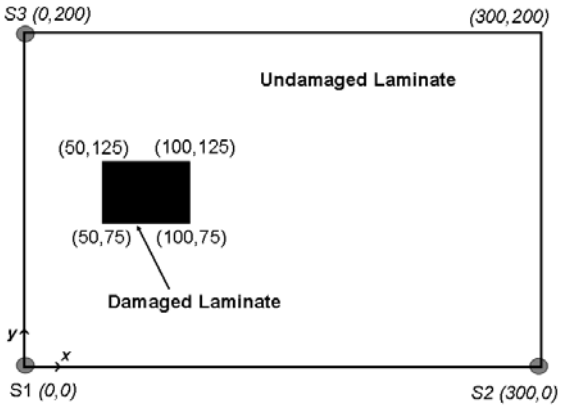

Figure 7.5: A composite plate with simulated delamination effect and boundary conditions.

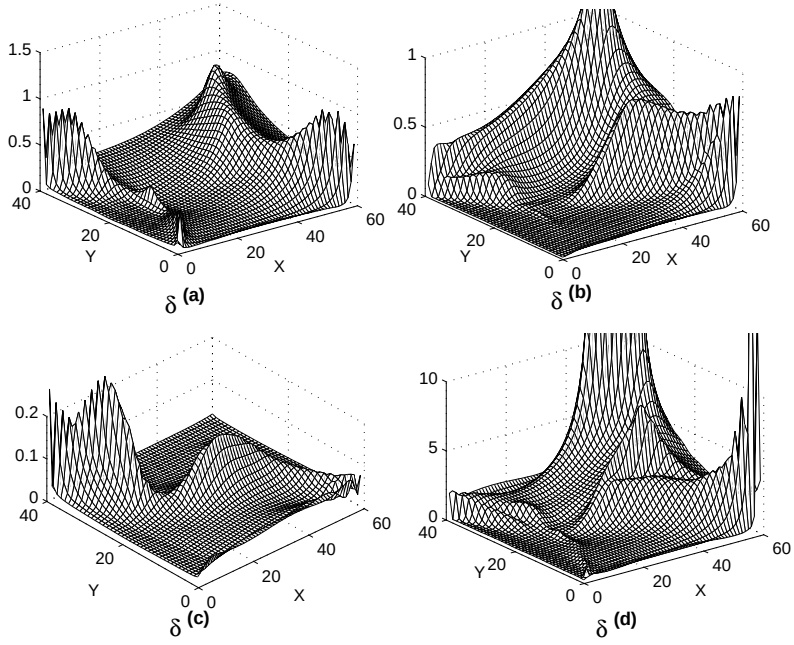

Figure 7.6: Damaged plate, 3D image of the noise sensitivity criteria : $\delta^{(\alpha)}$

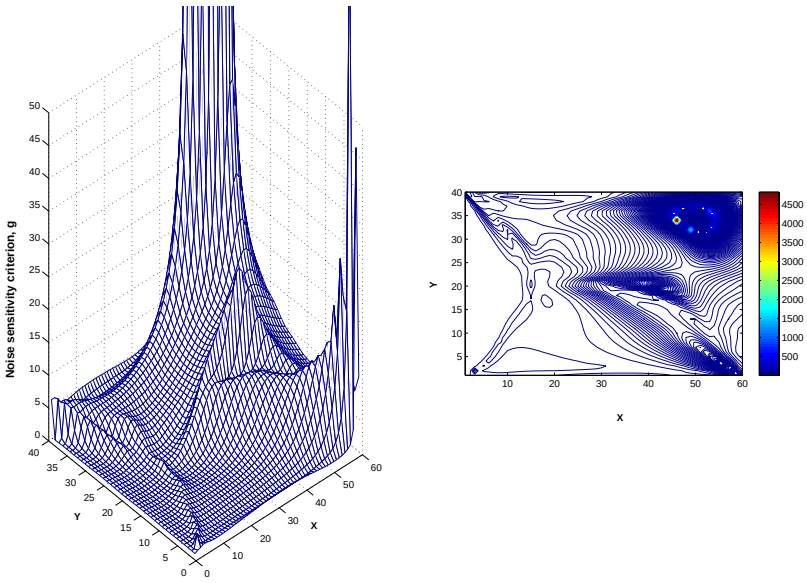

Figure 7.7: Damaged plate, 3D image of the noise sensitivity criteria : g

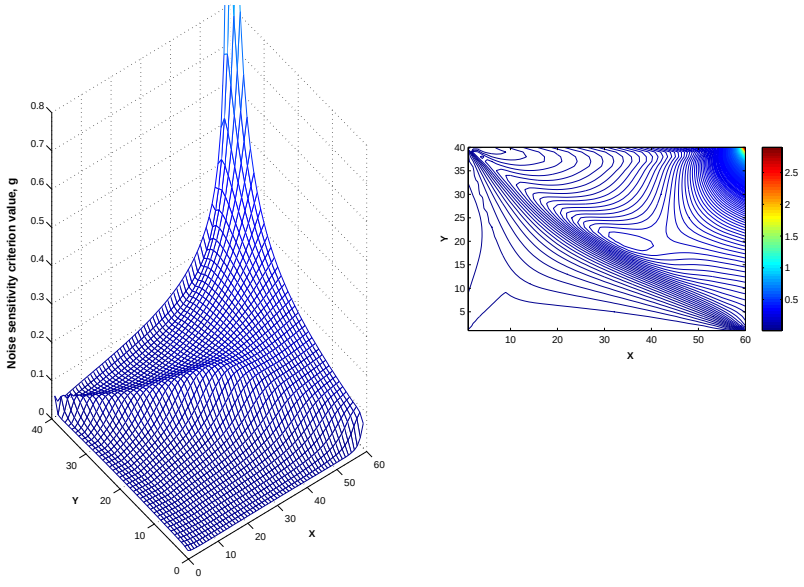

Figure 7.8: Undamaged plate, 3D image of the noise sensitivity criteria: g.

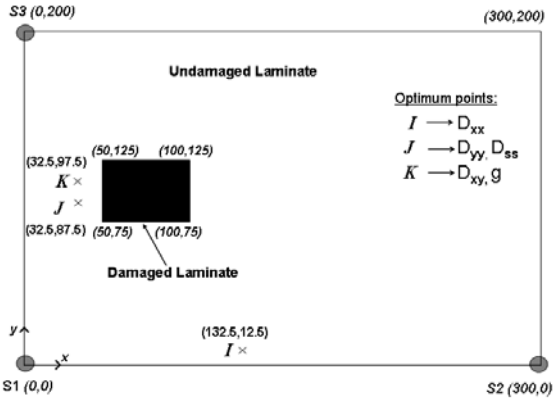

Figure 7.9: Damaged composite plate showing optimum force application points.

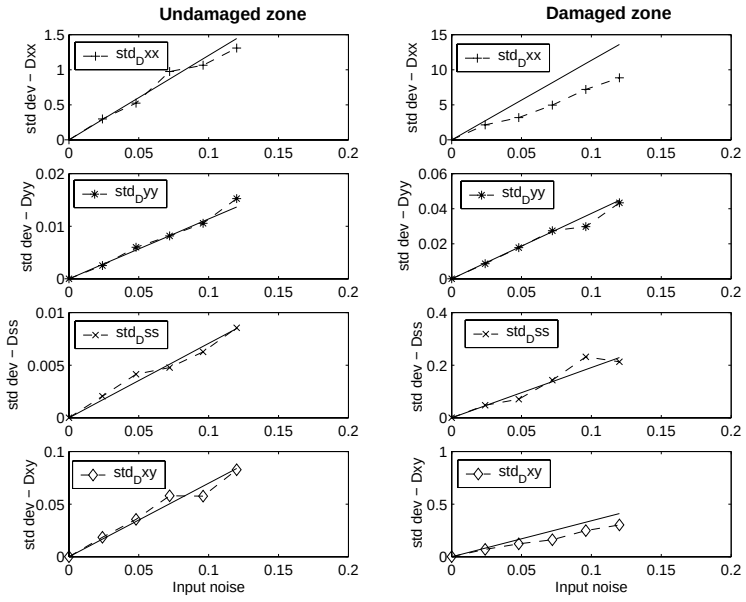

Figure 7.10: Standard deviations of mean rigidities identified at increasing noise levels (γ), using 6x8 virtual elements with load applied at optimum point K.

Criteria :	force location (x,y) (mm)	$\delta^{(\alpha)} \times 10^{-3}$			
		$D^{\dagger}_{xx}$	$D^{\dagger}_{yy}$	$D^{\dagger}_{ss}$	$D^{\dagger}_{xy}$
$\delta^{(a)}$	I(132.5,12.5)	13.2	19.5	35.0	198.1
$\delta^{(b)}$, $\delta^{(c)}$	J(32.5,87.5)	21.7	0.9	9.3	32.9
$\delta^{(d)}$, g	K(32.5,97.5)	22.4	1.0	10.4	31.6

Table 7.5: Noise sensitivity index values at optimum force locations for better identification of damaged zone properties.

It is interesting to note here that the results for locations J and K are approximately equivalent. Hence the location K using the criterion g can be regarded as the optimum loading point capable of extracting all the rigidities of the damaged zone with least possible noise sensitivity. To verify the consistency of results using noisy data at the optimum location K, standard deviations of the identified mean rigidities for both the zones are plotted against the theoretical values and they are found to be in good agreement, refer Fig 7.10. With reference to earlier observation regarding Fig 7.4, it is interesting to note in Fig 7.10 that the standard deviations for the undamaged zone are now well balanced and are in very good agreement to the expected theoretical values. Similarly, improvement is also observed for the damaged zone.

	$\delta^{(\alpha)} \times 10^{-3}$							
	Undamaged Zone				Damaged Zone			
force applied at:	D°_{xx}	D°_{yy}	D°_{ss}	D°_{xy}	$D^{\dagger}_{xx}$	$D^{\dagger}_{yy}$	$D^{\dagger}_{ss}$	$D^{\dagger}_{xy}$
center C(150, 100)	8.5	2.3	1.4	54	172.1	137.5	91.2	3879.0
K(32.5, 97.5)	1.9	0.2	0.3	5.3	22.4	1.0	10.4	31.6

Table 7.6: Noise sensitivity index values before and after optimization.

Table 7.6 presents the results of noise sensitivity index values for both the damaged and undamaged zones in the cases of unoptimized (loading case in Fig 7.1) and optimized load locations. For the damaged zone, at the optimum point K also, except for Dyy the sensitivity values are fairly high but significantly lower in comparison to the case when load was applied at point C, the center of plate. Noting the fact that optimum point K is based on the global criterion g which considers only the damaged zone rigidities, however, it also leads to more robust and better identification for the undamaged zone also. Finally it may be concluded that, with the help of only one test using the optimum point K all the rigidities both in damaged and undamaged zones are identifiable.

7.5 Localization of defect

7.5.1 Introduction

This section presents the ability of the piecewise VFM used for the localization of a defect zone. The present numerical study may be regarded as an initial attempt in an effort to develop a defect localization procedure. For this reason, a reference damaged plate is considered here such that the size and exact location of the defect zone is known in advance. Now with the procedure developed here, defect localization is performed and the localized defect is compared to the actual induced defect. This helps to assess the efficiency with which a defect is localized. This study may be regarded as a confidence building exercise such that the same approach may later be applied with confidence to a case where no prior knowledge of the defect is available.

The present study makes use of the same damaged plate as described in Section 7.2 and plotted in Fig 7.1. Remembering that the defect zone in fact represents a delamination within a given composite plate. Here it is assumed that all the damaged zone rigidities with respect to that of the undamaged zone are reduced by a same constant *reduction factor*. A constant reduction of approximately 25% is observed in all the damaged zones stiffnesses, refer Table 7.2. The adaptation of piecewise VFM is now discussed which enables to plot a stiffness reduction map for the damaged plate and thus defect localization is possible.

7.5.2 Principle and methodology of defect localization

Noting that all the rigidities in the defect zone are degraded with a constant reduction factor with respect to the properties found outside the defect zone. Thus the idea here is to use a suitable polynomial function and to plot a 2D stiffness reduction map. Now, on this map the stiffness reduction zone may be localized and this zone is in fact the damaged zone. For the purpose of defect zone localization a stiffness reduction parametrization is used which is written as [84]

$$D^{\dagger} = D^{\circ} \left\{ 1 + p\left(x/L, y/W\right) \right\} \tag{7.3}$$

Here, $D^{\dagger}$ is the bending stiffness tensor of the damaged zone while D° is that of the undamaged area. However, here it is assumed that undamaged zone rigidities, D°, are equivalent to homogenized or averaged plate rigidities. p represents a polynomial function of the normalized in-plane coordinates x/L and y/W, L and W are the composite plate length and width respectively. This polynomial may be interpreted as stiffness reduction coefficient whose value should be less than one in the damaged zone. Hence by evaluating this polynomial function for the damaged plate,

the zone with values less than unity may be identified which is in fact the damaged zone. For the defect localization following stepwise approach is undertaken:

- initially the homogenized or averaged stiffnesses, D°, of the damaged plate are identified. They will be later used as an input to find the unknown coefficients of polynomials.

- using the same earlier Eq. (2.7), the piecewise VFM is adapted to plot stiffness reduction map. For this, the unknown rigidities are respectively replaced by using the polynomial function given in Eq. (7.3) and the coefficients of the polynomial are the unknowns to be determined. The system of equations is developed as before using piecewise VFM and noise minimization effect (see Chapter 2). In this case, as many special virtual fields as the number of unknown coefficients, are required. Finally, the unknown coefficients of polynomials are identified. They are then used to draw the 2D stiffness reduction map.

- the stiffness reduction map is now processed to localize the defect zone closest possible to the actual defect. This is an approximate and repetitive process. Recalling that the size and location of the actual square shaped defect present in the composite plate, is assumed to be known a priori. In fact the map is filtered in such a way that only the zone containing values less than unity (equal to a predefined fraction of unity i.e. reduction factor) is isolated and is enclosed with a box. The dimension of this box (of the resulting four corners) is then compared to the actual damage dimension and relative error is noted. Now, respective relative errors are evaluated for increasing reduction factors such that a particular reduction factor value is found which results in minimum relative error of the localized zone. The coordinates associated with this reduction factor represent the localized defect. However, such an approach is found limited to a case where only a regular shape (e.g. square or rectangular) defect may be localized.

It is important to note here that a reduction map may be obtained by using a given polynomial order and number of virtual elements. Therefore, before processing any reduction map it is essential to establish its optimality in terms of polynomial order and virtual elements used, this issue is discussed in the following section.

7.5.3 Search for an optimum stiffness reduction map

This section presents the search for an optimized stiffness reduction map, which is obtained by using optimum polynomial order and number of virtual elements. It is important to note that a higher order polynomial is advantageous as it is more capable of detecting the variations. However, greater is the polynomial order, greater are the unknown coefficients in addition to the increased numerical errors. Similarly, use of more virtual elements is advantageous but after a particular optimum combination of virtual elements there is no significant gain in using even more virtual elements, as illustrated in Section 4.3. Hence it is required to find a sufficiently high order polynomial to be used with an optimum number of virtual elements which is capable of mapping the stiffness reduction over the damaged plate.

Recalling that for the present case of damaged plate a constant stiffness reduction factor is induced in the damaged zone. Thus for this reference damaged plate for which the defect size and location is assumed to be known in advance, a reference stiffness reduction map may be constructed. In this reference map, a constant value of a predefined reduction factor is assigned to all the measuring points within the damaged zone where as unity to the rest of the plate.

Now, polynomials with increasing orders are tested with increasing number of piecewise virtual elements and the stiffness reduction maps are obtained. The obtained stiffness reduction maps are then compared to the reference map and residual values λ are found in each case. This residual value, λ, is in fact a quadratic distance estimator defined by Eq. (7.4). For a given polynomial order and number of piecewise virtual elements used, it is evaluated by considering all the polynomial function values at n_e different points whose coordinates are given by x_g and y_g over the plate

$$\lambda = \sum_{i=1}^{n_e} \left\{ \left(poly.value - ref.value\right)^2 / ref.value^2 \right\}_{i_{(x_g, y_g)}} \tag{7.4}$$

In fact it is also appropriate to conduct such residual analysis separately for damaged and undamaged zone. For increasing polynomial order and virtual elements combination, damaged zone analysis gives an idea about better detection of defect zone, whereas the undamaged zone analysis is able to detect if the values outside defect zone are detected closer to unity as expected, thus it gives an idea of incurred deterioration. An optimum stiffness reduction map is the one which has a good compromise between these two zones for which the optimum order polynomial and number of virtual elements are identified.

Now the stiffness reduction map obtained from this optimum combination is processed as described before for detecting the defect zone and extracting its coor-

dinates closest to that of the reference damaged zone. This also gives an idea of the accuracy with which a known defect may be located. The following section now presents a numerical validation of the defect localization method.

7.5.4 Validation: Defect localization

For the studied case of damaged plate where an approximate 25% constant stiffness reduction is induced in the damaged zone, a reference stiffness reduction map is constructed. In this reference map, a constant value of 0.75 is assigned to all the measuring points within the damaged zone whereas unity to the rest of the plate. Now, polynomials with increasing orders (from 2^{nd} to maximum up to $8^{th} order$ are tested with increasing number of piecewise virtual elements, such that for a given polynomial order separate stiffness reduction maps are accordingly obtained by using combinations of 4×4, 8×8, 10×10 and 20×20 virtual elements. Fig 7.11 plots the reference 2D stiffness reduction map for the damaged composite plate, such that a constant value of 0.75 and 1 are respectively imposed on the damaged and undamaged zone. For illustration purposes, it also plots some other exemplary stiffness reduction maps which are obtained by using the different combinations of polynomial order and virtual elements.

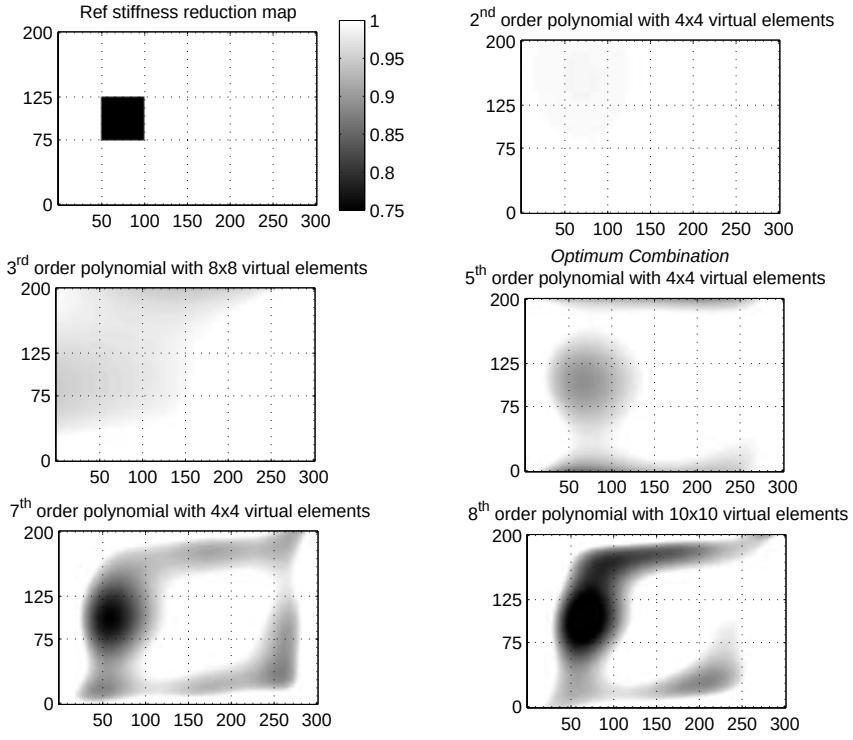

Figure 7.11: Stiffness reduction maps for different polynomial orders and virtual elements.

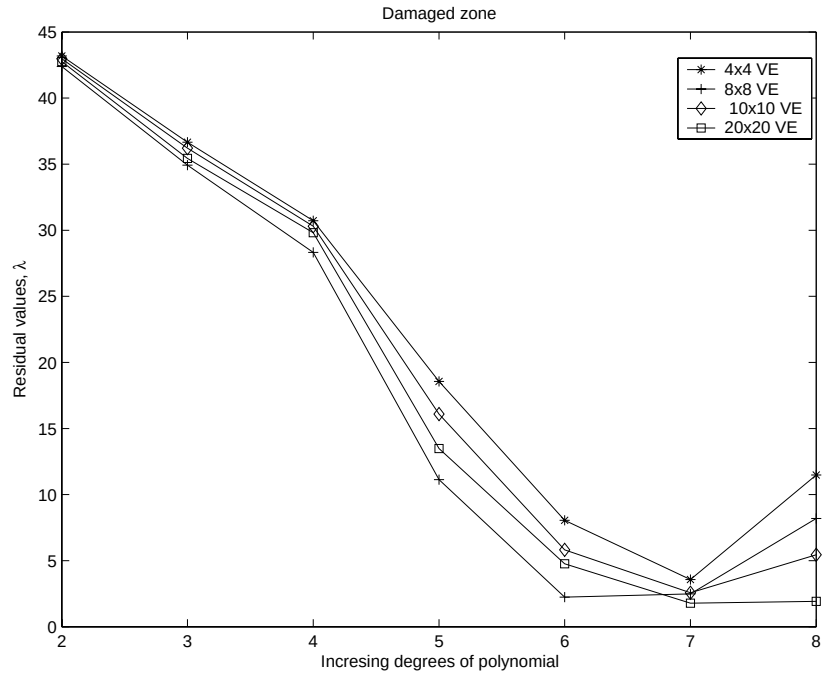

(a) For damaged zone

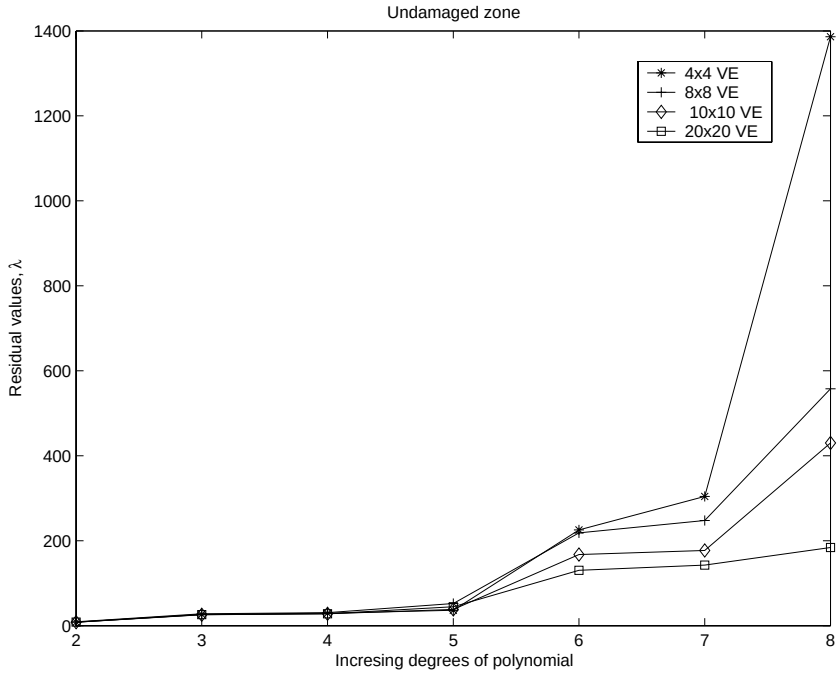

(b) For undamaged zone

Figure 7.12: Residual values plotted separately for the damaged and undamaged zones.

The obtained stiffness reduction maps are compared to that of the reference map and residual values λ, defined in Eq. (7.4), are found in each case separately for damaged an undamaged zones. These are plotted respectively in Fig 7.12. Additionally, Fig 7.13 presents the residual value analysis when complete plate is considered.

From Fig 7.12(a) for the residual value analysis of damaged zone, it may be concluded that a 7^{th} order polynomial results in minimum values. Also, regarding number of virtual element no significant gain is observed by using more and more elements, hence use of 4x4 virtual elements can be concluded to be sufficient. Contrary to this, from Fig 7.12(b) for the undamaged zone, it is evident that the use of 5^{th} order polynomial with 4×4 virtual elements is allowable as beyond that the results are sharply deteriorating. Thus finally for the defect localization, combination of 5^{th} order polynomial with 4x4 virtual elements may be identified as an optimum combination for the studied case. This combination is thus effectively capable of locating the defect zone with minimum deterioration in the undamaged zone. The same conclusion is also evident when the residual value analysis of the whole plate is considered in Fig 7.13.

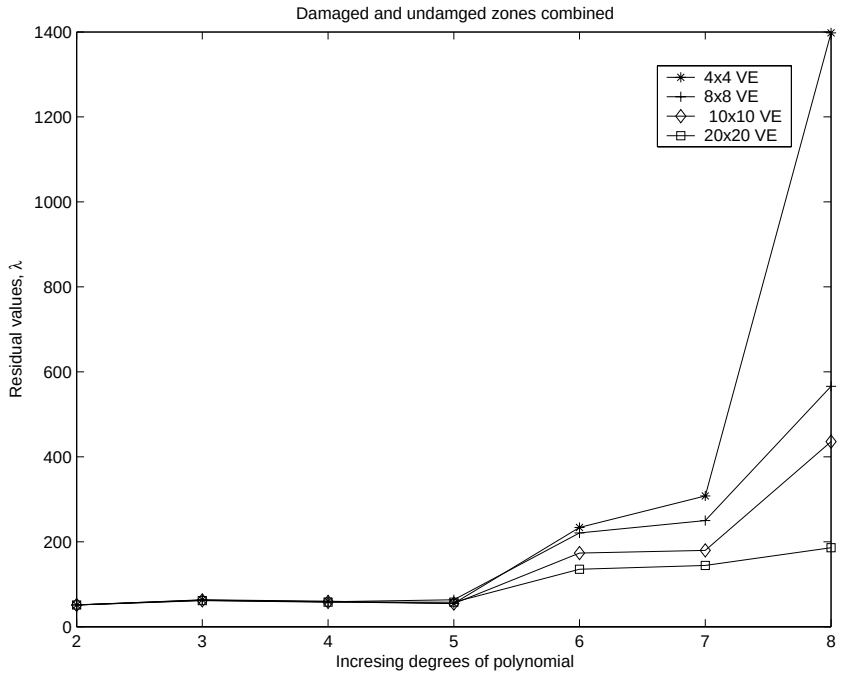

Figure 7.13: Residual value plotted for the whole plate.

From the obtained stiffness reduction maps, it is interesting to note that the defect zone is clearly visible and a fairly good idea of its size and location is possible. However, it is now required to precisely locate the defect zone in comparison to the actual defect. For this purpose, making use of the optimum stiffness reduction map

in comparison to the reference map, the defect zone is isolated. As discussed earlier in Section 7.5.2, a box is constructed around the localized defect zone. Initially, with the points with reduction factor equal to 0.75 only, a box is constructed and the resulting box coordinates are evaluated. These coordinates are compared to the reference square shaped defect with known locations. The resulting relative percentage difference of each corner of the box is noted. Now in a systematic manner the allowable reduction factor is slightly reduced and a comparatively bigger size box is constructed with more points enclosed within it. Again, the percentage difference of each of the resulting corner of the box is evaluated and compared to the reference square shaped defect. For the present case of damaged plate, a box constructed by using a reduction factor of 0.69 results in minimum relative difference with respect to the reference square shaped defect. The final filtered stiffness reduction map with an isolated defect zone closest to reference defect is presented in Fig 7.14 along with reference and optimum stiffness reduction maps. Table 7.7 records the identified coordinates of the box constructed around the isolated defect zone in comparison to actual defect zone coordinates.

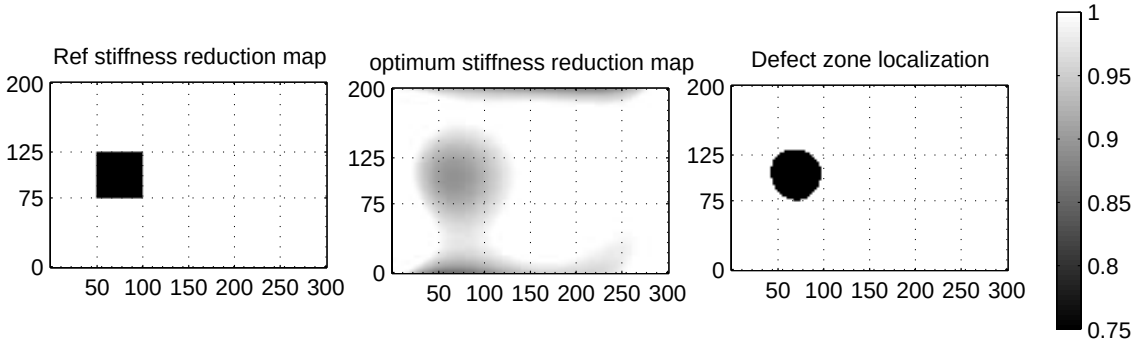

Figure 7.14: Extraction of approximate defect zone coordinates using optimum stiffness reduction map. Approximate defect zone is constructed with a reduction factor of 0.69 instead of 0.75 for the actual zone.

	Coordinates of localized defect zone					
(in mm)	$x_{initial}$	x_{final}	$y_{initial}$	y_{final}	$Length$	$Width$
Ref	50	100	75	125	50	50
Detected	43.7	96.3	71.2	123.8	52.6	52.6
rel. err(%)	*-12.5*	*-3.75*	*-5*	*-1*	*5*	*5*

Table 7.7: Comparison of the localized defect zone to the actual induced defect.

From above results it may be concluded that the above discussed adaptation of the piecewise VFM method is effectively capable of detecting the defect zone with

a fairly good resolution. However, in the present studied case the actual defect was known in advance. It gives a fairly good idea of approximate defect size and its location. Additionally with a trivial method, the defect zone coordinates are also extracted which are found to be in good agreement with the reference induced defect whose size and location was known in advance.

7.6 Conclusion

This chapter presents an important application of the piecewise VFM. It is a contribution in the framework of a separate research work dealing with the assessment of local loss in stiffness in damaged composite plates using the VFM. This research work is conducted by J.H. Kim at LMPF, ENSAM Châlons. The composite plate specifications are supplied by LMPF and it contains an induced damage, simulating a delamination effect, of a known size and location.

In the present work, an adaptation of the piecewise VFM is discussed for simultaneous identification of bending rigidities in two separate zones of the damaged composite plate. The procedure is numerically validated using a simulated example of the damaged plate. With the knowledge of damage zone location, which is assumed to be known a priori and is used as an input, simultaneous identification of the unknown bending rigidities of damaged and undamaged zones is achieved. Both for the cases of noiseless and noisy data, the identification is achieved and the accuracy and robustness of the results is discussed. In addition, an optimized force application point is also proposed. It is shown that more robust and accurate identification is possible for both damaged and undamaged zones at this optimum force location. A defect localization procedure based on the piecewise VFM is also discussed in the present work. However it represents a preliminary work, where an already known defect is localized. It enables one to evaluate the effectiveness of the localization effort with reference to the known defect. At this stage, the objective of the present collaborative work is achieved and a numerically validated identification system capable of determining local loss in stiffness is developed. Future works may include the experimental validation of the identification and the defect localization procedure discussed here. In this regard, it would be interesting to study the effect of varying defect zone properties and its location. Also, it would be interesting to study the effect of optimized support locations in addition to optimized force application point.

Following chapter now presents the first experimental results, it serves to preliminary validate the simulated expectations earlier observed in Chapter 5.

Chapter 8

Experimental results

8.1 Introduction

This chapter presents preliminary experimental validation of betterment in robustness and accuracy of results when a testing configuration with optimized force application point is used with piecewise virtual fields method and noise minimization effect. The experiments based on deflectometry technique [11] are performed by J.H. Kim, a Ph.D. student at LMPF, ENSAM Châlons. The following section describes this full-field optical measurement technique employed to identify bending rigidities of anisotropic plates. Then, experimental results of a testing configuration with optimized force application point is discussed. Improvement in terms of identifiability, robustness and accuracy of results is illustrated by comparing experimental results of a non-optimized to that of an optimized testing configuration. The basic interest is to study and evaluate the betterment in terms of identification results accuracy and reduced sensitivity to noise as observed after simulation study. The preliminary results presented here only verify the numerical results discussed in Section 5.4 for a case of optimized force application point. Additional experiments should be performed in the future to verify the other results discussed in detail in Chapter 6.

8.2 Deflectometry

8.2.1 Introduction

Deflectometry [11, 2, 12] is a full-field optical measurement technique to measure slope fields onto the surface of a bent plate. Deflectometry may be regarded as a low-cost, easy to implement and a more practical method which relies on the measured full-field heterogeneous slope fields for simultaneous extraction of thin plate bending rigidities from a single test. Worth noting that the interest of measuring slope over

deflection is that only one differentiation is required to obtain the curvatures which are directly related to the strain in the framework of Love-Kirchhoff thin plate theory. This technique has been successfully used and validated in case of plate bending [2, 12]. Basic principles of this technique are recalled below.

8.2.2 Principle

Deflectometry is based on the laws of specular light reflection. This technique requires a reflective specimen surface such that image of a reference grating on this reflective surface is visible. It consists in observing the image of this reference grating on the surface of the tested specimen and to process the change of phase caused by a local rotation. Phase measurement of this grating image before and after loading provides slope fields over the tested plate. A digital camera is used to capture images of the reference grating before and after loading. The images are stored in a computer. These are then processed to obtain the required slope fields by means of an appropriate software called Frangyne developed by Surrel [92]. Frangyne is suited to detect very small variations of the grating pitch caused by surface deformation. Now this measured slope field is derived to get actual curvature fields over the plate surface which are then used as an input to VFM for extraction of plate bending rigidities.

For the present case of quasi-planer plates, basic working principle of deflectometry is presented in Fig 8.1(a). AA' represents a reference cross-lined grating which can be obtained by plotting dark lines on a white background with a given pitch noted p. The plate top surface is made highly reflective (mirror like) either by surface treatment or by applying some reflective coating. The camera placed behind the grating, observes the grating image on the plates surface through a hole. Reference grating and the specimen plate are separated by a distance h.

Now with the use of a suspended mass for instance to apply the loading, out-of-plane displacement and slope variation are observed. Thus for a deformed plate, the reflected ray from point M captured by the camera comes from a slightly shifted point Q instead of point P in case of an undeformed plate. To be noted here that out-of-plane displacement of point M affects the displaced position of point Q. However, when this shift remains negligibly small in comparison to h, as in the present case of quasi-planer plates, main effect is that of the slope variation with minimum position dependence. In this configuration a local change in slope α_x at point M is easily related to the displacement of grid image. In fact for a plane reflecting object the grid image is symmetric to the grid with respect to the object. Hence if a local rotation of the object surface is considered at point M then the grid image is rotated about M by an angle of $2\alpha_x$. Point Ω, normal projection of M on

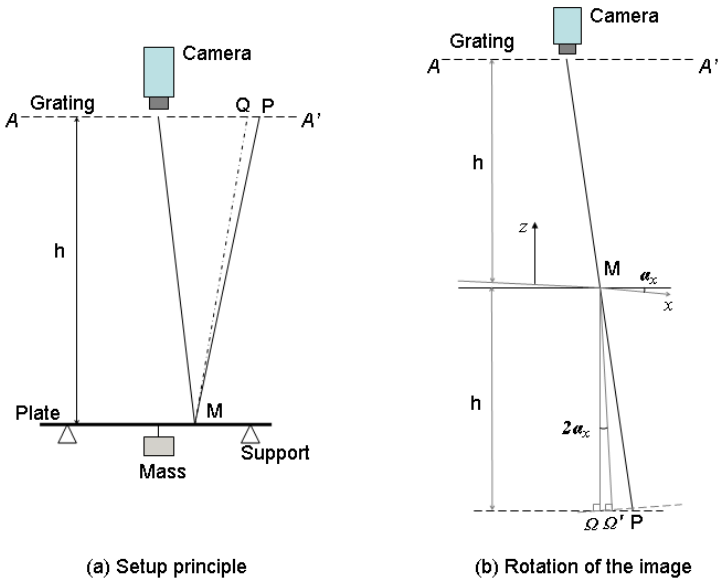

Figure 8.1: Principle of deflectometry applicable to bent plates [2].

the grid image, will be moved to Ω' and the corresponding displacement of grid image u_x can be evaluated as: $u_x = \Omega\Omega' = 2h\alpha_x$. Making use of the cross-lined grating, separate information in the two in-plane directions are realized simultaneously and the two slope components, α_x and α_y are measured. Now phase detection is achieved by analyzing the reference grating image using spatial phase-stepping [93]. Ratio between detected phase and local slope variation is defined as sensitivity, s, which is evaluated directly as: $s = 4\pi h/p$ [12]. Resolution σ_α, also called detection level can be obtained from amount of noise σ_ϕ in the phase measurement as: $\sigma_\alpha = \sigma_\phi/s$. Noise amount in the phase can be experimentally evaluated by subtracting two consecutive independent measurements made for a given testing configuration without changing any parameter [2, 12].

8.3 Experimental results

8.3.1 Set-up parameters

A grating of pitch $p = 2mm$ printed using a plotter is used. A 1296×1030 CCD Basler A113P camera is used to record the images with an objective lens of AF NIKKOR having $28 - 105mm$ focal length. The size of recorded images is $1157x861$ pixels, with 6 pixels per grid period. Using a metallic tape meter, distance h between the grid and plate surface is measured to be $125cm \pm 1mm$. Sensitivity s is found to be 785 using the relation $s = 4\pi h/p$. This corresponds to a sensitivity of 7.85 radians phase per milliradian of slope. For the studied setup, phase noise, σ_ϕ, equivalent

to 1.11x10^{-4} radians is evaluated experimentally. It is evaluated by the standard deviation of the phase fields obtained by subtracting two consecutive images of the plate at rest. The mechanical setup to perform experiments is presented in Fig 8.2 along with separate enlarged photos to demonstrate the support and force application mechanisms.

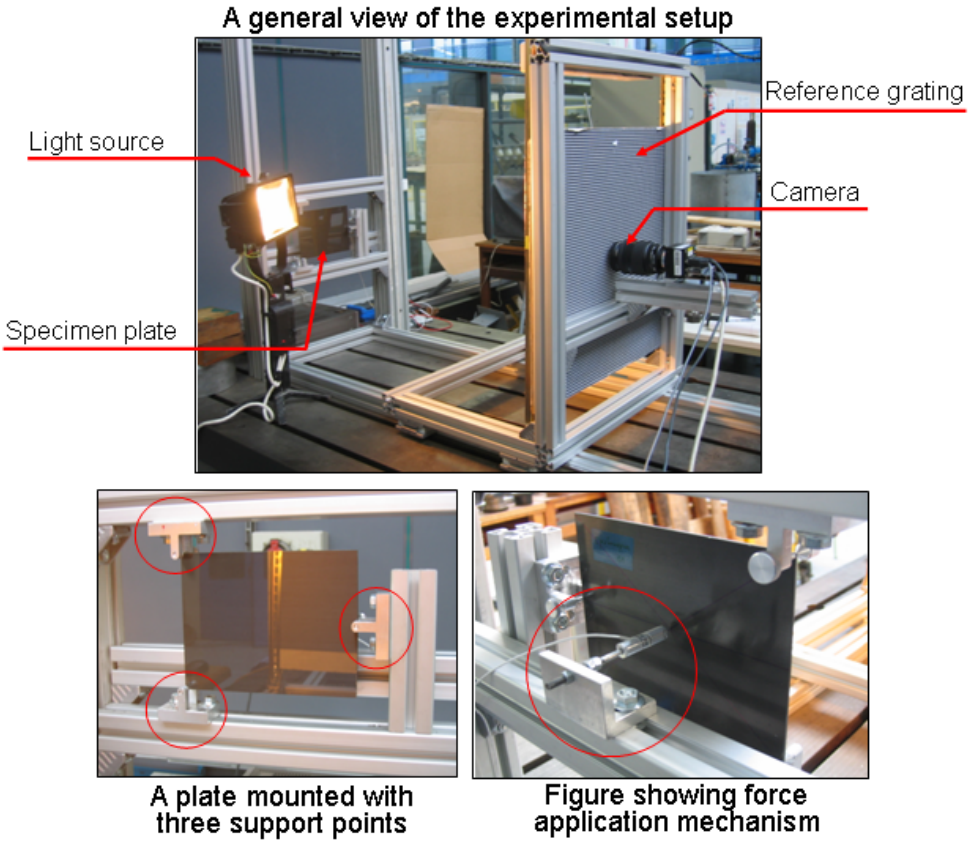

Figure 8.2: A general view of the deflectometry set-up.

A light source is used here to illuminate the grating panel whose reflection is visible on the specimen surface. This reflection is in fact captured by a mounted CCD camera which observes the specimen plate through a hole in the grating panel. The composite specimen plate is supported by using specially designed point grips which give simple support conditions. A screw driven rod mounted with a load cell is used to apply a $5N$ load in the present experimental work.

8.3.2 Specimen preparation

For experimental validation, unidirectional $T300/914$ carbon epoxy laminated composite plates $[0_8]_s$ are tested. Typical elastic constants values for this composite material can be found in refs. [94, 95]. Rectangular laminated composite specimens of $190mm$ x $140mm$, $2.68mm$ thick are fabricated with fibers oriented along x-asis.

In order to have a reflective specimen surface such that image of a reference grating is visible, the plates to be tested are coated with a special epoxy resin coating Surf Clear manufactured by SICOMIN. For this purpose, the epoxy resin and hardener mixture is applied on top of a pre-cleaned specimen surface and curing is achieved at room temperatures for 3 to 4 days. Detailed procedure for coating is presented in ref. [95]. Finally after curing, a required reflective surface is obtained on top of the specimen surface. This special coating, of less than $0.1mm$ thickness, gives a very glossy, colourless and transparent surface finish on top of the specimen thus making it sufficiently reflecting (mirror-like). Fig 8.3 compares a specimen surface without any coating to that of a coated specimen plate of same material. A significant improvement in terms of reflectivity may be noted by observing a sharp image of a ceiling light onto the surface of coated plate (right) to that of a blurred image in case of untreated surface (left).

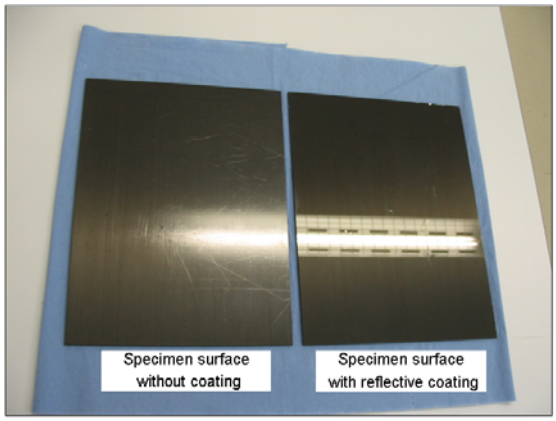

Figure 8.3: Specimen top surface without and with reflective coating.

8.3.3 Tested configurations

As discussed earlier, the objective of this present work is to provide the first experimental results for preliminary validation of the improvement in robustness and accuracy of results by comparing a less performing called bad configuration hereafter to that a proposed optimum one, as discussed in Section 5.4. For this purpose the piecewise VFM with noise minimization effect, developed in the present work, is used to identify bending rigidities of a thin composite plate. In the present preliminary experimental validation work, effect of only optimized force application point is studied. Thus, for the present case of rectangular plates instead of the square plates used earlier in Chapter 5, the same method as discussed earlier in Section 5.4 is used. For this purpose, keeping support locations similar to that of

Config-1 (refer Fig 4.1) and **F**= $5N$, sensitivity scan of the global cost function g given by Eq. 5.2, for a simulated experimental plate is performed.

Worth recalling here that a force application point corresponding to the minimum value of this global cost function represents a situation where the noise effect of all the rigidities is more balanced from one rigidity to another. For this analysis identification program capable of simultaneously identifying all the six bending rigidities and a combination of total $4x4$ piecewise virtual elements is used. For the present case of simulated experimental plate, Fig 8.4 plots the 3D image of the noise sensitivity criterion g and the contour plot.

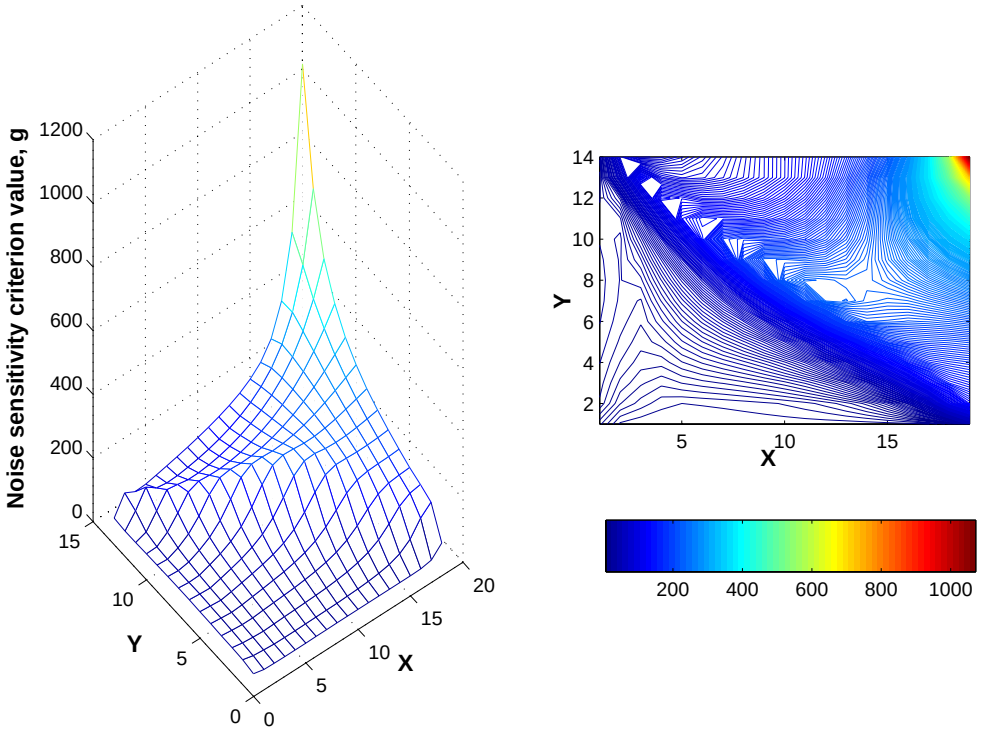

Figure 8.4: Sensitivity scan for the experimental plate using global noise minimization criterion, g.

As noted before in Section 5.4, greater noise sensitivity criterion values are observed for the load positions along the diagonal drawn between the two opposite supports, whereas comparatively lesser values with somewhat flat surface is observed near the lower left support. From this sensitivity scan, two different load positions are identified to be tested experimentally. One is in the middle of the plate on the diagonal drawn between the two opposite supports, this configuration is called as "bad configuration". The other one is found at the location where sensitivity value is minimum, this configuration is called as an "optimum configuration". These two configurations are respectively depicted in Fig 8.5.

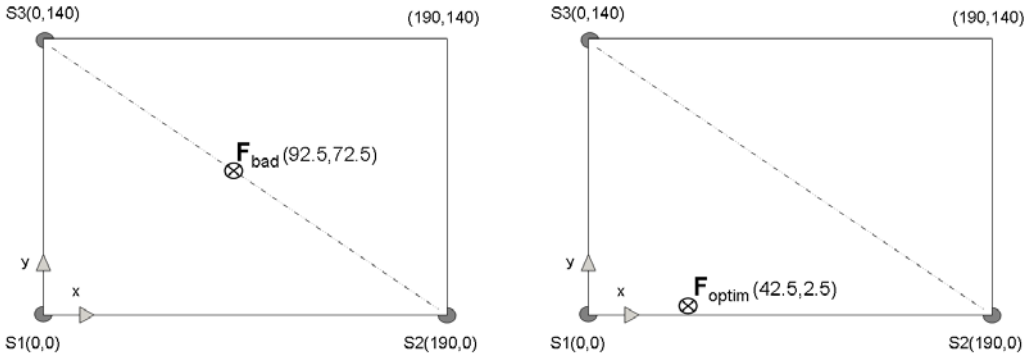

(a) Bad configuration (b) Optimum configuration

Figure 8.5: The two different configurations experimentally validated, $\mathbf{F}= 5N$.

For these two configurations simulated results of noise sensitivity index values using noisy data are evaluated. For this purpose, a Standard Gaussian white noise (equal to 5% of the amplitude of the maximum of the absolute values of the three curvatures) is added to the simulated curvature results which are then used for the identification. Total 50 such independent identifications are achieved each time using a different random copy of the added noise. Table 8.1 compares the results of bad configuration in terms of noise sensitivity index values, $\delta^{(\alpha)}$, to that of optimized configuration obtained from global criterion g. Also the respective global cost function values, g, are recorded to give an idea of the reduction in noise sensitivity criterion for the two different configurations.

	$\delta^{(\alpha)}$				g
configuration:	D_{xx}	D_{yy}	D_{ss}	D_{xy}	
Bad	10.0	2.6	2.1	58.9	178.0
Optimum	0.6	1.2	0.8	1.9	4.4

Table 8.1: Simulated results of noise sensitivity index values, $\delta^{(\alpha)}$, for bad and optimum configuration.

The betterment in identification is obvious in terms of accuracy and robustness in case of optimized configuration as the respective sensitivity index values are more balanced and reduced. Hence for optimum configuration we get a more balanced distribution of noise sensitivity index values from one rigidity to another. Now it is required to experimentally characterize these plates and study noise sensitivity for these different testing configurations using actual data. For each configuration total 21 independent tests are performed and identification is achieved. Noise sensitivity index values of the identified rigidities are calculated for the different configurations. It is expected to observe similar results as obtained from simulated study. The

experimental results are presented and discussed in the following section.

8.3.4 Experimental results and discussion

Using deflectometry method with the experimental setup described above, bending tests on the composite plates are performed. Using a constant $\mathbf{F}= 5N$, two different types of testing configurations, bad and optimum as shown in Fig 8.5, are tested separately. For each of the configurations total 21 tests are performed independently. Each test comprises of capturing undeformed and deformed grid images through the use of given CCD camera. Using Frangyne, phase maps are computed from these grid images. A phase substraction of initial and deformed phase maps directly produces wrapped phase maps related to slope fields, ϕ_x and ϕ_y. Such phase maps typically produce data in the form of fringe patterns with modulo 2π. Using Frangyne, these wrapped phase maps are then unwrapped. Frangyne uses an unwrapping algorithm where a multiple of 2π is either added or substracted locally to construct a continuous slope field. A typical example of wrapped and unwrapped phase maps of the slope fields for these configurations are shown in Fig 8.6. In these maps some missing data zones are also visible, which account for the hole through which camera sees the plate.

These slope fields may be now differentiated to obtain the required curvature fields to be used later in the identification program. But before differentiation, it is important to note here that the differentiation is very sensitive to noise and some sort of prior spatial smoothing is necessary to perform. For this purpose, the slope maps are fitted by polynomials which proves to be efficient especially in the present case where spatial frequencies of the signal (slope maps having low frequency) and the noise (high frequency) are well separated. This polynomial fitting also takes into account the missing data in the center of plate or some irregularities present at the edges. In order to find an appropriate degree polynomial for closest possible fit, fitted maps with increasing order of polynomials are compared to the actual phase maps and a RMS study to note the residuals is performed. The results of such a residual analysis are presented in Fig 8.7.

From residual value analysis as presented in Fig 8.7 it may be observed that for polynomials 9 th to 16 th degree approximately similar residuals are obtained. Another important aspect is the time required for this fitting operation, as greater is the polynomial order more closer is the fit but greater time is also required. Approximate time required for a 9, 14 and 16 th order polynomials were found to be around 1, 3 and 10 minutes on a standard Pentium4 computer with 1GB Ram. Here, 14 th order polynomial is selected as a better compromise to be used for fitting of the measured slope maps, considering that comparatively lesser residual values

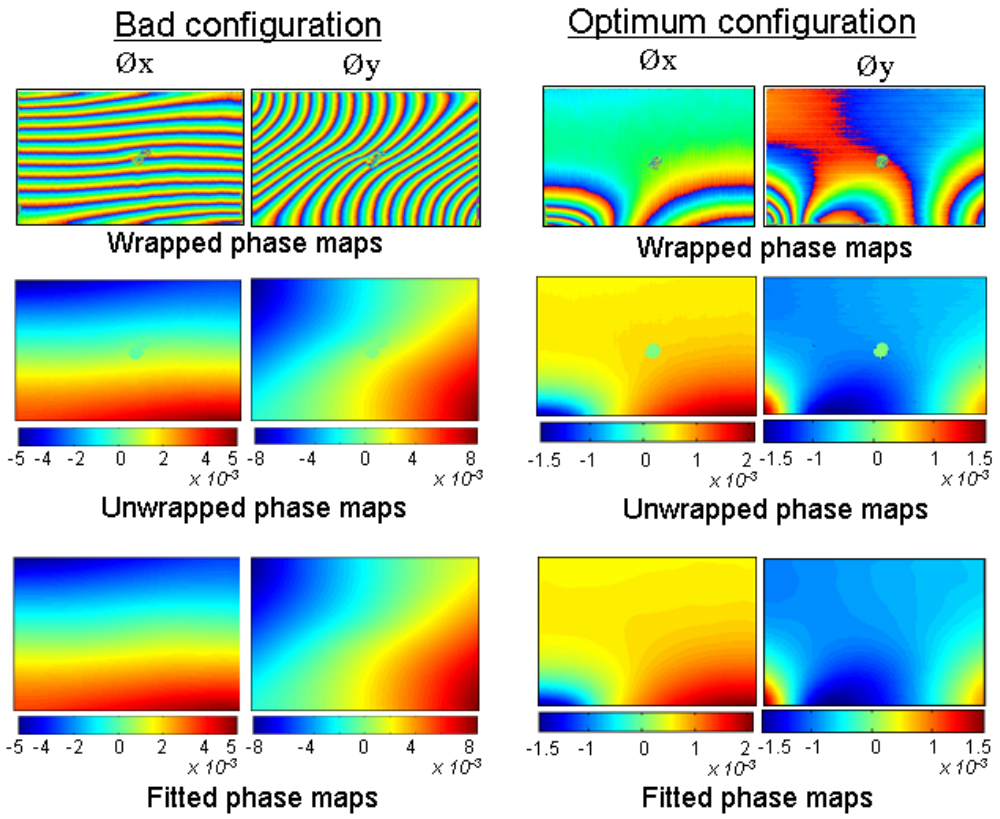

Figure 8.6: Wrapped, unwrapped (m^{-1}) and fitted phase maps (m^{-1}), using 14th order polynomial fitting, of the slope fields ϕ_x and ϕ_y.

were observed in addition to a reasonable processing time. An example of fitted phase maps is presented in Fig 8.6. Finally differentiation of such polynomial fitted slope map is performed to obtain the curvatures fields which are used as an input to the developed piecewise virtual fields method for rigidity identification. For this purpose the built-in numerical differentiation function called *gradient* of the Matlab package is used.

Now from the 21 independent set of experiments performed for the two configurations, identification results are achieved and noise sensitivity index values for the respective rigidities are evaluated. Experimental results are presented in Table 8.2 and Table 8.3. The average rigidity values recorded in Table 8.2 are very much similar to the values found at LMPF with the same plate.

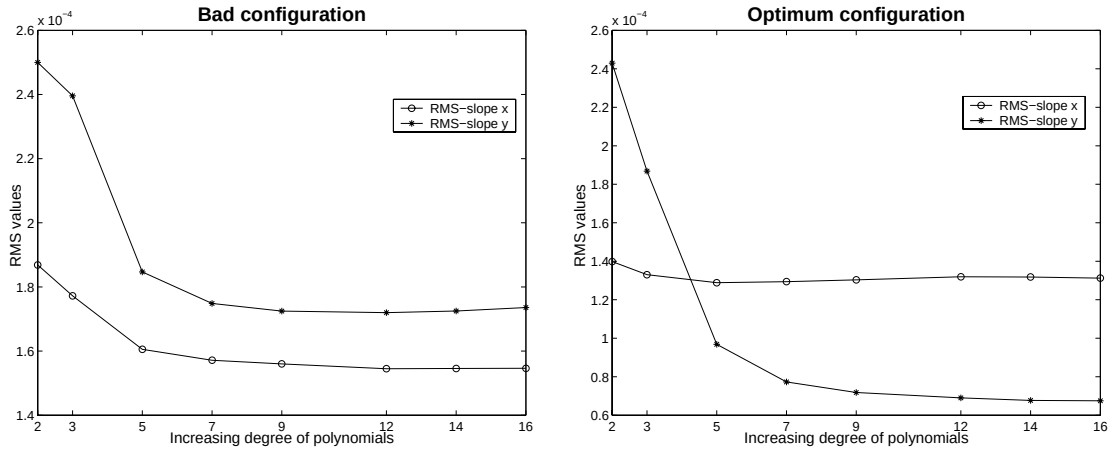

Figure 8.7: Residual analysis with increasing polynomial order.

configuration:	Average rigidity values in N.m			
	D_{xx}	D_{yy}	D_{ss}	D_{xy}
Bad	138.8	9.9	4.7	4.0
Optimum	142.5	10.7	6.2	5.3

Table 8.2: Experimental results of the average rigidity values identified in case of bad and optimum configuration using the measured experimental data.

configuration:	$\delta^{(\alpha)}$				g
	D_{xx}	D_{yy}	D_{ss}	D_{xy}	
Bad	45.4	38.1	37.0	119.5	254.6
Optimum	3.4	4.2	3.7	4.0	2.5

Table 8.3: Experimental results of noise sensitivity index values for bad and optimum configuration using the measured experimental data.

From a noise sensitivity point of view which is the main purpose of this study, the experimental results recorded in Table 8.3 are in a good qualitative agreement with simulated expectations recorded in Table 8.1. By comparison of above experimental results it may be observed that in case of bad configuration, rigidity D_{xy} is the most sensitive to noise and has a significantly greater sensitivity value in comparison to the respective values for other rigidities. But in case of optimum configuration, very balanced sensitivity values of same order are obtained for all the rigidities. As explained earlier, the cost function used for finding an optimum force location takes into account the noise effect on all the rigidities. Thus it finds an optimal load position where noise effect on all the individual rigidities is minimized and

is of the same order. Fig 8.8 presents identification results of the performed 21 separate experiments both for bad and optimum configurations. It gives an idea of the dispersion of the identified rigidity values obtained for bad and optimum configurations.

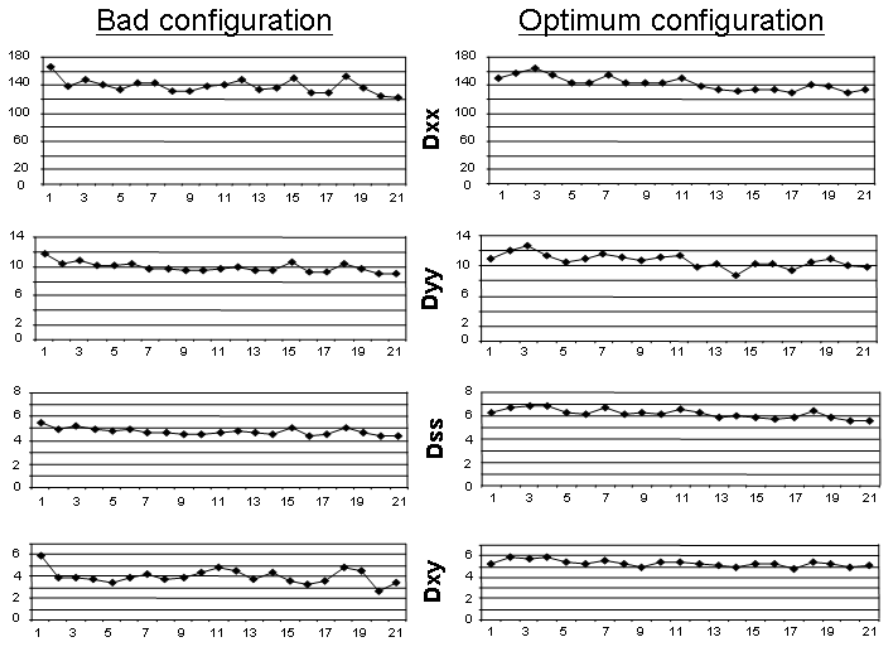

Figure 8.8: Identification results of the performed 21 separate experiments both for bad and optimum configurations.

It is worth recalling that a constant force of $5N$ is used in both the two situations for some experimental reason. Global cost function g is normalized with respect to the maximum deflection and this maximum deflection is presently much smaller in the optimum configuration than in the bad one because the same force is used in both cases (12.5 times smaller according to FE simulations). This explains the fact that a lesser scatter is not observed in case of optimum configuration. Increasing the applied force in case of optimum configuration so as to reach the same maximum deflection as in the bad configuration would lead to a reduction of this scatter, as explained in Section 5.2. This phenomenon was also verified with numerical simulations. In future works, it would be interesting to experimentally verify the betterment in scatter by using a greater applied force resulting in a greater maximum deflection. Finally, it can be said that the performed experiments using two configurations to study the effect of optimized force application point is illustrated in true spirits of the expectations as proposed by simulations.

8.4 Conclusion

In this chapter an initial experimental validation of the proposed improvement in terms of lesser noise sensitivity on the rigidities is presented by studying a bad and an optimum configuration. In the present work an optimized testing configuration is successfully validated which takes into account the reduced noise sensitivity effect on all the rigidities. The idea is to experimentally validate the simulated results, that in case of the optimum configuration in contrast to the bad configuration, noise sensitivity effect is more balanced. This work represents an initial and preliminary experimental validation. The obtained results are very promising and encouraging to perform and validate experimentally in detail the different optimization proposals, discussed earlier in Chapter 6, involving the various optimized parameters like fiber angle, specimen size, load application points and force application point.

Conclusions and perspectives

Conclusions

The present work deals with the characterization of mechanical properties of composite materials which find there ever increasing utilization in various industrial applications. The so-called virtual fields method is used for the direct determination of bending rigidities of thin anisotropic composite plates. An identification method is developed and presented in detail with description of the piecewise construction of the special virtual fields and minimization of the noise effect. A comparison with reference to an earlier study is discussed to illustrate that better and more robust identification is possible using this new proposed approach.

Three different testing configurations are numerically studied and it is shown that the approach enables to grade them with respect to better identifiability based on a noise minimization criterion. Using the same noise minimization criterion a detailed study of an optimized testing configuration is presented. Effect of different variable parameters, like fiber angle, specimen size, supports and force application points and specimen shape are studied onto the rigidity identification. Effect of these different parameters is considered separately and also in combination onto the numerically simulated examples of composite plates. Presence of more than one local minima is also observed when a combined effect of different variable parameters is studied. Finally, it is observed that an optimum combination of force and support point locations results in a significantly reduced criterion value.

Additionally, as a contribution to the ongoing separate research work at LMPF, ENSAM Châlons, dealing with the assessment of local loss in stiffness in damaged composite panels, the present work discusses an important application of the piecewise virtual fields method. It is shown that the method is effectively capable for an identification problem of a damaged composite plate. Using a simulated example of damaged composite plate, an adaptation of the method is presented which is used to simultaneously identify the bending rigidities separately for the damaged and

undamaged zones.

In the end, first experimental results of the identification of bending rigidities of a thin undamaged carbon-epoxy composite plate, for a so called bad and optimum configuration with respect to the location of force application point is presented. The results are encouraging and are in good agreement with the expected simulated results, with respect to the observed reduced noise sensitivity in case of optimum configuration.

Perspectives

In future works, it would be necessary to undertake a detailed experimental validation of the identification procedure in addition to the investigation of different optimized configurations. It is important to assess both quantitatively and qualitatively the improvement observed using the piecewise construction of the special virtual fields. Also, it is required to study the actual reduced noise sensitivity observed for different optimization proposals especially for the ones which result in significant reductions and are easily executable from an experimental point of view.

When the combined effect of different variable parameters are studied on the optimized testing configuration, the observed presence of local minima invites to study the issue in greater details using a more sophisticated optimization procedure, for instance genetic algorithms. It would be interesting to study the combined effect of all the contributing parameters such that a unique optimum combination is found which results in the best and most accurate identifiability with least sensitivity to noise. Also, it would be interesting to experimentally validate the problem of a damage plate identification especially with reference to the use of an optimum load application point for better identification of the damage zone. Another important perspective is the detailed numerical and experimental study regarding application of the piecewise virtual fields method for characterization of multi phase materials.

References

Bibliography

[1] J.D. Mathias. *Etude du comportement mécanique de patchs composites utilisés pour le renforcement de structures métalliques aéronautiques.* PhD thesis, Laboratoire de Mécanique et Ingénieries (LaMI), Université Blaise Pascal (UBP) Clermont II et Institut Française de Mécanique Avancée (IFMA), 2005.

[2] Y. Surrel. Deflectometry : a simple and efficient noninterferometric method for slope measurement. Proceedings of SEM International Congress, Costa-Mesa (USA), June 2004.

[3] M. Grédiac, E. Toussaint, and F. Pierron. Special virtual fields for the direct determination of material parameters with the virtual fields method. 3-Application to the bending rigidities of anisotropic plates. *International Journal of Solids and Structures*, 40(10):2401–2419, 2003.

[4] M.A. Sutton, W.J. Wolters, W.H. Perters, W.F. Ranson, and S.R. McNeill. Determination of displacements using an improved digital correlation method. *Image and Vision Computing*, 1(3):133–9, 1983.

[5] T.C. Chu, W.F. Ranson, M.A. Sutton, and W.H. Petters. Application of digital image correlation techniques to experimental mechanics. *Experimental Mechanics*, 3:232–244, 1985.

[6] R. Jones and C. Wykes. *Holographic and speckle interferometry.* Cambridge, MA: Cambridge University Press, 2000.

[7] D.W Robinson and G.T. Reid. *Interferogram analysis: digital fringe pattern measurement techniques.* Philadelphia, PA: IOP Publications Ltd, 2001.

[8] Y. Surrel. Moiré and grid methods in optics : a signal-processing approach. Proceedings of SPIE, 1994.

[9] V.J. Parks. Strain measurement using grids. *Optical Engineering*, 21(4):633–639, 1982.

[10] P.M. Boone, A.G. Vinckier, R.M. Denys, W.M. Sys, and E.N. Deleu. Application of specimen-grid moiret techniques in large scale steel testing. *Optical Engineering*, 21(44):615–625, 1982.

[11] Y. Surrel, N. Fournier, M. Grédiac, and P.A. Paris. Phase-stepped deflectometry applied to shape measurement of bent plates. *Experimental Mechanics*, 39(1):66–77, 1998.

[12] S. Avril, M. Grédiac, F. Pierron, Y. Surrel, and E. Toussaint. Deflectometry and virtual fields for identification of static plate bending stiffnesses. Proceedings of SEM International Congress, Costa-Mesa (USA), June 2004.

[13] S. Pagano. A review of identification methods based on full field measurements. Photomechanics 2006, Clermont-Ferrand, France.

[14] M.A.N. Hendriks. *Identification of the mechanical properties of solid materials.* PhD thesis, Eindhoven University of Technology, 1991.

[15] M. Meuwissen. *An inverse method for the mechanical characterization of metals.* PhD thesis, Eindhoven University of Technology, 1998.

[16] G. Mauvoisin. *Développement et mise en oevre d'une technique de moiré d'ombre quasi-hérodyne de mesure de relief en vue de la détermination de lois de comportemnt élastique de matériaux orthotropes.* PhD thesis, Université de Poitiers, 1993.

[17] M.H. Arafeh. *Identification de la loi de comportement élastique de matériaux orthotropes.* PhD thesis, Université de Technologie de Compiègne, 1995.

[18] M.H. Arafeh, C. Knopf-Lenoir, and F. Rouger. Conception optimale d'essais de flexion de plaques orthotropes et identification. *Comptes Rendus de l'Académie des Sciences*, II/321:351–354, 1995.

[19] L. Le Magorou. *Identification de la loi de comportement élastique et viscolastique de panneaux structuraux à base de bois.* PhD thesis, Université de Bordeaux I, 2002.

[20] L. Le Magorou, F. Bos, and F. Rouger. Identification of constitutive laws for wood-based panels by means of an inverse method. *Composite Science and Technology*, 62(4):591–596, 2002.

[21] M.H.H. Meuwissen, C. W.J. Oomens, F.P.T. Baaijens, R. Petterson, and J.D. Janssen. Determination of the elasto-plastic properties of aluminium using a

mixed numerical-experimental method. *Journal of Materials Processing Technology*, 75(1-3):204–211, 1998.

[22] G. Silva, R. Le Riche, J. Molimard, and A. Vautrin. Integrated strategy for identification of plate stiffness components. Photomechanics 2006, Clermont-Ferrand, France.

[23] D. Lecompte, H. Sol, J. Vantomme, and A.M. Habraken. Comparision between homogeneous and heterogeneous field information for plastic material identification. Photomechanics 2006, Clermont-Ferrand, France.

[24] R. Meijer, L.F.A. Douven, and C.W.J. Oomens. Characterization of anisotropic and non-linear behaviour of human skin in-vivo. *Comput. Methods in Biomechanics and Biomedical Engineering*, 1:13–27, 1997.

[25] M.R. Van Ratingen. *Mechanical identification of inhomogeneous solids: a mixed numerical experimental approach.* PhD thesis, Eindhoven University of Technology, 1994.

[26] C.W.J. Oomens, M.R. Van Ratingen, J.D. Janssen, J.J. Kok, and M.A.N. Hendriks. A numerical-experimental method for a mechanical characterization of biological materials. *Journal of Biomechanics*, 26(4/5):617–621, 1993.

[27] M. Bonnet and A. Constantinescu. Inverse problems in elasticity. *Inverse problems*, 21(2):R1–R50, 2005.

[28] P. Ladevèze and D. Leguillon. Error estimates procedure in the finite element method and applications. *SIAM J. Numer. Anal.*, 20:485–509, 1983.

[29] M. Bonnet, H.D. Bui, and A. Constantinescu. Principes variationnels et exploitation de mesures de champs en élasticité: Variational principles and exploitation of field measurements in elasticity. *Mécanique and Industries*, 4(6):687–697, 2003.

[30] A. Constantinescu. On the identification of elastic moduli from displacement-force boundary measurements. *Inverse Problems in Engineering*, 1:293–315, 1994.

[31] A. Constantinescu. On the identification of elastic moduli in plates. *Inverse Problems in Engineering Mechanics*, 1:205–214, 1998.

[32] A. Deraemaeker, P. Ladevèze, and Ph. Leconte. Reduced basis for modal updating in structural dynamics based on constitutive relation error. *Comput. Methods. Appl. Mech. Eng*, 191:2427–2444, 2002.

[33] P. Ladevèze, M. Reynier, and D. Nedjar. Parametric correction of finite element models using modal tests. *Inverse Problems in Engineering Mechanics*, pages 91–100, 1993.

[34] M. Reynier. *Sur le controle de modélisation éléments finis: recalage à partir d'essais dynamiques.* PhD thesis, Université Pierre et Marie Cuire, Paris, France., 1990.

[35] F. Latourte, A. Chrysochoos, S. Pagano, and B. Wattrisse. Identification of elastoplastic parameters distributions using digital image correlations. Photomechanics 2006, Clermont-Ferrand, France.

[36] G. Geymonat, F. Hild, and S. Pagano. Identification of elastic parameters by displacement field measurement. *Comptes Rendus Mecanique*, 330:403–408, 2002.

[37] D. Claire, F. Hild, and S. Roux. Identification of damaged fields using kinematic measurements. *Comptes Rendus Mecanique*, 330(11):729–734, 2002.

[38] D. Claire, F.Hild, and S. Roux. A finite formulation to identify damage fields: The equilibrium gap method. *International Journal of Numerical Methods in Engineering*, 61(2):189–208, 2004.

[39] J. Lemaitre and J.L. Chaboche. *Mechanics of solid materials.* Cambridge University Press, 1990.

[40] F. Amiot, F.Hild, and J.P. Roger. Mesure de champs de déplacements pour des MEMS. CFM 2005 - XVIIe Congrès français de mécanique, France.

[41] F. Amiot, F.Hild, and J.P. Roger. Identification of elastic property and loading fields from full-field displacement measurements. *International Journal of Solids and Structures*, 2006. In Press, available online.

[42] F. Amiot, F.Hild, and J.P. Roger. Model and parameter identification using non-contact loading and full-field measurement. Proceedings SEM XI, 2005, 6 p.

[43] N.Garraud, F. Amiot, F.Hild, and J.P. Roger. Full-field measurement of micro-cantiliver displacement induced by molecule adsorption- Identification of mechanical parameters. Photomechanics 2006, Clermont-Ferrand, France.

[44] H.D. Bui. Sur quelques problèmes inverses élastiques en mécanique de l'endommagement. In Deuxiéme Colloque National de Calcul des Structures. Hermès., 1995.

[45] M. Ikehata. Inversion formulas for the linearized problem for an inverse boundary value problem in elastic prospection. *SIAM Journal on Applied Mathematics*, 50:1635–1644, 1990.

[46] A.P. Calderon. On an inverse boundary value problem. In Seminar on Numerical Analysis and its applications to Continuum Physics. Soc. Brasilian de Matematica, Rio de Janeiro., 1980.

[47] M. Ikehata. An inversion problem for the plate in the Love-Kirchhoff theory. *SIAM Journal on Applied Mathematics*, 53:942–970, 1993.

[48] A. Ben Abda, H. Ben Ameur, and M. Jaoua. Identification of 2D cracks by boundary elastic measurements. *Inverse Problems*, 15:67–77, 1999.

[49] S. Andrieux, A. Ben Abda, and H.D. Bui. Sur l'identification de fissures planes via le concept d'écart à la réciprocité en élasticité. *Comptes Rendus de l'Académie des Sciences Paris, Sér. II.*, 324:1431–1438, 1997.

[50] S. Andrieux, A. Ben Abda, and H.D. Bui. Reciprocity principle and crack identification. *Inverse Problems*, 15:59–65, 1999.

[51] H.D. Bui, A. Constantinescu, and H. Maigre. Numerical identification of linear cracks in 2D elastodynamics using the instantaneous reciprocity gap method. *Inverse Problems*, 20:993–1001, 2004.

[52] M. Grédiac. Principe des travaux virtuels et identification. *Comptes Rendus de l'Académie des Sciences*, 309:1–5, 1989. Elsevier, in French with abridged English Version.

[53] M. Grédiac and A. Vautrin. A new method for determination of bending rigidities of thin anisotrpic plates. *Journal of Applied Mechanics*, 57:964–968, 1990.

[54] M. Grédiac. The use of heterogeneous strain fields for the characterization of composite materials. *Composite Science and Technology*, 56:841–846, 1996.

[55] M. Grédiac. On the direct determination of invariant parameters governing the bending of anisotropic plates. *International Journal of Solids and Structures*, 33:3969–3982, 1996.

[56] M. Grédiac and P.A. Paris. Direct identification of elastic constants of anisotropic plates by modal analysis: theoretical and numerical aspects. *Journal of Sound and Vibration*, 195(3):401–415, 1996.

[57] M. Grédiac, N. Fournier, P.A. Paris, and Y. Surrel. Direct identification of elastic constants of anisotropic plates by modal analysis: experiments and results. *Journal of Sound and Vibration*, 210(5):645–659, 1998.

[58] A. Giraudeau and F. Pierron. Simultaneous identification of stiffness and damping properties of isotropic materials from forced vibrating plates. *Comptes Rendus de l'Académie des Sciences*, 331:259–264, 2003.

[59] M. Grédiac and F. Pierron. A T-shaped specimen for the direct characterization of orthotropic materials. *International Journal for Numeriacl Methods in Engineering*, 41:293–309, 1998.

[60] M. Grédiac, F. Pierron, and Y. Surrel. Novel procedure for complete in-plane composite characterization using a T-shaped specimen. *Experimental Mechanics*, 39(2):142–149, 1999.

[61] M. Grédiac, F. Pierron, and A. Vautrin. The Iosipescu in-plane shear test: a new approach based on displacement field processing. *Composite Science and Technology*, 51:409–417, 1995.

[62] F. Pierron and M. Grédiac. Identification of the through-thickness moduli of thick composites from whole-field measurements using the iosipescu fixture: theory and simulations. *Composites Part A*, 31(4):309–318, 2000.

[63] F. Pierron, S. Zhavaronok, and M. Grédiac. Identification of the through-thickness properties of thick laminates using the virtual fields method. *International Journal of Solids and Structures*, 37(32):4437–4453, 2000.

[64] M. Grédiac, F. Auslender, and F. Pierron. Applying the virtual fields method to determine the through-thicknss moduli of thick composites with a nonlinear shear response. *Composites Part A*, 32(12):1713–1725, 2001.

[65] M. Grédiac, E. Toussaint, and F. Pierron. Principe de la méthode des champs virtuels avec champs spéciaux: Principle of the virtual fields method with special virtual fields. *Mécanique & Industries*, 4:679–686, 2003.

[66] M. Grédiac, E. Toussaint, and F. Pierron. Special virtual fields for the direct determination of material parameters with the virtual fields method. 1- Principle and definition. *International Journal of Solids and Structures*, 39:2691–2705, 2002.

[67] M. Grédiac, E. Toussaint, and F. Pierron. Special virtual fields for the direct determination of material parameters with the virtual fields method. 2- Application to in-plane properties. *International Journal of Solids and Structures*, 39:2707–2730, 2002.

[68] S. Avril, M. Grédiac, and F. Pierron. Sensitivity of the virtual fields method to noisy data. *Computational Mechanics*, 34:439–452, 2004.

[69] E. Toussaint, M. Grédiac, and F. Pierron. The virtual fields method with piecewise virtual fields. *International Journal of Mechanical Sciences*, 48:256–264, 2006.

[70] H. Chalal, F. Meraghni, F. Pierron, and M. Grédiac. Direct identification of the damage behaviour of composite materials using the virtual fields method. *Composites Part A*, 35(7-8):841–848, 2004.

[71] M. Grédiac and F. Pierron. Applying the Virtual Fields Method to the identification of elasto-plastic constitutive parameters. *International Journal of Plasticity*, 22(4):602–627, 2006.

[72] M. Grédiac. The use of full-field measurement methods in composite material characterization: interest and limitations. *Composites Part A*, 35:751–761, 2004.

[73] M. Grédiac, E. Toussaint, and F. Pierron. L'identification des propriétés mécaniques de matériaux avec la méthode des champs virtuels, une alternative au recalage par éléments finis: Identification of the mechanical properties of materials with the virtual fields method, an alternative to finite element model updating. *Comptes Rendus Mécanique*, 330:107–112, 2002.

[74] S.G. Lekhnitskii. *Anisotropic plates.* Gordon and Breach, 1968.

[75] O.C. Zienkiewicz. *The finite element method.* New York: McGraw-Hil, 1977.

[76] G. Dhatt and G. Touzot. *Une présentation de la méthode des éléments finis.* Maloine S.A., 1984.

[77] M. Grédiac and F. Pierron. Numerical issues in the virtual fields method. *International Journal for Numeriacl Methods in Engineering*, 59:1287–1312, 2004.

[78] S. Timoshenko and S. Woinowsky-Krieger. *Theory of plates and shells.* McGraw-Hill, New York, 1958.

[79] K. Syed-Muhammad, E. Toussaint, M. Grédiac, S. Avril, and F. Pierron. Extraction de paramètres d'une loi de comportement anisotrope avec la méthode des champs virtuels : construction de champs virtuels par sous-domaines et minimisation de l'effet du bruit de mesure. In *7ème Colloque National en Calcul des Structures*, Giens, mai 2005.

[80] K. Syed-Muhammad, E. Toussaint, M. Grédiac, and S. Avril. Characterization of composite paltes using the Virtual Fields Method : piecewise virtual fields, minimization of noise effect and optimization of testing configuration. In *8th European Mechanics of Materials Conference*, Cachan, september 2005.

[81] K. Syed-Muhammad, E. Toussaint, M. Grédiac, and S. Avril. Optimisation d'un essai sur plaque avec la méthode des champs virtuels. In *17 ème Congrès Français de Mécanique*, Troyes, septembre 2005.

[82] F. Pierron, G. Vert, R. Burguete, S. Avril, R. Rotinat, and M. Wisnom. Optimization of the unnotched Iosipescu test on composites for identification from full-field measurement. 6ème congrès international: Modern practice in stress and vibration anlysis, Institute of Physics and British Society for Strain Measurements., September 2006, Bath (GB).

[83] J.D. Mathias, X. Balandraud, and M. Grédiac. Applying a genetic algorithm to the optimization of composite patches. *Computers & Structures*, 84:823–834, May 2006.

[84] J. H. Kim, F. Pierron, K. Syed Muhammad, M. R. Wisnom, M. Grédiac, and E. Toussaint. Assessment of the local stiffness reduction on a composite impacted plate with the virtual fields method. Photomechanics 2006, Clermont-Ferrand, France., 58-59.

[85] J. H. Kim, F. Pierron, M. R. Wisnom, and K. Syed Muhammad. Identification of the local loss in stiffness reduction of a damaged composite plate using the virtual fields method. *Special Issue of Composites Part A*, 2006. Submitted.

[86] R. Steinberger, T.I. Valadas Leitão, E. Ladstätter, G. Pinter, W. Billinger, and R.W. Lang. Infrared thermographic techniques for non-destructive damage characterization of carbon fibre reinforced polymers during tensile fatigue testing. *International Journal of Fatigue*, 28(10):1340–1347, 2006.

[87] T.E. Preuss and G. Clark. Use of time-of-flight C-scanning for assessment of impact damage in composites. *Composites*, 19(2):145–148, 1988.

[88] R. Rùzek, R. Lohonka, and J. Jironè. Ultrasonic C-scan and shearography ndi techniques evaluation of impact defects identification. *NDT&E International*, 39(2):132–142, 2006.

[89] Z. Su, L. Ye, and Y. Lu. Guided lamb waves for identification of damage in composite structures: a review. *Journal of Sound and Vibration*, 2006. In press.

[90] S. Huguet, N. Godin, R. Gaertner, L. Salmon, and D. Villard. Use of acoustic emission to identify damage modes in glass fibre reinforced polyester. *Composites Science and Technology*, 62(10-11):1433–1444, 2002.

[91] H. Hu, B.T. Wang, C.H. Lee, and J.S. Su. Damage detection of surface cracks in composite laminates using modal analysis and strain energy method. *Composite Structures*, 74:399–405, 2002.

[92] Y. Surrel. Design of algorithms for phase measurements by the use of phase stepping. *Applied Optics*, 35(1):51–60, 1996.

[93] Y. Surrel. *Fringe analysis. in "Photomechanics"*. Springer, 1999. P.K.Rastogi Ed.

[94] P.P. Camanho and F.L. Matthews. A progressive damage model for mechanically fastened joints in composite laminates. *Journal of Composite Materials*, 33(24):2248–2280, 1999.

[95] J. H. Kim, F. Pierron, M. Grédiac, and M. R. Wisnom. A procedure for producing reflective coatings on plates to be used for full-field slope measurements by a deflectometry technique. *Strain*, 2006. In revision.